Studies of trapped, cooled ion ensembles

Inaugural-Dissertation

zur Erlangung des Doktorgrades
der Mathematisch-Naturwissenschaftlichen Fakultät
der Heinrich-Heine-Universität Düsseldorf

vorgelegt von

David Offenberg
aus Leverkusen

Düsseldorf, Oktober 2009

Aus dem Institut für Experimentalphysik
der Heinrich-Heine-Universität Düsseldorf

Gedruckt mit der Genehmigung
der Mathematisch-Naturwissenschaftlichen Fakultät
der Heinrich-Heine-Universität Düsseldorf

Referent: Prof. S. Schiller, Ph.D.

Koreferent: Prof. Dr. R. Weinkauf

Tag der mündlichen Prüfung: 16.12.2009

Abstract

This work presents various novel results in the field of experimental and theoretical trapped ion studies. All investigations involve laser-cooled $^{138}Ba^{+}$ ions confined in a linear quadrupole ion trap, which serve as coolant for complex molecular ions, as target for collisions with neutral atoms, or as model system in theoretical analyses.

The special feature of the apparatus used in this work is a molecular ion source based on electrospray ionization that allows for the production of gas-phase molecular ions of almost any species with a maximum mass-to-charge ratio of 2,000 Da. Trapped together with laser-cooled $^{138}Ba^{+}$ ions, the molecular ions can be cooled down, kept cold and investigated for many minutes, and in principle for hours, in a nearly collisionless environment. In this work, the sympathetic cooling of complex molecular ions to translational temperatures below 1 K is demonstrated for different types of molecules covering a mass range from 182 to 12,400 Da. For example, the protein cytochrome c, with a mass of about 12,400 Da, is the most massive molecular species sympathetically cooled in an ion trap so far. The methods for detecting successful trapping and cooling, and for the determination of the temperature are presented in detail. In one case, multiply protonated molecules of the protein cytochrome c have been cooled to less than 0.75 K.

Furthermore, two methods for measuring photodestruction rates of cold, trapped complex molecular ions have been developed that can, for example, be applied in destructive spectroscopy schemes. Both techniques are demonstrated using singly protonated glycyrrhetinic acid molecules (GAH^{+}) dissociated by an ultraviolet (UV) laser. Measurements of the photodestruction rate were performed at different intensities of the UV laser, and rates as low as 0.05 s^{-1} and less have been determined, which is only possible due to the long ion storage times that can be achieved with this apparatus. For the UV laser wavelength of 266 nm, a destruction cross section of $(1.1 \pm 0.1) \cdot 10^{-17}\,cm^2$ for GAH^{+} has been determined.

In this work, feasibility studies towards internal cooling of trapped complex molecular ions have been performed. Such an additional internal cooling could be realized via collisions with laser-cooled neutral atoms. To test their suitability, neutral atoms of Li, Na, K, Rb, Cs, and Yb have been collided with trapped laser-cooled and non-cooled Ba^{+} ions as well as with complex molecular ions. For all species charge exchange reactions with Ba^{+} ions have been observed, which excludes these species for use in collisional cooling. While K, Rb, and Cs showed charge exchange reactions with ground state and laser-excited Ba^{+} ions, the charge exchange rates of Yb and Ba^{+} were found to be state dependent. Collisions of neutral Yb atoms were found to be reactive and lead to the formation of adducts and fragments, in contrast to the alkali metals for which no such reactions have been observed.

In addition, the motion of cooled, trapped ions has been studied theoretically via simulations. When the translational energy of a trapped ion ensemble is sufficiently reduced, a first-order phase transition from a liquid to a solid state occurs with the ion ensemble changing from a disordered ion cloud to an ordered ion crystal. As ions in a linear quadrupole trap arrange in shell structures, a free motion in the radial direction is disabled, and ions can only move to neighboring shells when their kinetic energy is high enough to overcome a certain potential barrier. The simulations have shown that intershell diffusion rates in the considered ion crystals increase exponentially when the ion temperatures exceed values that well agree with the predictions of other established models. Ion ensembles of different ion numbers (300, 500, and 1000 $^{138}Ba^{+}$ ions) and symmetries (prolate and spherical) have been investigated showing a clear tendency for the phase transition temperatures: the higher the ion number, the lower the transition temperature.

Contents

1 Introduction

1.1 Motivation

In recent years, enormous progress has been made in the production of cold neutral and charged molecules. By common convention, molecules are designated as *cold* when exhibiting translational temperatures between 1 and 1000 mK [1]. In this low-temperature regime effects of light-molecule, atom-molecule, and molecule-molecule interactions become accessible that do not occur or cannot be observed at higher temperatures.

One wide field of current cold molecule research is the investigation of cold collisions [2, 3, 4]. Low collision energies allow one to study quantum mechanical details of collisional processes, with the deBroglie wavelength of the involved particles becoming comparable to the scale of their interaction. For example, elastic and inelastic collisions at very low temperatures can be strongly dominated by resonances [5], and also chemical reactions are expected to feature resonances in the cross section as a function of their collision energies [6].

Another important field where cold molecules are finding application is in high-resolution spectroscopy, where molecular transition frequencies can be measured with greater accuracy. Molecular spectra can be simplified greatly by cooling. Translational cooling increases the spectral resolution due to a reduction of Doppler and collisional line broadening, and internal cooling leads to molecules in vibrational ground states resulting in less congested spectra. High-resolution spectroscopy of cold molecules is also of special interest for fundamental tests of physics, such as the precise determination of fundamental constants [7, 8]. Furthermore, the accurate knowledge of transition frequencies allows one to test and to challenge quantum chemical calculations of rovibrational energy levels, or to gain structural and conformational information on the investigated molecular species [9].

Cold neutral and charged molecules have been produced using a variety of different techniques. To mention just a few examples, cold few-atom neutral molecules can be produced by photoassociation or through Feshbach resonances in ultracold atomic gases [10, 11, 12], by buffer gas cooling in magnetic traps [13], by electrostatic deceleration [14] or by using superfluid helium droplets [15]. However, the largest variety of cold molecular species has been obtained in the charged state via sympathetic cooling with laser-cooled atomic ions in ion traps [16, 17, 18, 19, 20, 21].

For this work, a unique apparatus based on sympathetic cooling has been used to significantly extend the mass range of producible cold molecules. Almost any kind of molecule can be protonated using an electrospray ionization (ESI) molecular ion source: including, even, molecules with masses more than 10,000 Da. Stored together with laser-cooled atomic $^{138}Ba^{+}$ ions in a linear quadrupole ion trap, these molecular ions translationally cool down via their mutual Coulomb interaction with the laser-cooled species. In this way, such complex molecules as proteins can be cooled to translational temperatures below 1 K [21]. An outstanding advantage of this method are the long storage times of tens of minutes, and, in principle, several hours, that cannot be reached with neutral molecule techniques. This, combined with the well-defined and nearly collisionless environment of

an ion trap, provides ideal conditions for various kinds of experiments, such as the observation of slow and low-energy processes or high-resolution spectroscopy using low-intensity narrow-linewidth lasers.

1.2 Outline

This work is organized as follows: in Chapter 2 the fundamentals of ion trapping in linear quadrupole traps and the cooling techniques used in this work are described. Among them is Doppler laser cooling which, applied to suitable trapped atomic ions, leads to the formation of ordered structures, so-called Coulomb or ion crystals, that are described in the end of the chapter.

The experimental setup is presented in Chapter 3 starting with an overview of the whole vacuum apparatus, followed by a detailed description of the electrospray ionization (ESI) molecular ion source and its basic principle. In addition, the trap setup is described, including the components used for the detection and analysis of the trapped ions. The laser system has been presented in detail in previous dissertations on this project [22, 23], so that it is only mentioned briefly here.

In Chapter 4 the three methods used for analysis of the trapped ion ensembles are introduced. The non-destructive secular excitation method and the destructive ion extraction method both can be applied for instantaneous identification of trapped ion species. Molecular dynamics (MD) simulations of the observed ion crystals in a post-experimental step enable quantitative values for ion numbers and temperatures to be obtained. The MD simulations are further used for theoretical studies and analysis of the ion's interaction and motion.

Chapters 5 to 7 report on the experimental results achieved during this work. In Chapter 5 the procedure for the preparation of cold complex molecular ion ensembles is described. Using the example of the protein cytochrome c, the most massive molecular species sympathetically cooled in an ion trap so far, the methods for detection of successful trapping and cooling, and for temperature determination are presented.

Photodissociation spectroscopy is a common tool to gain information on molecular structures, to distinguish between different isomers or to study the energetics and pathways of fragmentation. Often, these studies rely on measurements of dissociation or destruction rates. In this work two techniques for the measurement of photodestruction rates of translationally cold, trapped molecular ions have been developed and tested. These techniques are presented in Chapter 6 together with the experimental results achieved with the test molecule glycyrrhetinic acid.

As a pre-study for future cold collision experiments, the interaction of neutral metal atoms (evaporated from ovens) with cooled and non-cooled trapped atomic and molecular ions have been investigated. Charge exchange reactions of warm Li, Na, K, Rb, Cs, and Yb atoms with trapped Ba^+ ions have been observed and are presented in Chapter 7. Collisions of Yb atoms with trapped molecular ions lead to the formation of adducts and fragments as shown at the end of this chapter.

Chapter 8 reports on the results of a theoretical study on Coulomb crystallization. In common ion traps, there is a first-order phase transition from a liquid to a solid state. A so-called Coulomb crystal is formed at translational ion temperatures of a few millikelvin, and at this point the ion motion changes significantly. The behaviour of the ion ensembles around these critical points has been analyzed for crystals of different sizes: sizes which are typically produced in the experiment.

2 Trapping and cooling of ions

An ion trap placed in an ultra-high vacuum chamber allows one to store and to cool charged particles in a well-defined and nearly collisionless confined volume. The linear quadrupole trap type (Chapter 2.1) provides good optical access to the trapped ion ensembles and is, for this reason, most suitable for the experiments within this project. Furthermore potential wells with depths of several electron volts can be achieved, so that trapping of ions with kinetic energies in the electron volt regime and cooling can be realized in the same trap.

Doppler laser cooling (Chapters 2.2.2 and 2.2.3) is an efficient method to reduce the translational energy of trapped ions. It is restricted to a few ion species with suitable electron configurations that provide closed optical transitions. However, indirectly, laser cooling can be applied to other, non-laser-coolable ions when they are simultaneously trapped with laser-cooled ions. This so-called sympathetic cooling (Chapter 2.2.1) is based on the ions' mutual elastic Coulomb interaction which leads to a redistribution of the ions' kinetic energies.

Provided that the cooling power is sufficient, such trapped ion ensembles can undergo a liquid-solid phase transition from disordered ion clouds to ordered ion crystals. In the crystal state, ions arrange in shell structures and separate depending on their mass-to-charge ratios as described in Chapter 2.3.

2.1 Linear quadrupole trap

The basic principle of ion traps is the creation of an electric potential minimum in the trapping region where equally charged particles can accumulate. According to Earnshaw's theorem [24], it is not possible to create a three-dimensional extremum of a potential $\Phi(x, y, z)$ using electrostatic forces alone, as the Laplace equation

$$\triangle\Phi = \frac{\partial^2\Phi}{\partial x^2} + \frac{\partial^2\Phi}{\partial y^2} + \frac{\partial^2\Phi}{\partial z^2} = 0 \tag{2.1}$$

cannot be fulfilled. Assuming, for example, an harmonic potential $\Phi = \alpha x^2 + \beta y^2 + \gamma z^2$, the Laplace equation yields $\alpha + \beta + \gamma = 0$, so that the factors α, β, γ cannot all have the same sign simultaneously. This illustrates, that any static electric field would always be repulsive in at least one direction.

However, there are several possibilities to trap charged particles. In Penning traps, for example, trapping is achieved by a superposition of static electric and magnetic fields [25]. Though, being rather strong, these magnetic fields can be a source of limitation in precision measurements. This problem can be avoided using radio frequency traps, such as the linear quadrupole trap. Here, a combination of static electric fields and alternating electric fields with frequencies in the radio frequency range leads to an effective potential minimum in the trap center (Chapter 2.1.2).

As shown in Fig. 2.1, the configuration of a linear quadrupole trap is basically that of a quadrupole mass filter, which confines ions radially in the xy-plane and goes back to

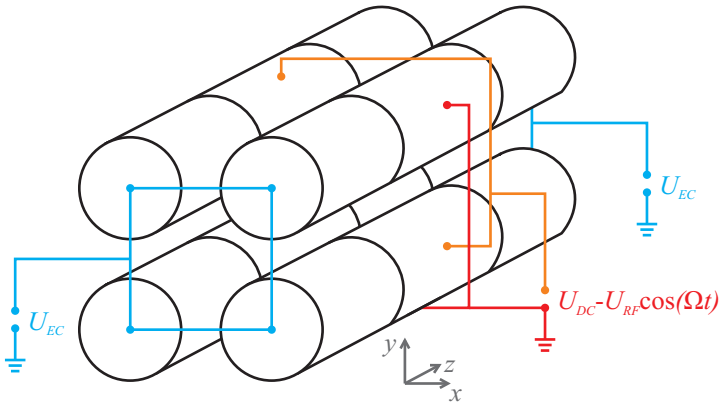

Figure 2.1: The linear quadrupole trap. Schematic view and electronic wiring.

Wolfgang Paul in 1958 [26]. Electrodes added to both ends of each quadrupole electrode provide an additional axial ion confinement along the z-axis resulting in total in a three-dimensional confinement.

2.1.1 Radial confinement - The quadrupole mass filter

A quadrupole mass filter in its ideal form consists of four hyperbolically shaped electrodes in quadrupole configuration (Fig. 2.2(a)). In practice, usually cylindrical electrodes are used as the resulting deviations from the real quadrupole potential are almost negligible near the trap center. Opposing electrodes are electronically connected, between neighboring electrodes the voltage $\Phi_0 = U_{DC} - U_{RF}\cos(\Omega t)$ is applied leading to the quadrupole saddle potential (Fig. 2.2(b))

$$\Phi(x, y, t) = \frac{U_{DC} - U_{RF}\cos(\Omega t)}{2r_0^2}(x^2 - y^2), \tag{2.2}$$

where r_0 is the distance from the surface of the electrodes to the trap center, U_{DC} is a direct (static) voltage and U_{RF} is the amplitude of an alternating voltage with the angular frequency Ω.

For the two-dimensional motion of an ion with the charge Q and the mass m the equations of motion

$$\ddot{x} + \frac{Q}{mr_0^2}(U_{DC} - U_{RF}\cos(\Omega t))x = 0 \tag{2.3}$$

$$\ddot{y} + \frac{Q}{mr_0^2}(U_{DC} - U_{RF}\cos(\Omega t))y = 0 \tag{2.4}$$

can be transformed using the dimensionless parameters

$$\tau = \frac{\Omega t}{2}, \quad a = a_x = -a_y = \frac{4QU_{DC}}{mr_0^2\Omega^2}, \quad q = q_x = -q_y = \frac{2QU_{RF}}{mr_0^2\Omega^2} \tag{2.5}$$

to the well-known Matthieu differential equations

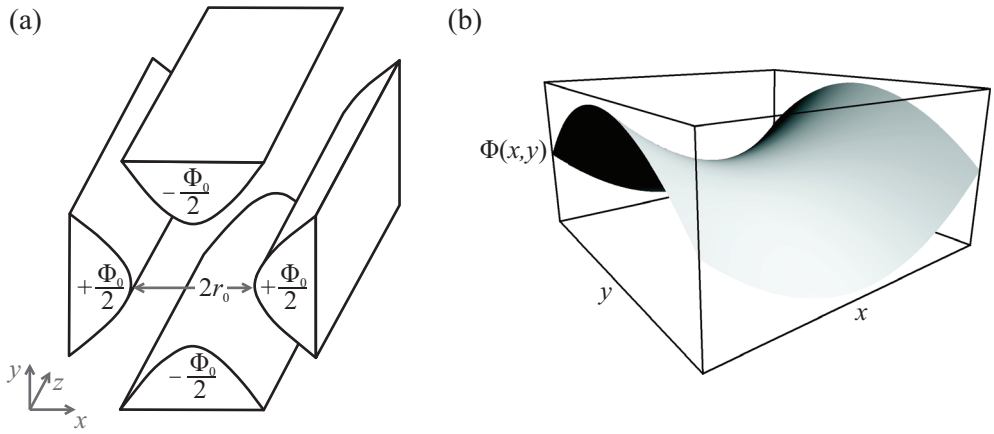

Figure 2.2: The quadrupole mass filter. (a) Schematic view. (b) Illustration of the two-dimensional saddle potential of the quadrupole mass filter as given in Eq. (2.2).

$$\frac{\partial^2 u}{\partial \tau^2} + (a_u - 2q_u \cos(2\tau))u = 0 \quad \text{with} \quad u = x, y. \tag{2.6}$$

Fig. 2.3(a) shows regions in the aq-space where these equations have stable periodic solutions in x- or y-direction. Radial confinement of the ion, i. e. stable radial motion in the xy-plane, is given for parameter pairs (a, q) lying in overlap regions of x- and y-stability [27]. The first radial stability region (Fig. 2.3(b)) is that of most practical importance, as it can be realized with comparatively low voltages.

A quadrupole mass filter can be used as a mass band-pass filter for an ion beam sent along the z-axis between the electrodes. Such a mass filter is part of the molecular ion source used in this work (Chapter 3.2). For fixed parameters r_0, Ω, U_{RF}, U_{DC} the (a, q)-pairs of all ions lie on the straight line with the slope $a/q = 2U_{DC}/U_{RF}$ (Fig. 2.3(b)). The intersections of this straight line with the radial stability region determine the maximum and minimum mass m_1 and m_2 that are yet radially confined. Thus, ions with masses $m_2 \leq m \leq m_1$ can pass the mass filter, and ions with masses outside this mass range are filtered out from the ion beam.

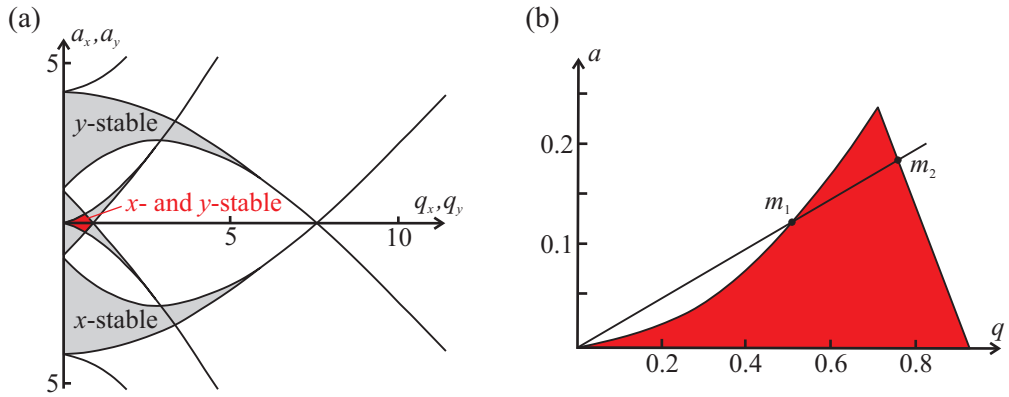

Figure 2.3: Stability diagram of the quadrupole mass filter. (a) Regions that allow for stable motion in x- or y-direction are colored in gray. Stable motion in the xy-plane is allowed for overlap regions colored in red. (b) Detailed view of the positive part of the first radial stability region.

2.1.2 Axial confinement

A three-dimensional confinement of ions can be achieved with a quadrupole mass filter by creating an additional potential minimum in axial direction using static electric fields. One of the numerous practical realizations is the linear quadrupole trap (Fig. 2.1). Here, a static voltage U_{EC}, applied to in total eight endcap electrodes added to the mass filter, creates an axial potential which close to the trap axis can be expressed as

$$\Phi_z = \kappa U_{EC} z^2 \tag{2.7}$$

according to [28, 29] with κ being a constant determined by the geometry and distance of the endcap electrodes.

The static electric field of the endcaps has a defocusing effect in radial direction, which weakens the radial confinement to some extent. With $U_{DC} = 0$, which is the common case in most applications and as well in this work, the radial potential of the linear quadrupole trap is given by

$$\Phi(x, y, t) = -\frac{U_{RF}\cos(\Omega t)}{2r_0^2}(x^2 - y^2) - \frac{1}{2}\kappa U_{EC}(x^2 + y^2). \tag{2.8}$$

As shown in the previous chapter, the resulting equations of motion in the xy-plane in this potential can be transformed to Matthieu differential equations

$$\frac{\partial^2 u}{\partial \tau^2} + (a_z - 2q_u\cos(2\tau))u = 0 \quad \text{with} \quad u = x, y, \tag{2.9}$$

but with the slightly different dimensionless parameters

$$\tau = \frac{\Omega t}{2}, \quad a_z = -\frac{4\kappa Q U_{EC}}{m\Omega^2}, \quad q = q_x = -q_y = \frac{2QU_{RF}}{mr_0^2\Omega^2}. \tag{2.10}$$

Fig. 2.4 shows the stability diagram of a linear quadrupole trap with its first stability region which is different from that of the quadrupole mass filter. For positively charged ions, stable trapping in axial direction is only possible for $a_z < 0$, i. e. for a positive voltage U_{EC} applied to the endcap electrodes. Another difference compared to the quadrupole mass filter is the fact that ions of an arbitrary low mass (arbitrary high q-parameter) in principle can be confined, as long as the endcap voltage U_{EC} can be set sufficiently high.

2.1.3 Ion motion in a linear quadrupole trap

The radial motion of an ion in a linear quadrupole trap is described by the solutions of the differential equation (2.9), that can be written as

$$u(t) = u_{max}\left(1 + \frac{q}{2}\cos(\Omega t)\right)\cos(\omega_r t) \quad \text{with} \quad u = x, y \tag{2.11}$$

in the case $-a_z, q \ll 1$ and with the radial secular frequency

$$\omega_r = \frac{\Omega}{2}\sqrt{\frac{q^2}{2} + a_z} \tag{2.12}$$

that, depending on a_z, is obviously reduced through the static field of the endcap electrodes.

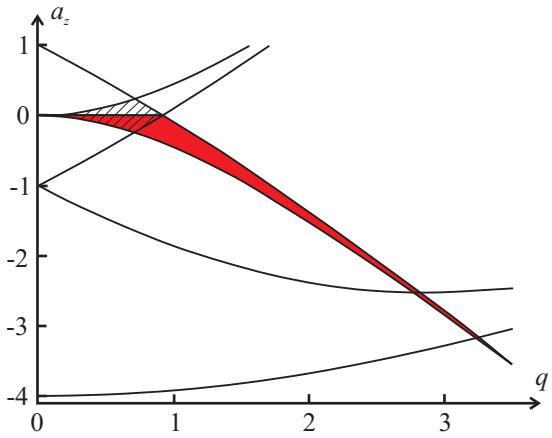

Figure 2.4: Stability diagram of the linear quadrupole trap. Colored in red is the first stability region of the linear quadrupole trap for positively charged ions. For comparison, the first radial stability region of the quadrupole mass filter is marked by hatching.

Eq. (2.11) describes a dominant motion of low frequency $\omega_r \ll \Omega$ with the amplitude u_{max}. Superimposed to this so-called *secular motion* is a fast jitter motion, the *micro-motion*, oscillating at the trap RF frequency Ω with a small amplitude (as $q \ll 1$) that is proportional to the distance from the trap axis. Thus, the secular motion can be seen as the time average of this composed motion and can be expressed as motion in a time independent harmonic pseudo potential Φ_{ps} with the oscillation frequency ω_r:

$$\Phi_{ps}(x,y) = \frac{1}{8} q U_{RF} \frac{x^2+y^2}{r_0^2} - \frac{1}{2}\kappa U_{EC}(x^2+y^2) \tag{2.13}$$

An expression for the three-dimensional time-independent pseudo potential of the linear quadrupole trap can be given by

$$\Phi_{ps}(r,z) = \frac{1}{2}\frac{m}{Q}\omega_r^2 r^2 + \frac{1}{2}\frac{m}{Q}\omega_z^2 z^2 \tag{2.14}$$

with $r^2 = x^2 + y^2$ and the axial oscillation frequency

$$\omega_z = \frac{\Omega}{2}\sqrt{-2a_z}. \tag{2.15}$$

According to [30] the depth of this pseudopotential in the middle of the trap at $z = 0$ is given by

$$\Phi_0 = \frac{QU_{RF}}{8} q, \tag{2.16}$$

meaning that ions with a higher kinetic energy than Φ_0, which is typically in the range of several electron volts, cannot be trapped.

It is important to note here, that the given radial secular frequency ω_r and the axial oscillation frequency ω_z are only valid in this strict form for a single ion confined in the trap. When more ions than one are trapped simultaneously, space charge effects become relevant and coupling effects between different ion species can lead to sometimes significantly shifted resonance frequencies as described in later chapters and for example in [31].

The secular temperature

In order to characterize the temperature of trapped ions, one has to distinguish between the energy contributions of the secular motion and the micromotion. The kinetic energy of the secular motion, where the regular micromotion oscillations are averaged out, can be taken as an indication of the temperature of the ions, since it arises from the disordered motion of the interacting ions in the time-independent trap pseudopotential. In contrast, the micromotion contribution to the total kinetic energy arises from a driven motion, which is limited to the radial direction in the linear quadrupole trap considered here.

In the context of our MD simulations (Chapter 4.3 and [32]) we have defined the temperature of an ion species as the secular temperature T via the secular kinetic energy $E_{sec} = \frac{3}{2}k_B T$ with

$$E_{sec} = \frac{m}{2}\frac{1}{N}\sum_{i}^{N}\left(\left\langle v_{ix}^2\right\rangle + \left\langle v_{iy}^2\right\rangle + \left\langle v_{iz}^2\right\rangle\right), \tag{2.17}$$

where m is the mass of the ions, N is the total number of ions of the considered species, and $\left\langle v_{i\alpha}^2\right\rangle$ is the squared velocity of ion i in direction α ($\alpha = x, y, z$) averaged over several RF oscillations periods.

RF heating

When ions collide with residual gas particles or other trapped ions, or are disturbed by electric noise, their motion can get out of phase with the trap RF field. As a consequence, kinetic energy from the micromotion can be irreversibly transferred to the secular motion, increasing the secular temperature which is known as RF heating. As the RF heating rate depends on various other factors, such as the trap parameters, the number of trapped ions and also the ion temperature, it can only be determined by elaborate MD simulations [33, 34, 32].

Qualitatively, the maximum increase of an ion's secular energy due to a collision can only be as high as the kinetic energy stored in its micromotion. According to [28] this micromotion energy is

$$E_{micro} = \frac{1}{2}m(\frac{1}{2}qr\Omega)^2, \tag{2.18}$$

thus, it increases for increasing radial distances r from the trap axis and makes it hard to cool large ensembles of ions. Here, an important advantage of linear quadrupole traps becomes apparent, as they provide a large trapping volume close to the trap axis, where micromotion is low and RF heating negligible. This allows for the preparation of huge ion crystals in linear quadrupole traps consisting of more than 10^5 ions [35].

Furthermore, RF heating strongly depends on the ion temperature and has been shown to be undetectable for temperatures below 0.5 K [34]. Consequently, RF heating is of low importance in the ion crystals produced and investigated in this work with usual temperatures of less than a few hundred millikelvin. But it can make it impossible to crystallize large and hot ion clouds, if cooling is not sufficient.

2.2 Cooling of trapped ions

Trapped ions are constantly heated, not only via RF heating, but also through direct transfer of kinetic energy in collisions with residual gas particles or, to a much smaller

extent, through electric noise on the trap electrodes. Without cooling, the kinetic energy of the ions can easily increase so much that it exceeds the trap potential depth (Eq. (2.16)) which leads to a loss of the trapped ions. Therefore, constant and sufficient cooling is essential in order to ensure stable trapping and to maintain cold ion ensembles.

Several techniques can be applied to cool ions in traps, such as resistive cooling [36, 37], buffer gas cooling [25], laser cooling [38, 39], or sympathetic cooling [40, 16, 41]. This section reports on the three last-mentioned techniques as they have been used in this work for translational cooling of atomic and molecular ions.

2.2.1 Cooling techniques

Buffer gas cooling

Buffer gas cooling is a very universal cooling technique, because it can be applied to all kinds of particles. Trapped ions, for example, can be cooled by collisions with a cold gas injected into the vacuum chamber that contains the trap. The cooling effect relies on elastic collisions of the trapped ions and the buffer gas particles, which lead to an equilibration of the ions' kinetic energies. When heating effects are negligible compared to the buffer gas cooling power, the minimum reachable ion temperature is that of the buffer gas. Thus, in order to reach temperatures in the Kelvin regime, cryogenic techniques need to be applied to cool the buffer gas and the trap apparatus.

As mentioned above (Chapter 2.1.3), in RF traps collisions of trapped ions with other particles can lead to RF heating. Thus, the buffer gas particles need to have lower masses than the ions that are to be cooled [25]. For higher masses, the RF heating overcomes the buffer gas cooling effect resulting in increasing ion temperatures. For this reason, in this work helium buffer gas is used to pre-cool complex molecular ions (Chapter 3.2) that have masses of more than 100 Da.

Using classical collision theory one can derive an expression for the ion-neutral collision cooling or heating rate as described in [42]. At low temperatures ($T < 300$ K) the most important ion-neutral interaction arises from an induced dipole attraction which has a potential $\varphi = -(\alpha/2)(e/4\pi\epsilon_0 r^2)^2$ for a singly charged ion. Here, α is the polarizability of the neutral atom or molecule, e the electron charge, and r the radial separation. According to [42] the collision cooling or heating rate is

$$h_{coll} = \frac{3(2.21)}{4}\frac{ek_B}{\epsilon_0} n_n \sqrt{\alpha\mu}\frac{T_n - T_c}{m_n + m_c}, \tag{2.19}$$

where n_n is the particle density of the neutral gas, m_n (m_c) and T_n (T_c) are the masses and temperatures of the neutrals (ions), and $\mu = m_n m_c/(m_n + m_c)$ is the reduced mass. For example, in a typical laser-cooled $^{138}Ba^+$ ion crystal, the heating rate due to collisions with room temperature N_2 molecules at $5 \cdot 10^{-10}$ mbar residual gas pressure is $h_{coll} = k_B(1.1\,\mathrm{K/s})$.

Laser cooling

The basic principle of laser cooling is a deceleration of particles by photon scattering based on a repeated absorption of directed photons and their undirected emission (see Fig. 2.5, a detailed treatment follows in Chapters 2.2.2 and 2.2.3). As the momentum of a photon transferred at each scattering process is very small, the particles need to relax to the initial ground state immediately in order to be available for the next absorption and emission

cycle. This need for closed optical transitions reduces the number of atom or ion species with a suitable simple electron configuration for laser cooling, and makes it generally not applicable to most of the molecules. Especially complex molecules, which are considered in this work, have numerous rovibrational levels, sometimes with long lifetimes, so that a direct application of laser cooling is impossible. However, laser cooling can be applied indirectly to arbitrary molecular species via sympathetic cooling in ion traps.

Sympathetic cooling

The basic idea of sympathetic cooling is simple: When two or more different ion species are trapped together in an ion trap and one of the species is laser-cooled, the other species will cool down as well due to Coulomb interaction. Through elastic Coulomb collisions, kinetic energy of the non-laser-cooled ions is transferred to the laser-cooled ions from where it is dissipated via laser cooling. In an ion crystal this mechanism leads to a thermal equilibrium between the laser-cooled and the sympathetically cooled ions. Sympathetic cooling is universally applicable to any kind of ions, atomic or molecular ones, as long as it can be stably trapped together with the laser-cooled atomic species. In our group sympathetic cooling has been used to cool ions covering the wide mass range from protons to proteins [43, 21].

Unlike buffer gas cooling, for sympathetic cooling there is no restriction in the masses of the interacting ion species. A laser-cooled ion species can sympathetically cool ions of higher mass, as well as ions of lower mass. MD simulations have shown [23] that the efficiency of sympathetic cooling does not significantly depend on the mass ratio of the laser-cooled and sympathetically cooled ions, but much more on the ratio of their mass-to-charge ratios.

As will be shown in Chapter 2.3, ion species of different mass-to-charge ratios radially separate in a quadrupole ion trap. Ions of lower mass-to-charge ratio arrange closer to the trap axis, simultaneously trapped ions of higher mass-to-charge ratio arrange around them at a higher radial distance from the trap axis. This radial separation determines the efficiency of sympathetic cooling. The spatially closer an ion species is to the laser-cooled ion species, the higher is the sympathetic cooling efficiency due to the stronger Coulomb interaction. For a linear quadrupole ion trap this means, sympathetic cooling is most efficient for ions of a mass-to-charge ratio similar to that of the laser cooled ion species. Therefore, in our group an ion trap apparatus with laser-cooled $^{9}Be^{+}$ ions is used to cool HD^{+} ions (mass-to-charge ratio = 3 Da), and another apparatus with 15 times more massive laser-cooled $^{138}Ba^{+}$for cooling complex molecular ions (mass-to-charge ratios $\approx$ 100 to 1100 Da).

Sympathetic cooling is so efficient that it enables the Coulomb crystallization of not directly laser-cooled ion species. To illustrate its high capability, two extreme experimental examples shall be mentioned here: In one case a single laser-cooled $^{24}Mg^{+}$ ion maintained order in a string of 14 sympathetically cooled $^{26}Mg^{+}$ ions (ratio of sympathetically cooled ions to laser-cooled ions = 14 : 1) at a temperature of 10 mK or lower [41]. In another case 20 laser-cooled $^{138}Ba^{+}$ ions were capable of maintaining the temperature of 120 sympathetically cooled barium isotopes ($^{135\text{-}137}Ba^{+}$) and 430 $^{138}Ba^{16}O^{+}$ molecules at approximately 25 mK (ratio of sympathetically cooled ions to laser-cooled ions = 27.5 : 1) [19].

2.2.2 Fundamentals of Doppler laser cooling

Doppler laser cooling can be applied to suitable neutral or charged atoms to quickly and effectively reduce their translational temperatures far below 1 K. Basically, it relies on a

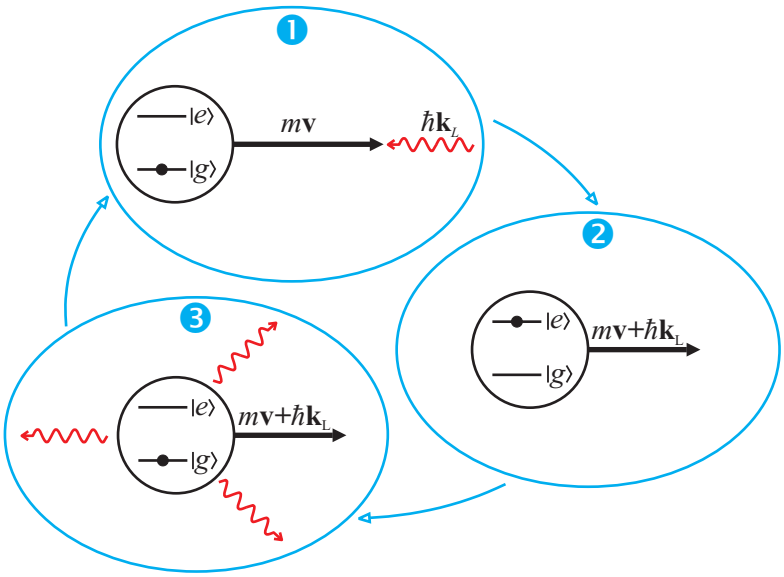

Figure 2.5: Illustration of a Doppler laser cooling cycle. (1) In the beginning the atom is in the ground state $|g\rangle$ and moving with the momentum $m\mathbf{v}$ towards a photon with the momentum $\hbar\mathbf{k}_L$. (2) By absorption of the photon the atom is excited to the state $|e\rangle$ and its momentum is reduced by the photon momentum. (3) Finally the atom emits a photon (each time in an arbitrary direction), returns to the ground state and is ready for the next absorption and emission cycle.

combination of momentum conservation and the Doppler effect. Assume an atom in a laser field, whose frequency ω_L is sligthly red-detuned compared to the transition frequency ω_A of the atom, i. e. $\omega_L < \omega_A$ (Fig. 2.5). Furthermore assume, that the atom moves with the velocity $\mathbf{v}$ against the laser beam characterized by the wave vector $\mathbf{k}_L$. Due to the Doppler effect, for the atom the laser frequency appears increased by the Doppler shift $\mathbf{k}_L \cdot \mathbf{v}$ and resonance occurs for the case when $\omega_A - \mathbf{k}_L \cdot \mathbf{v} = \omega_L$. When it absorbs a photon, the atom gains the photon momentum $\hbar\mathbf{k}_L$ in the direction of the laser beam and therefore is slowed down. An acceleration in direction of the red-detuned laser beam is not possible, as atoms moving in the laser propagation direction are off-resonant with the laser field and therefore a photon absorption is not possible. After the absorption the atom relaxes to the initial ground state by spontaneous emission and is ready for the next absorption. Since spontaneous emission is isotropic in space, the recoils due to photon emission cancel each other out over many cycles of absorption and emission. Thus, the only remaining effect is the deceleration due to absorption.

Doppler laser cooling can be quantitatively described by a semi-classical model that treats the atom quantum-mechanically as a two-level system and its motion classically. In the following, the main results of this model are given, a detailed treatment can be found in [44, 45].

The atom is treated as a closed two-level system with the ground state $|g\rangle$ and the excited state $|e\rangle$. The dipole transition $|g\rangle \rightarrow |e\rangle$ has the frequency ω_A and the excited state relaxes by spontaneous emission with the rate Γ. A light wave with the wave vector $\mathbf{k}_L$ and the frequency ω_L acts on the atom with the light force

$$F_{light} = \text{photon momentum} \cdot \text{photon scattering rate} = \hbar k_L \cdot \Gamma \rho_e. \tag{2.20}$$

Here, ρ_e is the population of the excited state that can be obtained from solving the optical

Bloch equations which yields

$$\rho_e = \frac{\Omega^2}{4\Delta^2 + \Gamma^2 + 2\Omega^2}, \tag{2.21}$$

where Ω is the Rabi frequency that determines the strength of the atom-light interaction, and $\Delta = \omega_L - \omega_A$ is the detuning of the light wave compared to the atomic transition. When the atom moves with the velocity $\mathbf{v}$, an additional Doppler shift $\mathbf{k}_L \cdot \mathbf{v}$ needs to be considered leading to the light force

$$F_{light} = \hbar k_L \Gamma \frac{\Omega^2}{4(\Delta - \mathbf{k}_L \cdot \mathbf{v})^2 + \Gamma^2 + 2\Omega^2}. \tag{2.22}$$

A Taylor expansion of this expression (2.22) for small velocities v leads to a simpler expression

$$F_{light} = F_{light,0} + \beta v + \mathcal{O}(v^2). \tag{2.23}$$

According to this, the light force is composed of two contributions − a constant force $F_{light,0}$ and a velocity dependent damping force βv with the damping coefficient

$$\beta = \hbar k_L^2 \frac{4S\frac{\Delta}{\Gamma}}{\left(1 + S + \left(\frac{2\Delta}{\Gamma}\right)^2\right)^2}. \tag{2.24}$$

Here, S is the the saturation parameter of the transition $|g\rangle \rightarrow |e\rangle$ in a resonant light field of the intensity I. With the saturation intensity I_{sat}, for which the population of the excited level $|e\rangle$ is 25 %, S can be given as

$$S = \frac{I}{I_{sat}} = \frac{2\Omega^2}{\Gamma^2} \quad \text{with} \quad I_{sat} = \frac{2\pi^2 \hbar c \Gamma}{3\lambda_L^3}. \tag{2.25}$$

For an ensemble of atomic ions with the above properties (two-level system, transition frequency ω_A etc.) confined in a linear quadrupole trap and exposed to a laser beam of frequency ω_L directed along the trap axis, this light force has the following effects: The constant force $F_{light,0}$, which is typically on the order of 10^{-20} N, causes a shift of the ions from the trap center in the propagation direction of the laser beam by a few micrometers. The velocity dependent damping force βv decelerates ions that move against the laser propagation direction ($v < 0$), when the damping coefficient β is negative. This is the case for red-detuned laser light, i. e. for negative values of the detuning Δ. Thus, the ions would be accelerated for blue-detuned laser light. Fig. 2.6 shows the damping coefficient β depending on the detuning Δ for different saturation parameters S. The strongest damping, i. e. the strongest cooling, is achieved for a red-detuning of the laser light by half the transition linewidth $\Delta = -\Gamma/2$ at an intensity twice as high as the saturation intensity $I = 2I_{sat}$.

Note that in an ion trap it is sufficient to use a single laser beam for cooling the ions. Although this only damps the motion along the propagation direction of the laser beam, the interaction of the ions and the trap confinement couple the ion motion leading to an effective translational cooling in all three dimensions.

Neglecting all possible heating effects, the minimum temperature reachable with Doppler laser cooling is still limited. Due to the repeated photon emissions in arbitrary directions, a laser cooled atom performs a random walk in momentum space [45]. The finite width of the according momentum distribution is the so-called Doppler limit characterized by the Doppler temperature

$$T_{Doppler} = \frac{\hbar \Gamma}{2k_B}. \tag{2.26}$$

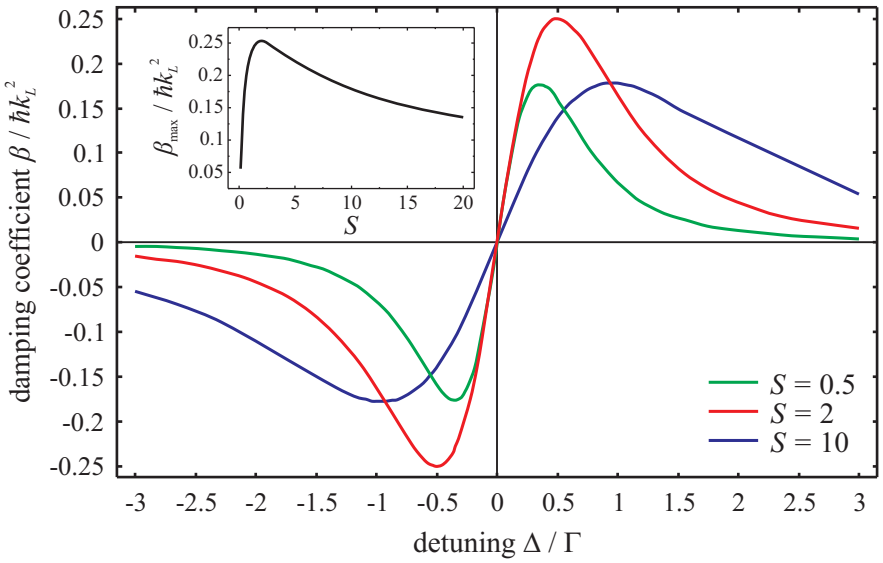

Figure 2.6: Damping coefficient in the two-level system. The damping coefficient β is shown for different saturation parameters S depending on the detuning Δ. The inset shows the maximum values for β as a function of S. For $\Delta = -\Gamma/2$ and $S = 2$ the damping coefficient β reaches its absolute maximum value.

For the laser-cooled barium ions used in this work the Doppler limit is at $T_{Doppler} \approx 480$ µK. However, this temperature can only be reached under ideal conditions for a single ion in the trap center with all heating effects reduced to a minimum.

2.2.3 Doppler laser cooling of $^{138}Ba^+$ ions

Barium (symbol Ba) is a chemical element with the atomic number 56, belonging to the alkaline earth metal group. Elementary barium is soft and silvery, and very reactive with oxygen and water. There are seven stable isotopes as shown in Tab. 2.1 with their relative abundances in natural barium metal.

isotope	^{138}Ba	^{137}Ba	^{136}Ba	^{135}Ba	^{134}Ba	^{132}Ba	^{130}Ba
relative abundance	71.7 %	11.3 %	7.8 %	6.6 %	2.4 %	0.1 %	0.1 %
isotope shift / MHz	0	+179.9	+143.9	+332.8	+287.8	-	-
nuclear spin	0	$\frac{3}{2}\hbar$	0	$\frac{3}{2}\hbar$	0	0	0

Table 2.1: Barium isotopes. Overview of the stable barium isotopes with their relative abundances in natural barium, the isotope shifts of the ($6^2S_{1/2} \rightarrow 6^2P_{1/2}$) cooling transition, and their nuclear spins [46].

In this work, $^{138}Ba^+$ ions from natural barium have been laser-cooled and used for sympathetic cooling of molecular ions. During the production of the $^{138}Ba^+$ ions, all other isotopes are also ionized and trapped simultaneously, but cannot be laser-cooled due to two different reasons. The isotopes with an odd nucleon number have a nuclear spin of $\frac{3}{2}\hbar$ and the resulting hyperfine interaction causes energy level schemes that are different from that of $^{138}Ba^+$. For the other isotopes with an even nuclear number, where the nuclear spin is 0 and there is no hyperfine interaction, the isotope shifts of the cooling transition are so high (> 100 MHz, see Tab. 2.1), that they are off-resonant with the cooling laser.

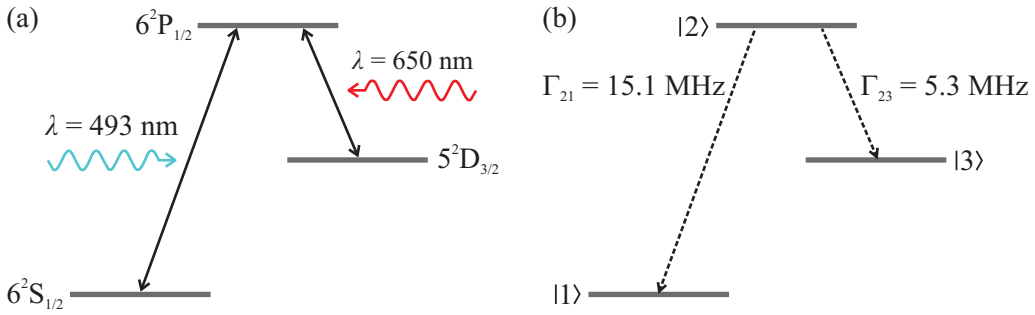

Figure 2.7: Level scheme of Ba^+. (a) Extract from the energy level scheme of singly ionized barium with terms and wavelengths needed for Doppler laser cooling. (b) Rates of spontaneous emission [48].

Fig. 2.7(a) shows an extract from the energy level scheme of singly ionized barium with the two transitions relevant for Doppler laser cooling. The cooling transition is the ($6^2S_{1/2} \rightarrow 6^2P_{1/2}$) transition, which can be excited by a laser with a wavelength of 493 nm (in the following denoted as *cooling laser*). The rates of spontaneous emission of the excited state $6^2P_{1/2}$ given in Fig. 2.7(b) show, that the excited state relaxes to the ground state $6^2S_{1/2}$ and the intermediate state $5^2D_{3/2}$ with a branching ratio of about 3:1. As the intermediate state is metastable with a lifetime of about 80 s [47], an additional laser at 650 nm (in the following denoted as *repumping laser*) driving the ($5^2D_{3/2} \rightarrow 6^2P_{1/2}$) transition is necessary to deplete the intermediate state in order to establish a closed laser cooling cycle.

Thus, the Doppler laser cooling of singly ionized barium relies on the interaction of two lasers with a three-level system, which can be quantitatively described with the same semi-classical approach as the Doppler laser cooling in a two-level system (Chapter 2.2.2). According to [22] for this three-level case the light force takes the form

$$F_{light} = \hbar k_{L,12} \Gamma_{21} \rho_2 + \hbar k_{L,32} \Gamma_{23} \rho_2, \tag{2.27}$$

where Γ_{ij} is the rate of spontaneous emission of the transition $|i\rangle \rightarrow |j\rangle$ with the energy levels as labeled in Fig. 2.7(b), and $\hbar k_{L,ji}$ is the momentum transfer to the atom absorbing a photon with the wave vector $k_{L,ji}$. The population ρ_2 of the excited state $|2\rangle$ depends on the emission rates Γ_{ij} and the Rabi frequencies Ω_{ij}. It can be obtained from solving the optical Bloch equations, that describe the interaction of the light fields with the three-level system.

Special for three-level systems are the so-called dark resonances, that complicate the laser cooling of barium ions. Dark resonances are coherent superpositions of quantum states occurring at certain detunings of the laser frequencies, for which the population of the excited state is almost zero. Thus, at dark resonances the ions do not fluoresce and laser cooling is not possible. Fig. 2.8 shows the rate of fluorescence $\Gamma_{21}\rho_2$ for different detunings Δ_{493} of the cooling laser depending on the detuning Δ_{650} of the repumping laser. Apparently, dark resonances occur for both detunings being equal, i. e. for $\Delta_{493} = \Delta_{650}$, which is in the strict sense only valid for the shown case of a saturation parameter $S = 2$ and only approximately valid for other values.

Note that high fluorescence does not mean high damping, as mentioned in the description of the two-level system, where damping is at its maximum for the cooling laser detuned by half the transition linewidth $\Delta = -\Gamma/2$ at an intensity twice as high as the saturation intensity $I = 2I_{sat}$. In a three-level system, such a simple condition cannot be given due to the existence of dark resonances. Fig. 2.9 illustrates the complexity of the strength of the damping coefficient β in the three-level system of singly ionized barium for the case of

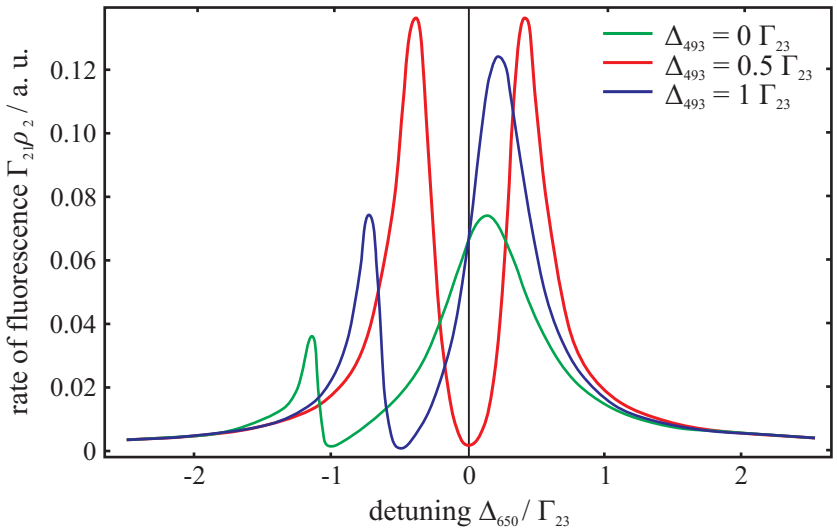

Figure 2.8: Dark resonances in a three-level system. The rate of fluorescence $\Gamma_{21}\rho_2$ is shown for different detunings Δ_{493} of the cooling laser depending on the detuning Δ_{650} of the repumping laser for double saturation ($S = 2$) [22]. Dark resonances with the rate of fluorescence falling to zero occur for $\Delta_{493} = \Delta_{650}$.

low and single saturation. Here, white areas stand for a high damping force, i. e. strong cooling, and dark areas stand for negative damping, i. e. heating. To find the ideal laser detunings for the cooling and the repumping laser is a challenging task in the experimental cooling of barium ions.

Another aspect of laser cooling of barium ions that has to be considered, is the degeneracy of the three levels in absence of a magnetic field. With no suitable magnetic field applied, optical pumping to states can occur which cannot spontaneously decay to the initial ground state. Ions in such states would be excluded from laser cooling. This can be avoided by the application of a magnetic field with an orientation parallel to the trap axis and the use of a linearly polarized cooling and repumping laser with the polarization axis orthogonal to the magnetic field. In this way, the degeneracy of the three states is removed and optical excitation is possible for all Zeeman states. A detailed description of this problem can be found in [22]. The Zeeman splitting makes the description of the laser cooling force even more complicated as further dark resonances occur. This has been investigated for barium ions by Reiß et al. [49].

2.3 Coulomb ion crystals

2.3.1 Coulomb crystallization

The motion of ions confined in a linear quadrupole trap is determined by the trap potential as described in Chapter 2.1.2 in Eq. (2.14)

$$\Phi_{ps}(r,z) = \frac{1}{2}\frac{m}{Q}\omega_r^2 r^2 + \frac{1}{2}\frac{m}{Q}\omega_z^2 z^2$$

and their mutual Coulomb interaction

$$\Phi_{C,i} = \frac{1}{4\pi\epsilon_0}\sum_j \frac{Q_j}{r_{ij}}. \tag{2.28}$$

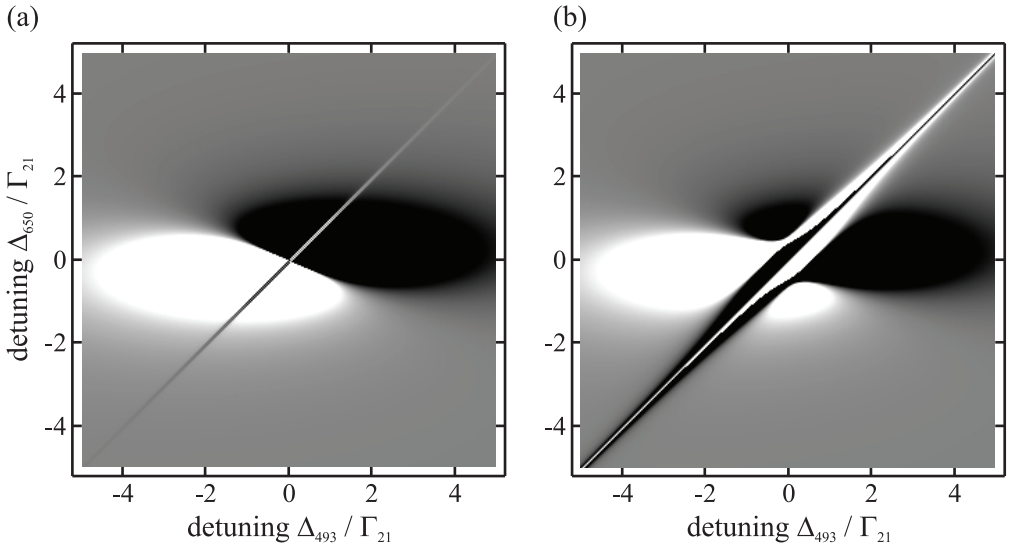

Figure 2.9: Damping coefficient in a three level system. The damping coefficient β for the three-level system $^{138}Ba^{+}$ is shown depending on the detunings of the cooling laser Δ_{493} and the repumping laser Δ_{650} for (a) low and (b) single saturation. White areas stand for a high damping force (strong cooling) and dark areas for a negative damping force (heating) [22].

Here, $\Phi_{C,i}$ is the electric potential at the position of the ion i caused by all other ions j with the charges Q_j at distances r_{ij}. While the ions are confined to the trap center by the trap potential, they electrostatically repulse each other. With no cooling applied, the result is a diffuse ion cloud in which the ions move in a disordered way with their thermal velocities.

When the translational energy of the ion ensemble is sufficiently reduced by laser cooling, a liquid-solid phase transition occurs with the ion ensemble changing from a disordered ion cloud to an ordered ion crystal (Fig. 2.10). Essential for the occurrence of this so-called Coulomb crystallization is the dominance of the particles' interaction over their disturbing translational motion. This can be quantified by the plasma coupling parameter

$$\Gamma = \frac{Q^2}{4\pi\epsilon_0 a_{WS}} \frac{1}{k_B T}, \tag{2.29}$$

which is the ratio of the interaction energy between neighboring particles and the thermal energy per degree of freedom. Here, a_{WS} is the Wigner-Seitz radius that is defined as the radius of the sphere with a volume equal to the volume per ion,

$$a_{WS} = \left(\frac{3}{4\pi n_0}\right)^{1/3}, \tag{2.30}$$

where n_0 is the ion density.

Trapped ion ensembles, and non-neutral plasmas in general, are governed by the size of the plasma coupling parameter Γ. For $\Gamma \gtrsim 1$ a plasma is referred as strongly coupled. For $\Gamma \gtrsim 2$ MD simulations of infinite non-neutral plasmas predict a phase transition to a liquid state, characterized by the emergence of a short-range order [50, 51]. And for $\Gamma \gtrsim 170$ MD simulations and thermodynamic approaches predict the above-mentioned phase transition to a solid state, i. e. the emergence of long-range order [52, 51]. In this work, theoretical studies on this phase transition of Coulomb crystallization have been performed which

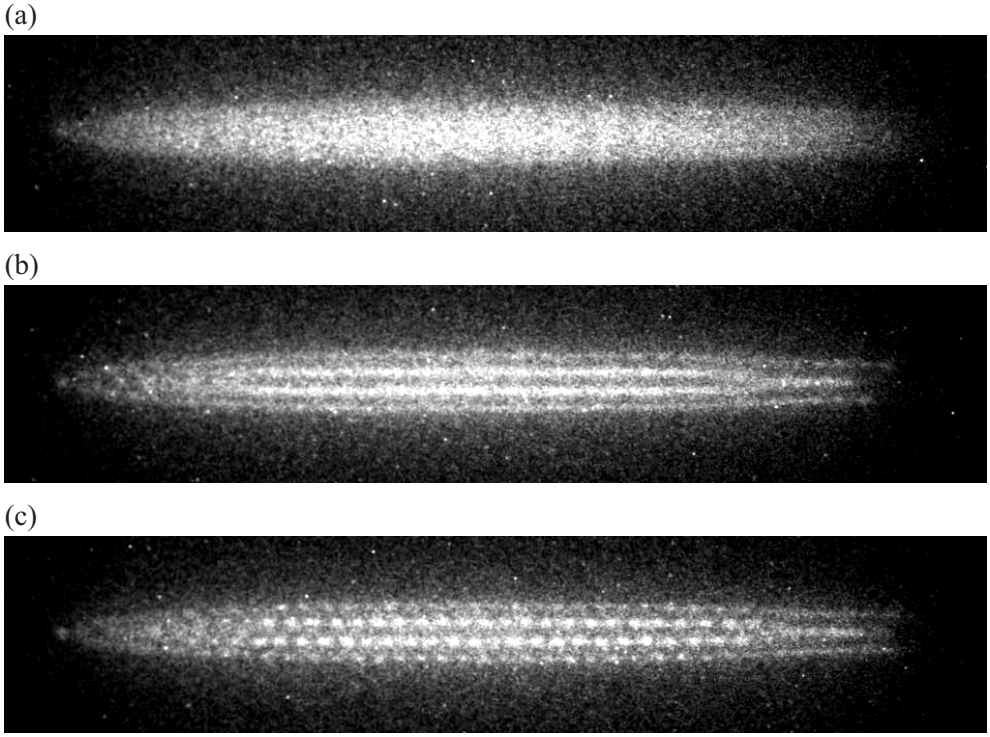

Figure 2.10: Coulomb crystallization of a $^{138}Ba^{+}$ ensemble. By adjusting the cooling and repumping laser frequencies, an initially diffuse cloud of $^{138}Ba^{+}$ ion (a) cools down. First structures appear (b) before it finally crystallizes (c).

are presented in detail in Chapter 8. The value of Γ and the corresponding temperature T at which the Coulomb crystallization sets in depends on several parameters, such as those defining the trap potential and especially the number of trapped ions. Therefore, no exact and generally applicable value can be given, but an approximate value for the ion ensembles considered in this work is < 10 mK.

2.3.2 Ion crystal structures

The appearance of ion crystals in a linear quadrupole trap depends on three factors − the ratio of the strength of radial and axial confinement, the ion number and the mass-to-charge ratios of the involved ion species.

Fig. 2.11 shows CCD images of differently structured single-species ion crystals consisting of Ba^{+} ions only. In a linear ion trap, low numbers of ions arrange along the trap axis forming strings of ions as shown in Fig. 2.11(a). When more ions are trapped, they arrange in concentric shells forming cigar-shaped, prolate ion crystals (Fig. 2.11(b) - (d)). For a stronger axial confinement or a weaker radial confinement, ion crystals axially shrink and radially expand as shown in Fig. 2.11(b) and (c). This ratio of radial and axial confinement can be described by the ratio of the radial and the axial resonance frequencies ω_r (Eq. (2.12)) and ω_z (Eq. (2.15)). For $\omega_r > \omega_z$ ion crystals have the prolate shape as shown in Fig. 2.11, and for $\omega_r = \omega_z$ ion crystals are of spherical symmetry. However, this cannot be achieved with the ion trap used in this work, as it is designed to produce prolate ion crystals that benefit from the low distance of the ions to the trap axis where micromotion is low.

It is important to note that the dots in the CCD images of ion crystals do not necessarily correspond to single ions. With their residual translational energies, the ions move around

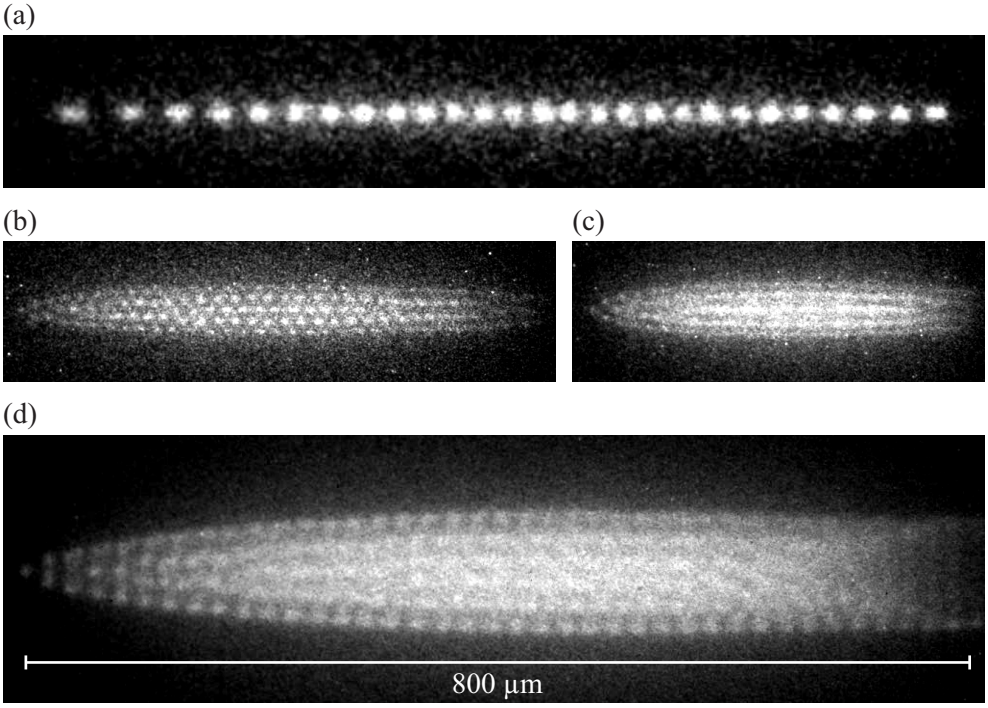

Figure 2.11: Ion crystal structures. CCD images of $^{138}Ba^{+}$ ion crystals consisting of different ion numbers acquired with two seconds exposure time. Image (a) shows a string of barium ions arranged along the trap axis. The images (b) and (c) show the same ion ensemble, but (c) was taken at a higher axial confinement, which makes the ion crystal shrink axially and expand radially. The ion crystal shown in image (d) consists of $\approx$ 600 $^{138}Ba^{+}$ ions at a temperature of $T \approx 6$ mK as determined via MD simulations.

their position in the ion crystal or even change their sites, moving axially within a shell or to neighboring shells (see also Chapter 8). Therefore, with a typical exposure time of the CCD camera of two seconds, spanning thousands of secular oscillation periods, these dots rather have to be interpreted as places of a high spatial probability density.

In multi-species ion crystals, ions of different mass-to-charge ratio $\frac{m}{Q}$ radially separate due to their different effective radial trap potentials

$$\Phi \propto \frac{Q}{m} r^2 \tag{2.31}$$

and the interspecies repulsion $\sim Q_1 Q_2$ [32]. For prolate ion crystals, this radial separation scales as

$$\frac{r_1}{r_2} \simeq \sqrt{\frac{m_1/Q_1}{m_2/Q_2}} \tag{2.32}$$

with the outer radius r_1 of the lower mass-to-charge ratio m_1/Q_1 subensemble and the inner radius r_2 of the higher mass-to-charge ratio m_2/Q_2 subensemble as illustrated in Fig. 2.12(b) [53].

Fig. 2.12 illustrates this radial separation in a simulated three-species ion crystal consisting of ions of the mass-to-charge ratios 50 Da (red), 138 Da (blue) and 300 Da (green). According to Eq. (2.31), ions of a low mass-to-charge ratio feel a strong radial confinement,

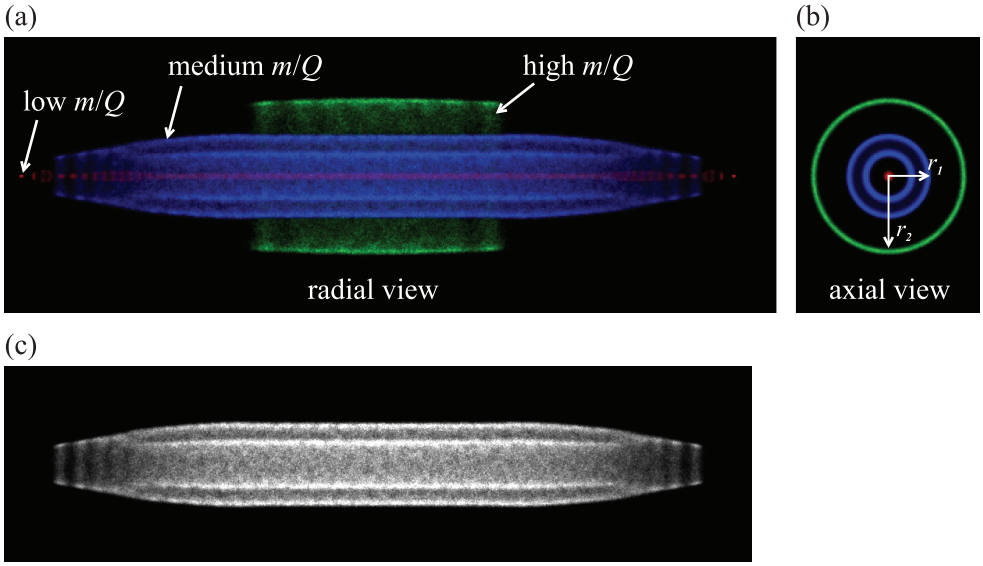

Figure 2.12: Ion species separation. Simulated images of an ion crystal consisting of 70 ions with a mass-to-charge ratio of 50 Da (red), 500 ions of 138 Da (blue), and 100 ions of 300 Da (green). (a, b) Ions of lower mass-to-charge ratios arrange closer to the trap axis, and ions of higher mass-to-charge ratios arrange around these ions. (c) Simulated CCD image of the ion crystal shown in (a) as it would be seen in the experiment, where only the fluorescing laser-cooled ions are visible.

and therefore arrange closer to the trap axis than ions of higher mass-to-charge ratios that arrange around them at radial distances described by Eq. (2.32). In a laser-cooled $^{138}Ba^+$ ion crystal this means that ions with $\frac{m}{Q} < 138\,\mathrm{Da}$ form a core in the barium ion subensemble, and ions with $\frac{m}{Q} > 138\,\mathrm{Da}$ form a sheath around the barium ions, as shown in Fig.2.12(a). As only the laser-cooled $^{138}Ba^+$ ions do fluoresce, they are the only species that can be detected by the CCD camera (Fig. 2.12(c)). Consequently, sympathetically cooled ions are not visible, but they cause deformations of the observed barium ion crystals from which one can derive their numbers, and, analyzing the structures in further detail, even their temperatures, as described in Chapters 4.3 and 5.

The constant light pressure force (Eq. (2.23)) that acts on the laser-cooled ions only, is another factor that influences the structure of ion crystals. In all experimental and simulated CCD images in this work, the cooling laser propagates from right to left, so it shifts the laser-cooled $^{138}Ba^+$ ions slightly to the left. Sympathetically cooled ion species are not influenced by the light pressure leading to an axial asymmetry of the multi-species ion crystals (for simplicity not considered in Fig. 2.12).

For the barium isotope ions, which are always produced and trapped simultaneously with the $^{138}Ba^+$ ions, this has the following consequence: Their mass-to-charge ratios are so similar to that of the $^{138}Ba^+$ ions, that there is no strong radial separation. But due to the light pressure acting on the $^{138}Ba^+$ ions, the laser-cooled and the sympathetically cooled barium ions are axially separated with the isotope ions arranging on the right side of the crystals. This can be seen in Fig. 2.10 and 2.11 and further images within this work, where the isotope ions cause the $^{138}Ba^+$ ion subensembles to have a differently shaped ending on the right than on the left side.

3 Experimental setup

The apparatus used and extended within this project is a unique setup for sympathetic cooling of complex molecular ions to millikelvin temperatures. Its special feature is the use of a molecular ion source based on electrospray ionization that allows for the production of gas-phase molecular ions of almost arbitrary species with a maximum mass-to-charge ratio of 2000 Da (Chapter 3.2).

With an octopole ion guide, the produced molecular ions can be transferred to a linear quadrupole trap (Chapter 3.3). There, at ultra-high vacuum (UHV) conditions and in the presence of simultaneously trapped laser-cooled barium ions (Chapter 3.4), they can be stored, kept cold and investigated for many minutes and in principle for up to hours.

3.1 Vacuum system

As the electrospray ionization takes place at atmospheric pressure and the achievement of millikelvin temperatures using laser cooling requires ultra-high vacuum conditions, high demands are made on the vacuum system. In this apparatus, both conditions are fulfilled using a differentially pumped vacuum setup (Fig. 3.1) that provides a pressure gradient of more than 13 orders of magnitude, sustained by in total 11 vacuum pumps (Tab. 3.1).

In the molecular ion source, a solution containing the desired molecular species is sprayed at atmospheric pressure towards a heated capillary with an inner diameter of 0.4 mm (as described in detail in Chapter 3.2). This capillary of about 11 cm length represents the first stage of the differential vacuum. It connects the electrospray region at atmospheric pressure (1000 mbar) with the skimmer region (Fig. 3.2) at 1 mbar, which is pumped by a strong rotary vane pump (R1). Behind the skimmer, in a region of less than 0.1 mbar pumped by a turbopump (T1), the stream of molecular ions is transferred to a quadrupole mass filter with a short octopole ion guide. This mass filter is placed in a high vacuum chamber at about 10^{-6} mbar, which is pumped by a second turbopump (T2) of the same type. Both turbopumps share the same rotary vane pump (R2) as forepump. Behind the mass filter, the molecular ions are coupled into a two meter long radio frequency octopole ion guide which transfers the ions to the linear quadrupole ion trap (technical details about the octopole can be found in [54, 22, 23]).

The part of the vacuum system described so far is sealed with elastomer gaskets, in the following part, operated at ultra-high vacuum pressures, CF flanges with copper gaskets are used. Along the octopole ion guide the pressure decreases by another seven orders of magnitude achieved by two turbo pumps (T3 and T4), which are fore-pumped by a common rotary vane pump (R3).

The end of the octopole ion guide extends into the linear quadrupole trap by a few millimeters in order to avoid a spatial gap with no radial confinement. The ion trap itself is placed in a vacuum chamber at ultra-high vacuum conditions which is pumped by a turbopump (T5) that uses another turbopump (T6) as its forepump in order to achieve a higher compression rate. Turbopump T6 itself is fore-pumped by a rotary vane pump (R4). A self-made titanium sublimation pump (S1) is installed in the bottom of the ion

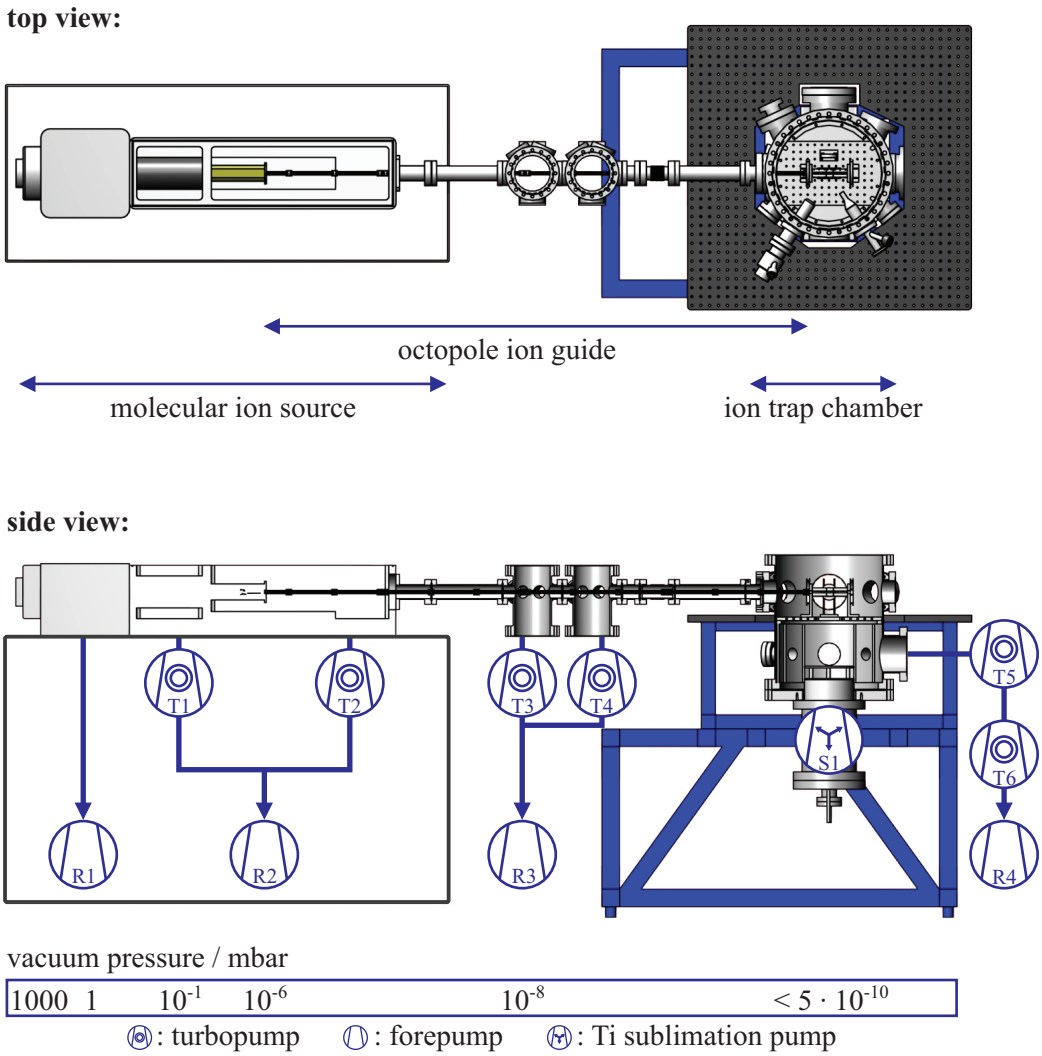

Figure 3.1: Overview of the vacuum setup. Top and side view of the vacuum setup consisting of the electrospray ionization (ESI) molecular ion source, the octopole ion guide, and the ion trap vacuum chamber in which the molecular ions are trapped, cooled and manipulated in a linear quadrupole ion trap. The vacuum pressure in the differential vacuum setup decreases from atmospheric pressure at the molecular ion source inlet to ultra-high vacuum values in the ion trap chamber (scale drawings from [22]).

pump	R1	R2	R3	R4	T1	T2	T3	T4	T5	T6
type	rotary vane pump				turbopump					
pumping speed	30	13	8	16	330	330	210	520	520	210
unit	m^3/h				l/s					

Table 3.1: Overview of used vacuum pumps. All mechanical pumps are listed here, not listed is the titanium sublimation pump (S1), which has an initial pumping speed of 1500 to 4500 l/s depending on the absorbed gas species (see Tab. 3.2).

gas type	H_2	N_2	O_2	CO	CO_2	H_2O	CH_4	Ar	He
pumping speed per area / $ls^{-1}cm^{-2}$	3.1	4.7	9.3	9.3	7.8	3.1	0	0	0

Table 3.2: Pumping speed of titanium layers. The table shows the initial pumping speeds per area of a titanium layer at room temperature for typical residual gas species [22].

trap chamber to achieve a final pressure of less than $5 \cdot 10^{-10}$ mbar, which is not possible by turbopumps alone. Additionally, sublimation pumps are capable of removing hydrogen much more efficiently than turbopumps, but in contrast, turbopumps are much more efficient in removing noble gases. The titanium sublimation pump has an active absorption surface of about 500 cm^2. Its pumping speed strongly depends on the absorbed gas species an ranges from 1500 to 4500 l/s (Tab. 3.2).

In order to trap molecular ions entering the ion trap through the octopole ion guide, a buffer gas (typically helium) needs to be injected into the ion trap chamber to slow down the molecular ions (Chapter 5.1). With this configuration of vacuum pumps, not only the required pressures in the 10^{-10} mbar range can be achieved, but also helium partial pressures of up to 10^{-5} mbar can be sustained for minutes and removed within seconds. The vacuum pressure in the ion trap chamber is measured with a hot cathode ionization gauge that has a lower limit of $5 \cdot 10^{-11}$ mbar. With a residual gas analyzer the partial pressures of gas species in a mass range of 1 to 100 Da can be determined.

To sustain the ultra-high vacuum in the ion trap chamber, all vacuum pumps need to run continuously. A power blackout longer than a minute will lead to an irrecoverable loss of the ultra-high vacuum. Reason for this is the intrusion of moist ambient air into the trap chamber which is constantly sucked into the vacuum system through the heated capillary, but no longer removed by the vacuum pumps (mainly T1 and T2) when they are off. The ultra-high vacuum can only be recovered by baking the ion trap chamber at about 200 °C for a few days to remove the intruded water. Furthermore, a loss of the vacuum leads to the oxidation of the elementary barium stored in the ion trap chamber, which needs to be replaced in such a case. To prevent the loss of the ultra-high vacuum, an uninteruptable power supply (UPS) with a maximum power capacity of 7000 W has been installed. In case of a power blackout it can supply the vacuum pumps with a total power of about 2500 W in sustainment mode for more than half an hour.

3.2 Molecular ion source

There are various techniques to produce gas-phase molecular ions, for example based on electron or photon impact ionization, on charge exchange reactions, or on thermal or electric desorption. In most of these methods, the energy applied for evaporation and ionization leads to a fragmentation of the molecules, especially in the case of more complex molecules. For mass spectrometry, where molecules are ionized to measure their mass-to-charge ratio, several techniques have been developed that can be applied even to such complex molecular species as biomolecules. Most important for modern biochemical mass spectrometry are the matrix-assisted laser desorption ionization (MALDI) [55] and the electrospray ionization (ESI) [56, 57, 58]. For MALDI, the desired molecules are implemented in a matrix that contains chromophores. By laser irradiation of these chromophores, the sample is locally heated so that the molecules evaporate and get ionized in a gentle way. With this method, gas-phase molecular ions with masses up to 500,000 Da and low charge numbers of one to three elementary charges can been produced.

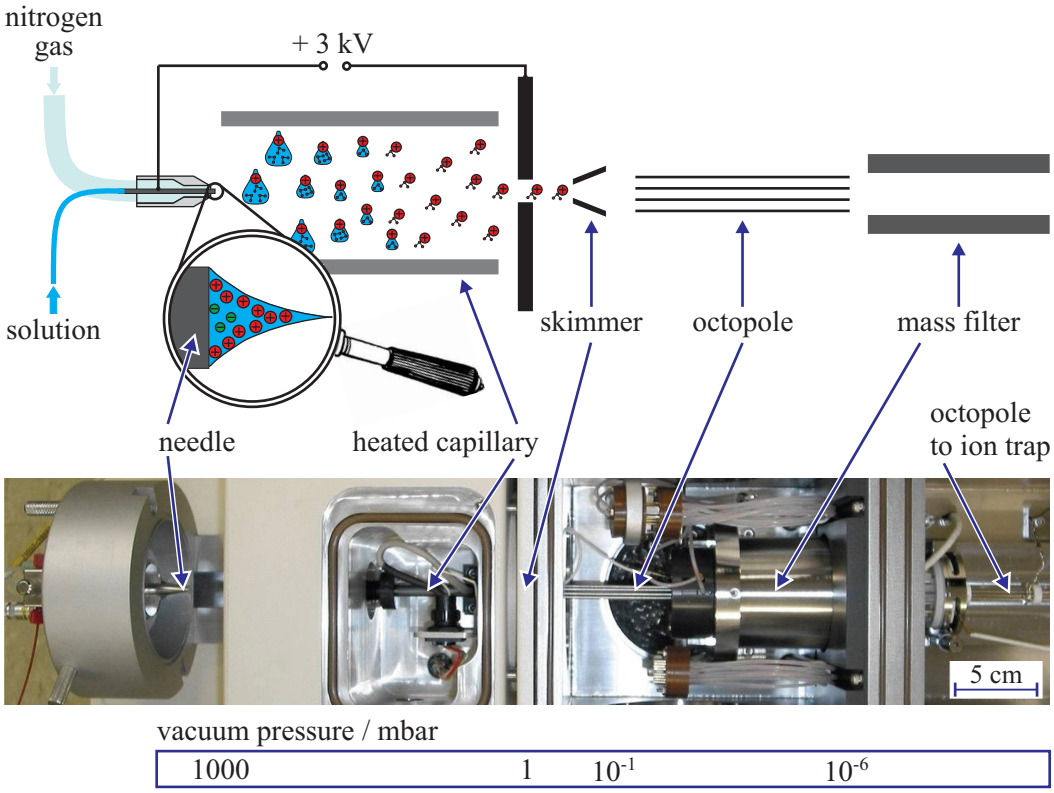

Figure 3.2: Principle and setup of the molecular ion source. The upper schematic diagram (not to scale) illustrates the principle of electrospray ionization as described in the text. The lower photo shows the unclosed molecular ion source with the needle through which the solution with the molecular ions is sprayed, the heated capillary in which the solvent evaporates, the skimmer (covered by housing components) which serves as aperture, a short octopole used as ion guide, the quadrupole mass filter for selection of the ion species to be transferred to the ion trap, and the beginning of the two meters long octopole which transfers the molecular ions to the ion trap. The pressures given below are approximate values for the atmospheric pressure region (1000 mbar), the skimmer region (1 mbar), the octopole region (10^{-1} mbar), and the following high vacuum region (10^{-6} mbar).

However, for our application, ESI is more suitable as samples of different molecules can be produced and exchanged much easier. These samples are solutions of the desired molecular species with typical concentrations in the range of 1 to 100 µmol/l. As solvent, volatile substances, such as methanol, ethanol, acetonitrile or mixtures of those and often in combination with water are used, chosen depending on the solubility of the molecular species. A crucial point is the addition of acids to the solution, typically in concentrations of a hundredth to a few percent. Protons from the acid attach to the solved molecules at basic sites, leading to singly or multiply charged molecular ions. Here, the number of charges, i. e. the grade of protonation, depends on the acid concentration, the size of the molecules and the availability of basic sites in the molecule, for example free electron pairs at nitrogen atoms (see also Chapter 5.2.1). Multiple protonation is an outstanding advantage of the ESI method as it allows one to reduce the mass-to-charge ratio of biomolecules, such as proteins or peptides with masses of more than 10 kDa, making them accessible for conventional mass spectrometers.

In an ESI apparatus, such a solution is sprayed at atmospheric pressure through a thin

metal needle of a few hundred micrometer inner diameter to which a positive high voltage of several kilovolts is applied (Fig. 3.2), at fluxes of about 10 µl/min. Around the needle, nitrogen gas streams out that shapes the leaking solution to a so-called Taylor cone. Due to the positive high voltage, the protonated molecular ions in the solution are pushed to the tip of this cone. Again and again, droplets break off from the tip of the Taylor cone, which only contain these protonated molecular ions and the solvent − separated from other negatively charged ions. These droplets are sprayed towards the inlet of the vacuum system, a heated capillary, that has a temperature of 200 °C and an inner diameter of 400 µm in our case. In this capillary, the solvent evaporates so that the droplets shrink and the surface charge of the droplets increases to a critical point known as the Rayleigh stability limit. At this critical point the droplets divide into smaller droplets with less molecular ions. This process repeats over and over until single gas-phase molecular ions remain.

The molecular ion source used in this work is a modified ESI-based commercial mass spectrometer (*Finnigan* SSQ700, Fig. 3.2). Here, the divergent stream of molecular ions from the heated capillary first passes a so-called skimmer which serves as an aperture to form a beam. At this point, this beam of ions contains a vast variety of molecular species, among them the molecules in different charge states, but also fragments, impurities, and adducts of the molecules with other particles from the solution. In order to remove all unwanted species, the ion beam is guided via a short octopole to a quadrupole mass filter that works as a band pass filter as described in Chapter 2.1.2. Mass-to-charge ratios of up to 2000 Da can be set for transmission with an adjustable bandwidth. Behind the mass filter, the purified beam of the desired molecular species is coupled into the octopole ion guide, which transfers the ions from the high-vacuum region of the ion source to the linear quadrupole ion trap in its ultra-high vacuum environment.

3.3 Trap setup

The linear quadrupole ion trap is placed in a cylindrical vacuum chamber with a diameter of 300 mm (Fig. 3.3). Optical viewports at height of the trap axis provide optical access to the trapped ions in radial and axial directions. The cooling and the repumping laser, as well as UV lasers for dissociation or IR lasers for spectroscopy, can be aligned along the trap axis through an axially mounted sapphire viewport.

The 493 nm fluorescence light from the trapped laser-cooled $^{138}Ba^{+}$ ions is collimated by two radially arranged lenses, both with a focal length of $f = 50\,\mathrm{mm}$, and directed to a CCD camera and a photomultiplier (PMT) outside the vacuum chamber through radial glass viewports. On the PMT side, the collimated light is focused with an $f = 100\,\mathrm{mm}$ objective to an aperture in order to reduce scattered light. An additional narrow-band filter at 493 nm between this aperture and the PMT eliminates all other wavelengths than the laser cooling light. Count rates of up to 10^6 photons/s at a background of a few hundred photons/s can be reached. On the CCD side, an $f = 400\,\mathrm{mm}$ achromat lens is used to image the trapped ion crystals to the 1024 x 1024 pixel detector chip of an intensified CCD camera, which has a quantum efficiency of about 40 % at 493 nm. Here, the same type of narrow-band filter at 493 nm is used. With the two lenses in this configuration, a magnification of 12.9 is achieved with a scaling factor of 1.03 µm/pixel. By imaging a micrometer scale on a glass plate in the trap center, the optical resolution could be determined to be better than 10 µm. This is sufficient to resolve single lattice sites in ion crystals with typical Wigner-Seitz radii of about 15 µm.

The barium ions are created in a UHV suitable evaporator, which contains about 1 g of elementary natural barium metal, being enough for many years of experiments. The

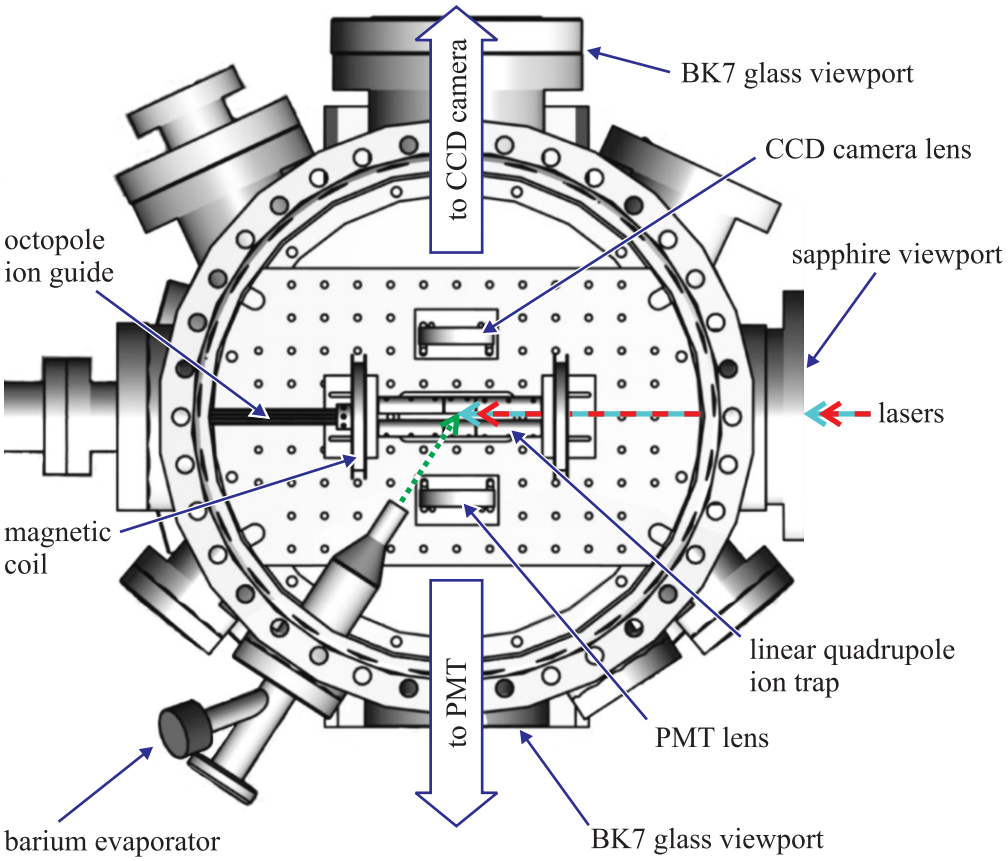

Figure 3.3: Overview of the ion trap vacuum chamber. Molecular ions from the ESI ion source are transferred to the linear quadrupole ion trap with the octopole ion guide. The barium ions are produced with a UHV suitable evaporator directed to the trap center (as indicated by the dashed green arrow). Cooling and repumping laser (red and blue arrows), as well as other required lasers are overlapped outside the vacuum chamber, enter it through an axial sapphire viewport, and propagate along the trap axis. The light emitted by the laser-cooled $^{138}Ba^{+}$ ions is collimated by radially arranged lenses to direct it through glass viewports to a CCD camera or a photomultiplier (PMT) both outside the vacuum chamber (scale drawing adapted from [22]).

barium is heated by electron bombardment leading to evaporation and as well ionization of barium atoms. Apertures form a beam of neutral and singly ionized barium atoms that is directed to the trap center (see green dashed arrow in Fig. 3.3). When the trap is switched on, thousands of barium ions can be trapped just by activating the evaporator for a few seconds.

The linear quadrupole trap consists of four cylindrical stainless steel rods with a diameter of 10 mm, which are divided into the middle electrodes of 20 mm length and the two endcap electrodes of 30 mm length, electrically isolated with internal macor ceramic parts. The smallest distance of the electrode surface to the trap axis is $r_0 = 4.36\,\mathrm{mm}$. With this geometry, the the axial electric potential of the trap is described by the value of $\kappa = 1500\,\mathrm{m}^{-2}$ (see Eq. (2.7)). The RF voltages for radial ion confinement are applied to the middle and the endcap electrodes with an RF frequency of $\Omega = 2\pi \cdot 2.5\,\mathrm{MHz}$ and a maximum amplitude of $U_{RF,max} = 500\,\mathrm{V}$. DC voltages of $-20\,\mathrm{to} + 20\,\mathrm{V}$can be individually applied to the four middle electrodes to compensate external electric fields for exact symmetrization of the quadrupole field. Concerning the DC supply the endcap electrodes on each side are connected to each other, and DC voltages of $-20\,\mathrm{to} + 20\,\mathrm{V}$ can be applied individually to the one and the other side. Together with the DC voltages on the middle electrodes a maximum difference of $U_{EC,max} = 40\,\mathrm{V}$ can be realized. Typical operation parameters are $200\,\mathrm{V} < U_{RF} < 500\,\mathrm{V}$ and $5\,\mathrm{V} < U_{EC} < 7\,\mathrm{V}$.

The magnetic field that is necessary for laser cooling of $^{138}Ba^{+}$ ions is produced by two coils centered around the trap axis and mounted beyond the endcap electrodes. The coils produce a magnetic field in the trap center which is parallel to the trap axis at a field strength of approximately 5 G.

Trapped ion ensembles can be analyzed destructively and non-destructively as described in detail in Chapter 4. The non-destructive technique requires an excitation of ion motion in radial direction in order to identify ion species via their mass-to-charge ratio dependent resonance frequencies (Eq. (2.12)). There are two possibilities for this radial excitation. The trap electronics allows one to modulate the amplitude of the RF voltage on the two upper middle electrodes in a range of about 10 to 300 kHz. This excitation is normally used to excite the motion of unwanted trapped species beyond stability to remove them from the trap. The other possibility uses an additional external electrode that is mounted above the trap and reaches in between the two upper middle electrodes by a few millimeters (Fig. 3.4). Arbitrary AC voltages can be applied to this radial excitation electrode that lead to a more gentle excitation of radial ion motion without the risk of losing the trapped ions, as the confining RF field is not affected directly.

For the destructive technique, a channel electron multiplier (CEM) is mounted below the trap serving as ion detector (Fig. 3.4). When the trap RF voltage is shut down, the ions lose trapping stability at mass-to-charge ratio dependent RF voltages (Eq. (4.1)). With an extraction electrode at a distance of 17 mm below the trap center and at a DC voltage of about $-1000\,\mathrm{V}$ referred to the trap electrodes, these instable ions can be accelerated downwards through a hole to the ion detector. Counting the detected ions simultaneously to the RF voltage shutdown leads to mass spectra of the trapped ion ensembles as described in Chapter 4.2. The overall ion capture efficiency is between 10 and 20 %, depending mainly on the applied detector electronics settings, but being constant during the experiments and almost equal for the various singly charged ion species. This was determined by comparing ion numbers detected by the counter with the numbers in the Coulomb crystals determined by MD simulations.

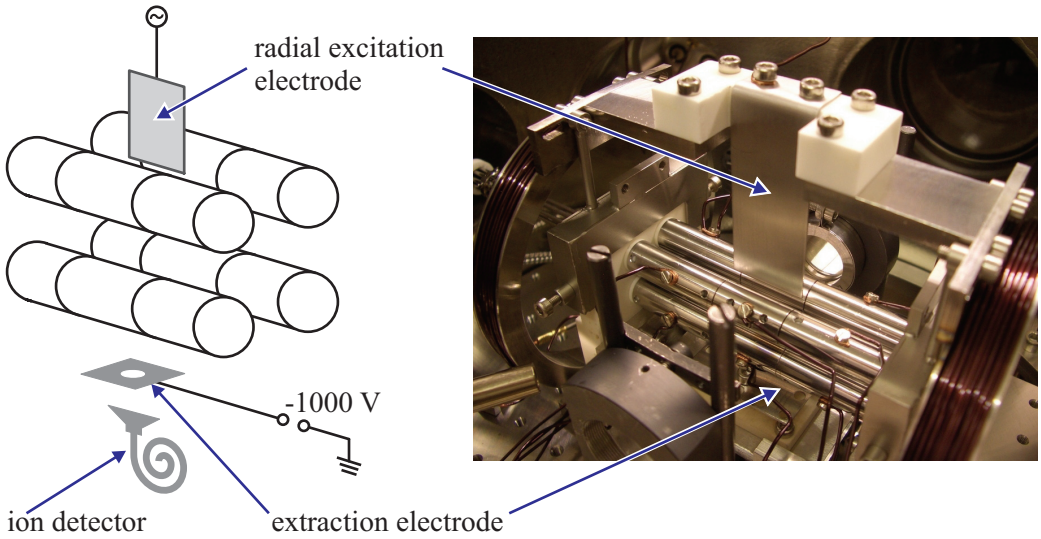

Figure 3.4: Trap setup with detection components. With an AC voltage applied to the radial excitation electrode, radial motion of the trapped ions can be excited and ion species can be identified non-destructively via their mass-to-charge ratio dependent resonance frequencies (Chapter 4.1). A destructive identification of ion species works via a controlled shutdown of the ion trap with a simultaneous detection of the escaping ions. Therefore, the ions are directed to an ion detector mounted below the trap by an extraction electrode (Chapter 4.2).

3.4 Laser system

For the Doppler laser cooling of $^{138}Ba^{+}$ ions, a cooling laser at 493 nm and a repumping laser at 650 nm are required, as described in Chapter 2.2.3. Further demands on the laser system are:

- long-term intensity and frequency stability in order to keep crystallized ion ensembles cold on the timescale of > 1 h for the observation of slow processes, such as chemical reactions [19], charge exchange reactions (Chapter 7), or slow dissociation processes (Chapter 6);
- linewidths smaller than those of the $^{138}Ba^{+}$ ions' transitions and the width of dark resonances, both in the order of < 10 MHz;
- fine and sufficiently wide tunability of the stabilized lasers in order to tune them to optimum laser cooling frequencies and to crystallize hot ion ensembles with further red-detuned lasers.

All these demands are met with the present laser system, described with its main characteristics in this chapter and in further detail in [22] and [59].

Fig. 3.5 gives a schematic overview of the laser system which consists of three lasers sources – a diode laser at 650 nm (*Sacher* TEC-100-645-10, 10 mW) that directly provides the repumping light, another diode laser at 920 nm (*Toptica* DL100, 100 mW), and a Nd:YAG laser at 1064 nm (*LZH*, 12 W) whose light is converted via sum frequency generation to obtain the cooling light at 493 nm. All lasers are frequency stabilized using the Pound-Drever-Hall technique [60] with double-stage proportional-plus-integral (PI) controllers. These controllers allow one to compensate slow frequency drifts, like those caused by temperature variations, and likewise, fast frequency fluctuations, for example due to acoustic noise. The hierarchy of the laser stabilizations is shown in Fig. 3.5.

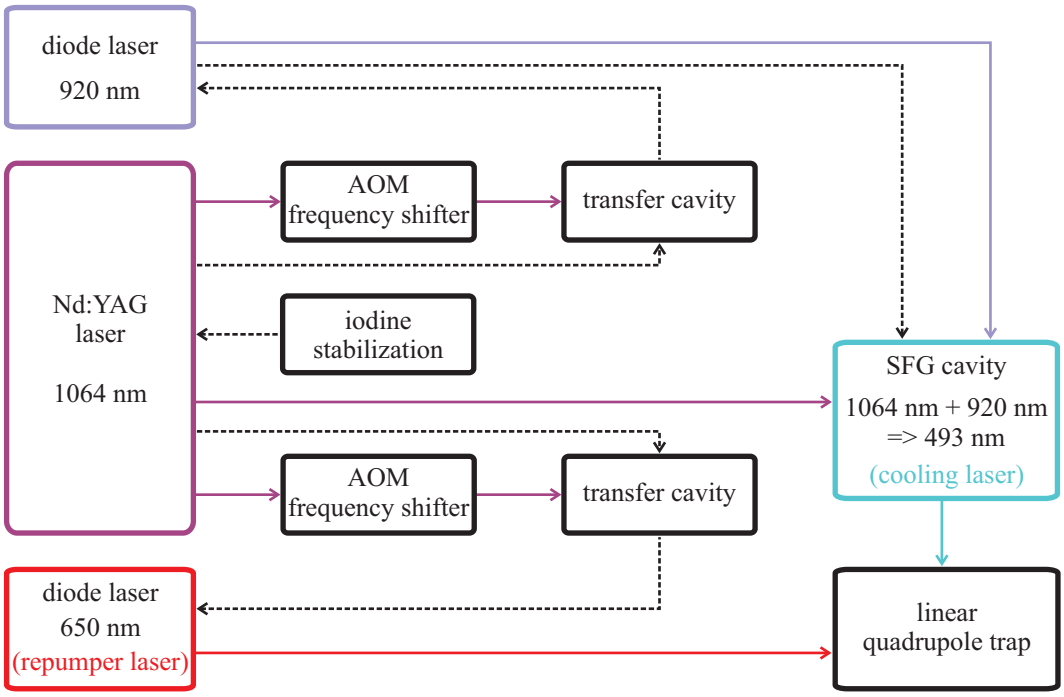

Figure 3.5: Schematic diagram of the laser system. The solid arrows schematically show the paths of the laser beams, and the dashed arrows indicate the hierarchy of the laser stabilizations. Example: The iodine stabilization determines the frequency of the Nd:YAG laser.

The Nd:YAG laser plays a decisive role for the frequency stabilization of the whole laser system. It is a master-slave system with an output power of about 12 W. Here, the master laser is a non-planar ring oscillator (NPRO) with an output power of about 800 mW at a wavelength of 1064 nm and a high short-term stability of 1 kHz/100 ms. The slave laser consists of two Nd:YAG crystals each pumped by diode lasers with 17 W at 808 nm and coupled to the master laser via injection locking. A portion of the 12 W output beam, roughly 1 W, is frequency doubled and used for stabilization of the master laser to a rovibrational transition of molecular iodine via Doppler-free saturation spectroscopy. In this way, a long-term ($>$ 1 h) frequency stability of $<$ 100 kHz for the Nd:YAG laser can be achieved.

This high frequency stability is used to frequency stabilize the two diode lasers by locking them to two so-called transfer cavities. The lengths of these two optical cavities is kept constant by stabilization to two separate beams of a few hundred milliwatt taken from the Nd:YAG laser output. Before these beams are coupled into the transfer cavities, they double pass acousto-optic modulators (AOM) that allow one to shift the frequency of these beams by up to 180 MHz. In consequence, the lengths of the transfer cavities and thus the frequencies of the diode lasers locked to them can be tuned. In practice, for the 650 nm laser a maximum tuning range of 200 MHz can be achieved, and for the 920 nm laser 150 MHz (for the sum-frequency produced 493 nm light the tuning range equals that of the 920 nm laser), sufficient for our requirements.

The largest fraction of the Nd:YAG laser light (about 8 W) is used for sum-frequency mixing it with 60 mW of the 920 nm diode laser in an optical cavity which is resonant for 920 nm to maximize the non-linear conversion efficiency. An enhancement by a factor of 15 is achieved leading to a resonating power of 900 mW at 920 nm. The 920 nm cavity mode is overlapped with the 1064 nm beam in a non-linear periodically poled KTP crystal.

Output powers of well above 50 mW at the sum-frequency wavelength of 493 nm have been achieved, which is close to optimum.

4 Analysis of trapped ion ensembles

Three different techniques are used in this work to analyze trapped ion ensembles. The first method (Chapter 4.1), denoted as *secular excitation*, is non-destructive and based on a mass-selective resonant excitation of ion motion in the harmonic trap potential. It can be applied to identify the trapped ion species and to follow changes in the number of trapped ions. The second method (Chapter 4.2), called *ion extraction*, is destructive and relies on a mass-selective extraction followed by detection of the trapped ions. It is also used for the identification of ion species and can give qualitative evidence about the temperature of the ions. The last method (Chapter 4.3) is the very versatile application tool of *molecular dynamics (MD) simulations* of the observed ion crystals, which enable to give quantitative values for ion numbers and temperatures. Furthermore the MD simulations can be used for theoretical studies and analysis of the ions' interaction and motion (Chapter 8).

4.1 Secular excitation

The radial motion of an ion, trapped in the harmonic pseudo potential of a linear quadrupole trap (Eq. (2.14)), has a resonance at a mass-to-charge ratio dependent frequency as described by Eq. (2.12)

$$\omega_r = \frac{\Omega}{2}\sqrt{\frac{q^2}{2} + a_z}.$$

Ion oscillations in the radial harmonic potential can be excited via AC amplitude modulations of the trap RF voltage or via AC voltages applied to an external excitation electrode (Chapter 3.3). When the excitation frequency coincides with the resonance frequency of an ion species, its strong large-amplitude resonant motion heats up all other trapped ions due to their mutual Coulomb interaction. This leads to a higher Doppler broadening of the cooling transition and hence a drop of the $^{138}Ba^{+}$ ions' fluorescence intensity as illustrated in Fig. 4.1(a). When recording the fluorescence intensity as a function of the applied AC excitation frequency, such a resonance case produces a fluorescence dip at the resonance frequency (Fig. 4.1(b)), which allows one to deduce the ions' mass-to-charge ratio. However, there are several aspects that strongly influence the measured resonances and which are discussed in the following.

Space charge and motional coupling

Strictly speaking, Eq. (2.12) describes the resonance frequency of a single ion, trapped in a linear quadrupole trap. When more than one ion are trapped simultaneously, space charge effects become relevant that modify the trap potential. As shown in [32] the Coulomb potential of a $^{138}Ba^{+}$ ion crystal added to the trap potential leads to an effective potential which is steeper around the $^{138}Ba^{+}$ ion crystal than that of an empty trap. Thus, sympathetically cooled ions of a, for example, higher mass-to-charge ratio arranging around the $^{138}Ba^{+}$ ion crystal will have a higher radial resonance frequency as expected from the single ion expression. Additionally, the sympathetically cooled ions themselves contribute

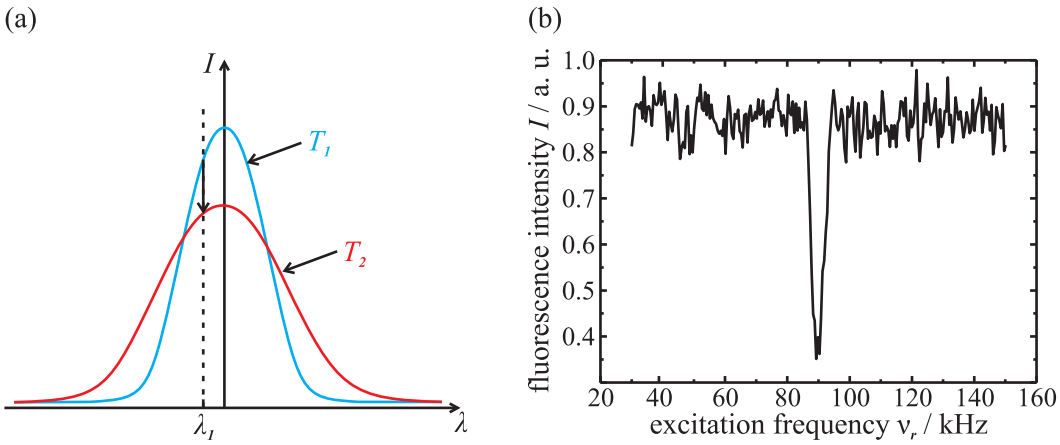

Figure 4.1: Fluorescence dips at secular excitation. (a) With the cooling laser fixed at the wavelength λ_1, the barium fluorescence intensity at 493 nm I drops when the barium ions heat up from a temperature T_1 to a temperature T_2 due to temperature Doppler broadening of the cooling transition. (b) Radial secular excitation mass spectrum of an ion crystal consisting of barium ions only. Excitation across the barium ions' resonance frequency $\nu_r = 90\,\mathrm{kHz}$ leads to a dip of the recorded barium ions' fluorescence.

to a modification of the trap potential. Consequently, the measured radial resonances can only by reproduced by MD simulations that take into account the effect of *all* trapped ions. Such deviations of measured radial resonances from calculated single ion resonances can be of up to 25 % depending on the mass-to-charge ratio compared to that of the laser-cooled ions.

According to Eq. (2.12), ions of lower mass-to-charge ratios have higher resonance frequencies. However, due to coupling of the motion of different ion species, additional resonances even at lower frequencies can occur, comparable to the dynamics of coupled pendula. This has been observed experimentally in mixed-species ion crystals (Chapter 6.2, Fig. 6.6), where ions with a mass-to-charge ratio lower than that of $^{138}Ba^+$ not only accounted for their expected resonance with a frequency above that of the barium ions, but also to a coupling resonance far below the barium resonance. Thus, coupling and space-charge effects complicate a straightforward interpretation of secular excitation spectra.

Furthermore, these coupling effects limit the mass resolution that can be achieved with secular excitation. Ba^+ and BaO^+ ions, for example, cannot be resolved because their resonances are broadened and overlap due to coupling. It is not possible with our setup to acquire a secular excitation spectrum that shows two separate fluorescence dips for these two species. The mass-to-charge ratios of simultaneously trapped ion species need to differ by more than 20 % in order to resolve them by secular excitation.

Excitation amplitude

Another important aspect of secular excitation mass spectrometry is the excitation amplitude. For a sympathetically cooled ion species, compared to the laser-cooled barium ions, a stronger amplitude needs to be applied to cause a fluorescence dip, i. e. to heat up the laser-cooled barium ions. This is due to the fact that a resonant excitation of sympathetically cooled ions affects the laser-cooled ions only indirectly via the Coulomb interaction among the different species. Here, the excitation amplitude needs to be a few times larger as shown in the example of Fig. 4.2. However, the same high amplitude applied when

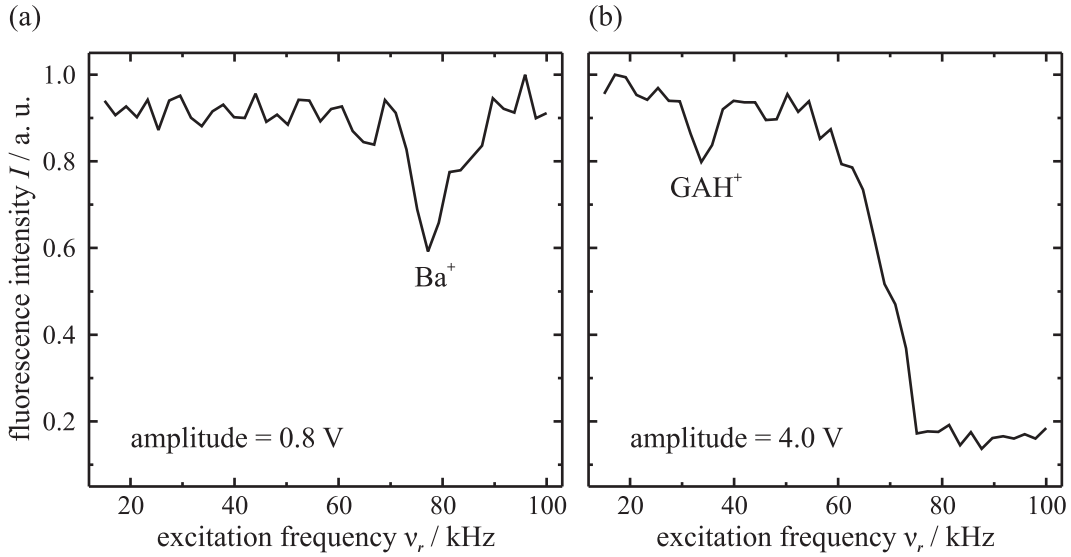

Figure 4.2: Secular excitation with different amplitudes. An ion crystal consisting of laser-cooled $^{138}Ba^+$ ions and sympathetically cooled, singly protonated glycyrrhetinic acid molecules with a mass of $m(GAH^+) = 471\,Da$ (for details see Chapter 6.1) is radially excited via the external electrode with frequency scans from 15 to 100 kHz within 0.2 s. (a) When a low amplitude of 0.8 V is applied, only the barium resonance at 78 kHz becomes apparent. (b) A higher amplitude of 4.0 V is needed to excite the sympathetically cooled species GAH^+ at 32 kHz, sufficient for detection. At this high amplitude, the resonance excitation of the barium ions is so strong that the crystal melts and the fluorescence intensity drops steplike to a lower level.

scanning across the barium ions' resonance frequency inevitably leads to such a strong excitation that the ion crystal melts and the fluorescence intensity drops steplike (Fig. 4.2(b)), usually irrecoverably

In addition, the excitation amplitude sligthly influences the value of the measured secular frequency. When the excitation frequency approaches a resonance, a fluorescence dip or step occurs earlier for higher excitation amplitudes. Depending on the secular frequency scan direction, this either happens at higher (scan from high to low) or at lower (scan from low to high) frequencies. For the two different excitation amplitudes in Fig. 4.2 this is very evident for the higher amplitude, where the barium ions' resonance manifests in a step around a frequency of 68 kHz, compared to the dip at lower excitation amplitude at 78 kHz.

Laser cooling

Not only the excitation amplitude determines the strength of the fluorescence response, i. e. the height of the fluorescence dip, or whether the result is a dip or a step. Very important are also the detunings of the cooling and the repumping laser which determine the laser cooling power. For detunings that implicate a high damping (see Chapter 2.2.3), ion crystals cool down faster after resonant excitation, which leads to more narrow fluorescence dips and which prevents a melting of the ion crystals. Thus, the signal-to-noise ratio of secular excitation fluorescence dips can be adjusted by balancing excitation amplitude and laser detunings. Once these parameters are fixed, the height of the fluorescence dip is proportional to the number of the excited ions to first order approximation. This allows

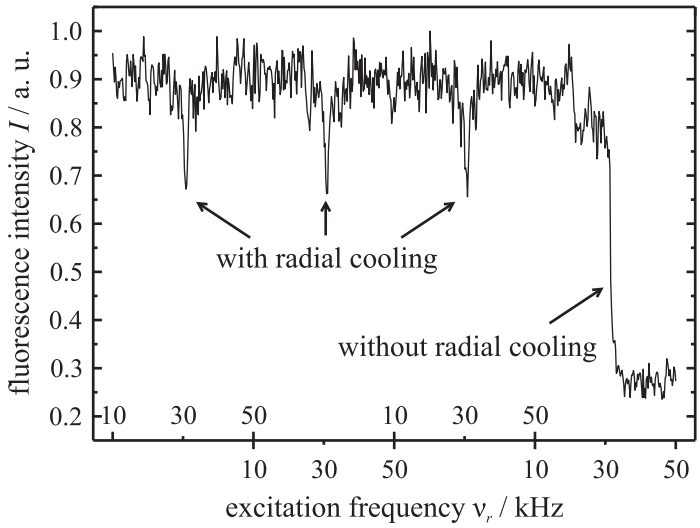

Figure 4.3: Secular excitation assisted by radial cooling. An ion crystal consisting of $^{138}Ba^+$ and GAH^+ ions is repeatedly excited with frequency scans from 10 to 50 kHz. Every time the excitation frequency coincides with the GAH^+ resonance at 31 kHz, a fluorescence dip occurs as long as an additional radial cooling beam is present that assists the cooling in radial direction. When the radial cooling beam is blocked, the damping of the ion motion is no longer sufficient in this case and the ion crystal melts due to excitation so that the fluorescence intensity drops steplike.

one to observe changes in the ion number by repeatedly scanning across an ion species' resonance which has been used in this work to measure photodestruction rates of trapped molecular ions (Chapter 6).

An interesting experimental observation in this context is the effect of an additional cooling laser beam directed to the ion crystal at an angle of 45 ° to the axial direction so that it has a significant radial component. With this additional damping in radial direction, ion crystals that would irrecoverably melt upon radial resonant excitation can possibly stay crystallized when scanning the resonance as shown in Fig. 4.3. However, as the effect is not significant in most cases and the radial exposure causes a lot of disturbing scattered light noise in this trap setup, a radial beam has not routinely been used in this work.

4.2 Ion extraction

The ion extraction method makes use of a mass-to-charge ratio selective extraction of the ions from the trap. When reducing the trap RF amplitude U_{RF}, the Matthieu stability parameter $q = (2QU_{RF})/(mr_0^2\Omega^2)$ (Eq. (2.10)) of an ion species decreases until it leaves the stability region (Fig. 4.4) and the ions escape from the trap at a mass-to-charge ratio dependent RF amplitude

$$U_{RF}^{ex} = \alpha \cdot r_0^2\Omega\sqrt{2\kappa U_{EC}\frac{m}{Q}}. \tag{4.1}$$

This expression with the numerical factor $\alpha = 1$ holds, when the edge of the stability region is approximated by $q = -a_z^2/2$, which is adequate for the range of q considered here.

As described above (Chapter 3.3), an extraction electrode below the trap center at a potential of $-1000\,\mathrm{V}$ draws the escaped ions to an ion detector that registers these ions

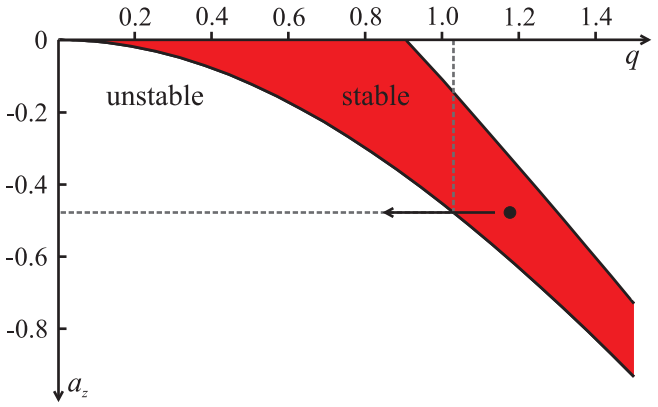

Figure 4.4: Principle of ion extraction. When reducing the trap RF amplitude U_{RF}, the q parameter of an ion species (black dot) decreases until it leaves the stability region (red shaded area) of the linear quadrupole trap at the point (a_z^{ex}, q^{ex}).

during a controlled reduction of the trap RF amplitude. The result is an ion extraction mass spectrum as shown in Fig. 4.5(a). In practice, the numerical factor α in Eq. (4.1) is different from 1 due to the attracting effect of the extraction electrode that causes the ions to escape earlier during the RF amplitude reduction, that means at higher amplitudes. Its value sligthly varies depending on ion numbers and temperatures of the trapped ion ensemble and is approximately 2.4 in this setup. Using the barium peak in an ion extraction mass spectrum for a precise calibration of α, other ion species can be identified or confirmed via their extraction amplitude U_{RF}^{ex} (Fig. 4.5(b)).

This mass spectrometry method is destructive, but it has several advantages compared to the non-destructive secular excitation method. Here, motional coupling and space charge effects do not play a role so that ion species can be unambiguously identified according to their mass-to-charge ratio reaching a resolution of $< 20\,\mathrm{Da}$ in the range below $\sim 500\,\mathrm{Da}$ for cold ion ensembles. For example, Ba^+ and BaO^+ with their mass difference of 16 Da can easily be distinguished (Fig. 4.5), which is not possible via secular excitation as mentioned above.

Furthermore, ion extraction can be applied to non-cooled ensembles as well, because it does not need the barium fluorescence as measurement signal. The mass resolution is much lower in the non-cooled case, however, sufficient in those many cases during the experiments when the ion extraction is used to check, if the loading of molecular ions to the trap has been successful or not. Another advantage is the speed of this method. An ion extraction takes a few seconds and does not need any preparation, such as tuning of lasers or adjustment of amplitudes as in the case of secular excitation.

The reason for the lower mass resolution in non-cooled cases is a temperature broadening of the ion species' peaks in the ion extraction spectra. Temperature broadening occurs, because warm ions can escape the trap already at higher RF amplitudes due to their higher kinetic energies. As a consequence, peaks of species with similar mass-to-charge ratios can overlap, and peaks in general are less distinct as in extraction spectra of cold ion ensembles. However, this supposed disadvantage allows for a qualitative determination of ion temperatures, with narrow peaks indicating successful sympathetic cooling, as will be shown in the next chapter (Fig. 5.7).

Although ion extraction is destructive, it can be applied to measure photodestruction rates of trapped molecular ions (Chapter 6). Therefore, ion crystals containing the desired molecular species are prepared under identical conditions and exposed to the destruction

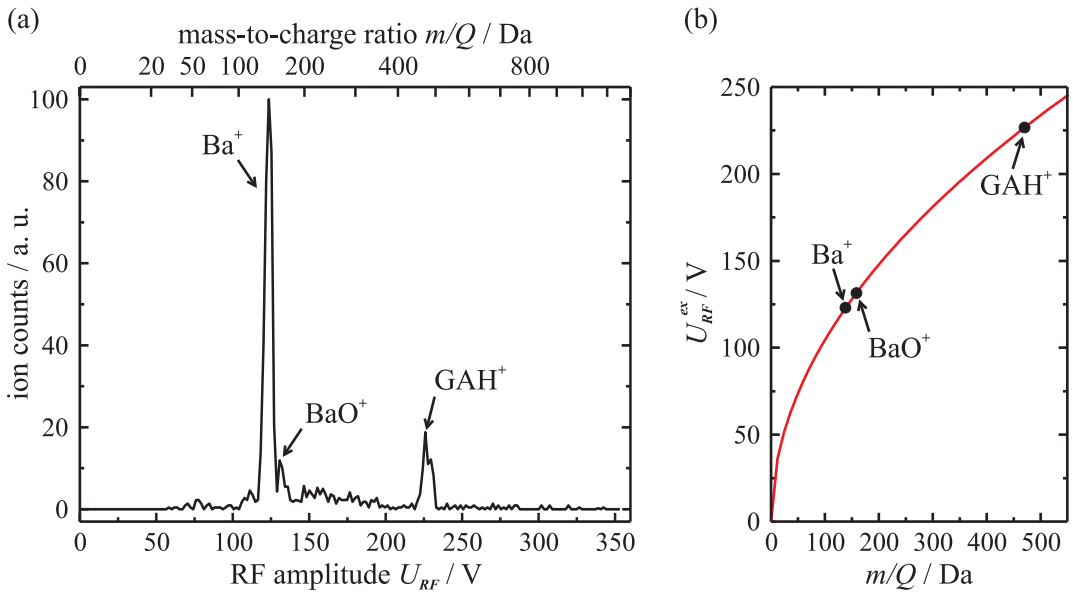

Figure 4.5: Ion extraction mass spectrum. (a) When reducing the trap RF amplitude U_{RF} to zero, ions of high mass-to-charge ratios escape first as in this three-species ion crystal consisting of Ba^+, BaO^+ and GAH^+ ions. The known mass of the Ba^+ ions can be used for calibration of the upper mass-to-charge ratio axis. (b) Calibration curve $U_{RF}^{ex}(m/Q)$ with $\alpha = 2.45$ in this case. Here, the three species are plotted at their known masses and their experimentally obtained extraction RF amplitudes. BaO^+ and GAH^+ are well confirmed by the calibration curve.

laser for different, sequentially increased times. The resulting ion crystals in different stages of the destruction process are analyzed via ion extraction, so that the decay of the parent ion number is fully described by such a series of ion extraction spectra (Fig. 6.7).

4.3 Molecular dynamics simulations

In this work, MD simulations have been used to determine ion numbers and temperatures of experimentally observed and investigated ion crystals (Chapters 5 - 7), and for theoretical studies of the Coulomb crystallization (Chapter 8). All simulations have been performed using the simulation program *SOSC* written by Chaobo Zhang and documented in detail in [32, 23].

The simulations of multi-species ion crystals are based on solving Newton's equations of motion for all laser-cooled and sympathetically cooled ions

$$m_i \ddot{\mathbf{r}}_i = \mathbf{F}_i(\mathbf{r}_1, ..., \mathbf{r}_{N_{tot}}, \mathbf{v}_1, ..., \mathbf{v}_{N_{tot}}, t) = \mathbf{F}_i^{trap} + \mathbf{F}_i^{Coulomb} + \mathbf{F}_i^{stochastic} + \mathbf{F}_i^{laser}, \quad (4.2)$$

where $i = 1, ..., N_{tot}$ numerates the ions with N_{tot} being their total number. $\mathbf{F}_i$ is the total force acting on ion i, which depends on the positions $\mathbf{r}_i$ and velocities $\mathbf{v}_i$ of all other ions, and on the time t. The total force itself is a sum of several contributions: $\mathbf{F}_i^{trap}$ is the force that confines the ion i in the trap and which is given by $\mathbf{F}_i^{trap} = -Q_i \nabla \Phi_{ps}$ with the pseudo potential of the linear quadrupole trap Φ_{ps} (Eq. (2.14)). $\mathbf{F}_i^{Coulomb}$ is the force acting on ion i that arises from the Coulomb interaction with all other ions and which is given by $\mathbf{F}_i^{Coulomb} = -Q_i \nabla \Phi_{C,i}$ with the Coulomb potential $\Phi_{C,i}$ at the position of ion i (Eq. (2.28)). The stochastic force $\mathbf{F}_i^{stochastic}$ results from random interactions of ion i with the surrounding, such as collisions with residual gas particles, electric field noise, or

scattered light. The implementation of the latter and the laser cooling force $\mathbf{F}_i^{laser}$, which acts on the laser-cooled ions only, are described later.

The equations of motion are numerically solved using the leapfrog algorithm. As the simulations are performed in the pseudo potential approximation, where the RF micromotion is not considered, the integration time steps Δt can be comparatively long which reduces the computing time significantly. Usually an integration time step of $\Delta t = 400\,\mathrm{ns}$ is used corresponding to a few hundredths of the secular oscillation periods. Typical simulated time intervals are in the order of a few milliseconds that take a few hours of computing time scaling approximately as N_{tot}^2, since the calculation of the Coulomb interaction of all particles is the most time-consuming part of the simulation. In principle, the simulation program *SOSC* allows one to consider the full RF micromotion. However, micromotion related effects, such as RF heating, have proved to be of little importance for ion crystals at temperatures below 0.5 K as considered in this work.

Implementation of cooling and heating effects

As described in Chapter 2.2.2, the light force of the cooling laser (Eq. (2.23)) causes a damping of the ion velocities opposite to the laser propagation direction and a shift of the laser-cooled ions from the trap center in the laser propagation direction. Both effects are implemented separately in the simulation program. The shift along the trap axis due to the constant light pressure force can be adjusted, according to the experimental images, by a coordinate offset of the laser-cooled ions in z-direction. The damping force is realized by reducing the z-component of the velocities of the laser-cooled ions by the damping coefficient β, which is included in the equations of motion as $F_{z,i}^{laser} = -\beta v_{z,i}$. According to [32] this leads to a temperature reduction rate

$$\frac{\mathrm{d}T}{\mathrm{d}t} = -\frac{2}{3}\frac{\beta}{m}T, \tag{4.3}$$

where m is the mass of the laser-cooled ions and T is their secular temperature as defined in Eq. (2.17). A typical experimental value for the damping coefficient is $\beta = 1.7 \cdot 10^{-22}\,\mathrm{kg/s}$. For a pure barium ion crystal at a temperature of, for example, 20 mK this yields a cooling rate of about 10 K/s. As the damping coefficient strongly depends on the laser detunings and intensities which cannot be determined accurately in the experiments, the simulations are performed with additional values for β of 1.0 and $2.0 \cdot 10^{-22}\,\mathrm{kg/s}$ in order to obtain a realistic lower and an upper limit for the achieved ion temperatures (Chapter 5.2.3).

All possible heating effects, such as collisions with residual gas particles, electric field noise, or RF heating, are implemented in the simulations by a comprehensive heating model. Here, every ion i of the species j is given a velocity kick $\mathbf{w}_{j,i}(t) = v_{j,0}\hat{\mathbf{w}_{j,i}}(t)$ at each integration time step with a fixed magnitude $v_{j,0}$ in a random direction $\hat{\mathbf{w}_{j,i}}(t)$. According to [32] this leads to a heating rate

$$h_j = \frac{\langle \Delta E_j \rangle}{\Delta t} = \frac{m_j v_{j,0}^2}{2\Delta t} \tag{4.4}$$

with $\langle \Delta E_j \rangle$ being the average change in kinetic energy per ion of the species j at each simulation time step Δt.

Note that sympathetic cooling is intrinsically implemented in the simulations because it relies on the Coulomb interaction of the trapped ions, which is fully considered here. Within this project, the sympathetic cooling efficiency has been studied via MD simulations and experimentally as described in [32].

Simulation results

As result of solving the equations of motion, the simulation program outputs the coordinates of all ions for every simulation time step. Based on these data, simulated CCD images can be generated, which are used to compare them with real CCD images taken in the experiments, in order to derive ion numbers and temperatures. The typical exposure time for experimental CCD images is 2 s. During this time the ions' trajectories span several meters due to their residual kinetic energies. As a result, the images appear blurred and have to be considered as probability density plots rather than as snapshots of current ion arrangements.

To reproduce these real CCD images by simulations, the coordinates of all ions for all simulation time steps are projected to a plane perpendicular to the desired line of sight. A density plot of this plane corresponds to a real CCD image. Not only radial views, as those taken with the CCD camera, but also axial views (watching along the trap axis) can be generated which is not possible experimentally with our setup. Furthermore, the simulations can also visualize the sympathetically cooled ions that do not fluoresce and are therefore not visible on the real CCD images (see for example Fig. 2.12(a)).

A completely realistic simulation of the CCD images would require simulated time intervals as long as the CCD exposure time and a more accurate implementation of the ions' collisions with residual gas particles, that means rare and strong collisions. However, this would lead to impracticably long computing times. With the more continuous velocity kick heating model used here, equilibrium states are reached after simulated times of a few milliseconds, and the real CCD images can be reproduced with good agreement. This works, because the CCD exposure time of 2 s is much longer than the thermalization time of the ions.

Another output of the simulation program are the translational temperatures of the involved ion species. They are given for every simulation time step as averages over all ions of that species (sub-ensemble averages). The secular temperatures defined in Eq. (2.17) are time averages of theses temperatures, usually for the whole simulated time of several milliseconds.

Simulation applications

Just like secular excitation and ion extraction, the MD simulations are used to analyze experimentally observed ion crystals, but in contrast, in a post-experimental phase. The reproduction of CCD images via simulations requires a precise adjustment of the implemented trap model to the real experimental conditions. There are basically two parameters in the experiment that are adjustable and need to be calibrated − the trap RF amplitude U_{RF} and the endcap electrode voltage U_{EC}. A calibration of these parameters with those to be set in the simulation program has been achieved by adjusting measured and simulated radial and axial resonance frequencies of barium ions in pure barium ion crystals.

The main application of MD simulations for evaluation is the determination of ion temperatures. The method is based on comparing the internal structures of real and simulated ion crystals, that are the more blurred and less distinct the higher the ion temperatures are (Chapter 2.3.2). Fig. 4.6 shows an example for the temperature determination of two comparatively small barium ions crystals. Here, the real CCD images are compared with simulated ones that have been generated with a fixed cooling but different heating rates in order to adjust the ion temperature. Ion numbers are determined in the same step by varying them in the simulations in order to reproduce length and diameter of the ion crystals as well as details of their internal structures, such as the number of shells or transitions of strings to shells.

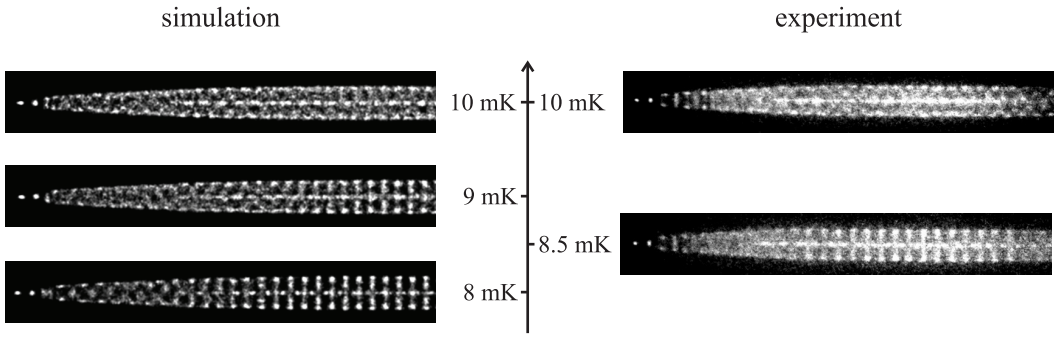

Figure 4.6: Temperature determination. CCD images of experimentally observed barium ion crystals (right) are compared with simulated CCD images of barium ion crystals at different temperatures (left). Due to the ions' higher velocities, structures are more blurred and less distinct at higher temperatures. Here, the best agreement is given for a barium ion temperature of 10 mK, or 8.5 mK respectively.

For pure barium ion crystals the temperature determination is relatively simple. Here, there are only the laser-cooled $^{138}Ba^{+}$ and the sympathetically cooled barium isotope ions which are so similar that the same heating rate can be applied to both of them. Thus, only one parameter needs to be tuned to achieve agreement of simulated and real CCD images resulting in well-defined temperatures.[1] However, other sympathetically cooled ion species feel different heating rates due to their different radial positions and their different motion. Assume an ion crystal consisting of barium ions and another ion species. Here, the temperature of the observed barium ion crystal is influenced by the sympathetic interaction with the other ion species which feels an own, but unknown heating rate. In this case, two heating rates need to be tuned independently to make the simulated barium ion crystal look like in the real CCD image, which can be achieved with numerous combinations of the two heating rates. The derived temperature for the other ion species would be ambiguous, as different heating rates lead to different temperatures. However, there is a method to determine the temperature of a sympathetically cooled ion species. It is based on a separation of the sympathetically cooled species' effect by removing it from the ion ensemble and comparing the observed ion crystals with and without this species, which is described in detail in Chapter 5.2.3 and in [21].

Another application is the simulation of resonance frequencies. As treated in Chapter 4.1, ion species can be identified to a certain extent via excitation of their motional resonances. The obtained frequencies, however, barely agree with the single ion frequencies described by Eq. (2.12). In multi-species ion crystals, coupling and space charge effects lead to significant shifts of the resonance frequencies. In the simulations that consider the interaction of all trapped ions, these effects are intrinsically taken into account. Two methods are implemented in the simulation program to simulate secular excitation. In the first one, all ions are given a small spatial offset in a radial direction, whereupon they move back and start oscillations. A Fourier analysis of their coordinates yields approximately the observable resonance frequencies. The second method gives better results as it is more similar to the experimental secular excitation. Here, an additional electric field in a radial direction

[1] This assumes, that the damping coefficient in the simulations exactly agrees with that from the experiment. As the experimental damping coefficient cannot be measured and varies depending on the detuning and the intensities of the cooling and the repumping lasers, the simulations use an average damping coefficient leading to well-defined temperatures according to this used coefficient. As described above, usually additional temperature simulations with a lower and a higher damping are performed to give realistic lower and upper limits for the temperature (see as well Chapter 5.2.3).

with a stepwise scanned frequency is added to the equations of motion. When resonances occur, the barium ion temperatures rises − just as in the experiment. The results are much closer to the experiment and effects like the dependence of the resonance frequencies on ion numbers and trap asymmetries can be studied, as described in [23]. However, these simulations are extremely time-consuming and take up to days for typical ion ensembles consisting of about 1000 ions.

In this work, MD simulations have also been used for theoretical studies of the ion motion at temperatures near and at the Coulomb crystallization (Chapter 8). It has been found that radial ion motion between the different shells of ion crystals becomes significant at temperatures $\gtrsim 7\,\mathrm{mK}$ corresponding to earlier works based on simulations or thermodynamic approaches (Chapter 2.3.1).

5 Sympathetic cooling of proteins

Molecular ions trapped together with laser-cooled atomic ions in an ion trap can sympathetically cool down to millikelvin temperatures (Chapter 2.2.1). In this work, procedures have been developed to reliably prepare such ensembles of translationally cold molecular ions with masses up to 12,400 Da. A crucial point here is the transfer of the ESI-produced gas-phase molecular ions to the linear quadrupole ion trap, which is described in the following Chapter 5.1.

For complex molecules with masses above a few hundred Daltons, multiple protonation during the electrospray process becomes more and more prevalent. This reduction of their mass-to-charge ratios is essential for these experiments because it makes such complex molecules accessible for conventional mass spectrometers and quadrupoles in the first place, and it allows for a more efficient sympathetic cooling. In one case, multiply protonated molecules of the protein cytochrome c (mass $\simeq$ 12,390 Da, charge = $+17\,e$) have been cooled to less than 0.75 K as described in Chapter 5.2 and published in *Physical Review A* [21].

5.1 Preparation of cold complex molecular ions

5.1.1 Loading of molecular ions

From the molecular ion source to the ion trap, the molecular ions are radially confined by electric RF quadrupole or octopole fields. With DC voltages on the different ion optical components along the transfer path, the molecular ions are axially guided to the ion trap. They leave the quadrupole mass filter in the ion source at a potential of $-5\,\mathrm{V}$ referred to ground and are focused by an Einzel lens at $-5\,\mathrm{V}$ into the octopole ion guide, which is at a potential of $-27\,\mathrm{V}$ for acceleration towards the ion trap. When the molecular ions reach the ion trap (Fig. 5.1), they are decelerated by the left endcap electrodes' potential of $-2.6\,\mathrm{V}$, fall into the middle electrodes' potential well of $-5\,\mathrm{V}$, and are reflected by the right endcap electrodes' potential of $+2\,\mathrm{V}$. In order to capture the molecular ions in the ion trap, helium is injected into the trap chamber serving as a buffer gas. Due to collisions with the helium atoms, the molecular ions lose kinetic energy along their way through the trap. When the buffer gas pressure is sufficiently high so that the ions lose enough energy, they cannot leave the potential well anymore after the reflection from the right endcap electrodes' potential and they are finally trapped. Indeed, the endcap electrode potentials are very crucial for the capture efficiency, which has been found to be highest for the values mentioned above.

Typical ion fluxes from the octopole ion guide into the trap center are in the range of 10,000 to several 100,000 ions per second. The number of captured molecular ions depends on several factors − among others the octopole transfer time, the buffer gas pressure, and the trap RF amplitude. The longer the octopole is switched on and ions are transferred into the trap, the more ions accumulate in the trap. Measurements with a typical test molecule GAH^+ (singly protonated glycyrrhetinic acid molecules, for details see Chapter 6.1) have shown that the number of captured ions grows linearly with the octopole transfer

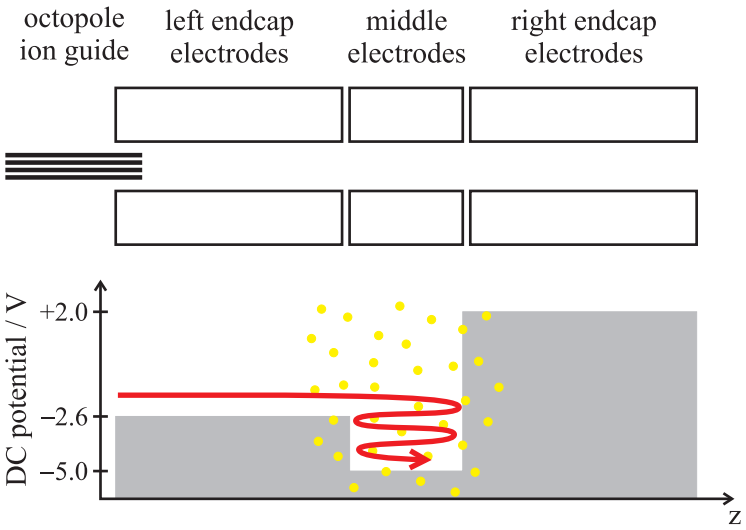

Figure 5.1: Capture of molecular ions. The lower graph schematically shows the DC potential of the linear quadrupole trap along the trap axis. Molecular ions from the octopole ion guide can be captured in the potential well when their kinetic energy (red arrow) is sufficiently reduced by collisions with helium buffer gas atoms (yellow dots).

time (Fig. 5.2(a)). For these measurements, GAH^+ ions at a flux of 35,000 ions per second have been transferred to the trap and captured, assisted by helium buffer gas at a pressure of $5 \cdot 10^{-5}$ mbar for different octopole transfer times. After every loading process, the buffer gas has been removed, and the axial DC trap potential has been symmetrized with +2 V on both the left and the right endcap electrodes, before the trapped ions were extracted and counted. Given are the numbers of *counted* ions, not the numbers of *trapped* ions as the detection efficiency was not exactly known here, but is in the range of 10 to 20 %. In the following, a detection efficiency of 10 % is assumed to give lower limits for the capture efficiency.

Usually buffer gas pressures in the range of 10^{-5} mbar are used for loading molecular ions. In this range, the capture efficiency increases linearly with the buffer gas pressure as shown in Fig. 5.2(b) and reaches a maximum value of 7.6 % in this case of loading GAH^+ at $U_{RF} = 400$ Vfor 5 s. Furthermore, the capture efficiency is determined by the trap RF amplitude. As shown in Chapter 4.2, an ion species of a certain mass-to-charge ratio can only be trapped for the trap RF amplitude being larger than the extraction RF amplitude U_{RF}^{ex} (Eq. (4.1)). For the capture of hot ions the RF amplitudes need to be even larger. Measurements with GAH^+ have shown (Fig. 5.2(c)) that the RF amplitude has to be higher than 300 V and that the capture efficiency tends to saturate for 500 V, which is the highest RF amplitude that can be produced by the trap electronics. Here, a maximum capture efficiency of 4.9 % has been achieved with a buffer gas pressure of $5 \cdot 10^{-5}$ mbar.

Additionally, the capture efficiency varies from species to species being lower for ions of higher mass-to-charge ratios. Here, the buffer gas deceleration effect is accordingly smaller and higher RF amplitudes need to be applied. However, as typical cold ion ensembles investigated in this work contain only a few hundred molecular ions, the capture efficiencies at the realized ion fluxes are by far high enough for octopole transfer times of a few seconds (see examples in Chapter 5.2 and 6).

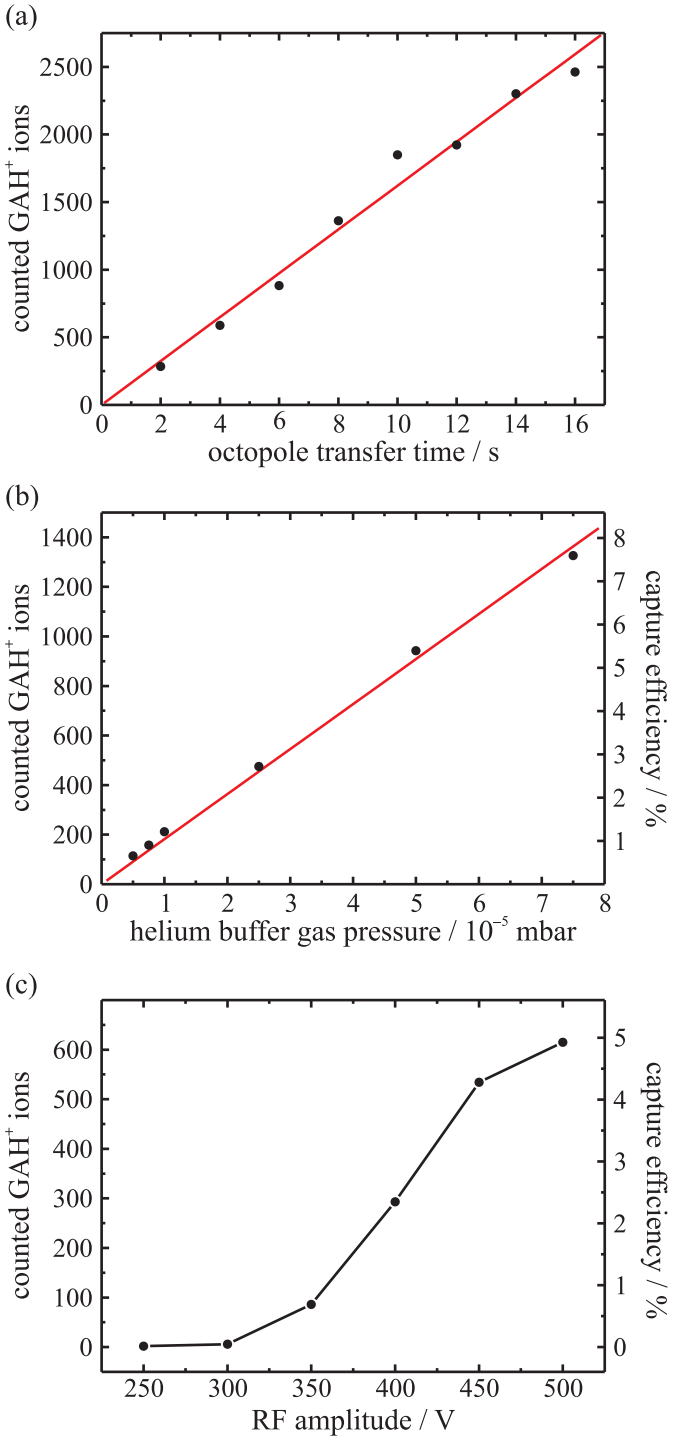

Figure 5.2: Efficiency of molecular ion capture. The loading of molecular ions to the ion trap has been analyzed for a typical test molecule GAH^+ (singly protonated glycyrrhetinic acid). (a) The number of captured ions linearly grows with the octopole transfer time. (b) The capture efficiency also linearly depends on the used helium buffer gas pressure (the red lines are linear fits). (c) A certain minimum RF amplitude is required for capturing molecular ions. The capture efficiency grows with the RF amplitude and saturates for higher values.

5.1.2 Preparation procedure

Independent of the molecular species, the preparation procedure for cold molecular ion ensembles is the same for all species − apart from specific parameters. Fig. 5.3 gives a schematic overview of the standard preparation procedure, which is described in the following.

1. Injection of helium buffer gas
   To decelerate and capture the molecular ions coming from the octopole ion guide, helium buffer gas at pressures of $1 - 10 \cdot 10^{-5}$ mbar is injected into the ion trap chamber using a piezoelectric leak valve.
2. Loading of molecular ions
   While the molecular ion source is constantly running during the experiments producing molecular ions of the desired mass-to-charge ratio, the octopole ion guide is not switched on all the time, so there is no continuous ion flux into the trap. Just for loading it is switched on for a few seconds so that the molecular ions are transferred to the trap and can be captured, decelerated by the buffer gas. For loading, the trap RF voltage is set to high values of $400 - 500$ V with the left endcap electrode potential lowered to -2.6 V to allow the ions to leak into the axial potential well as described in Chapter 5.1.1. The number of trapped molecular ions depends on the octopole transfer time, the buffer gas pressure and the RF amplitude.
3. Removal of helium buffer gas
   After the octopole has been switched off, the buffer gas injection is stopped by closing the leak valve. The pressure in the ion trap chamber returns to less than $1 \cdot 10^{-9}$ mbar within less than 30 s. Now a hot cloud of molecular ions and possibly fragments created while loading is confined in the ion trap at ultrahigh vacuum conditions. Finally, the axial trap potential is symmetrized by increasing the left endcap electrodes' potential to the same value as applied to the right endcap electrodes (usually $+2$ V).
4. Loading of barium ions
   Then barium ions from the UHV evaporator are added to the cloud of molecular ions which takes less than 10 s. The barium cooling and repumping laser, which are roughly tuned to the right wavelengths or are already locked from a previous experiment, are unblocked in this step to assist the capture of barium ions.
5. Removal of unwanted species
   The hot cloud of barium and molecular ions usually cannot crystallize because it contains various unwanted species. There are molecular fragments created during buffer gas loading or through collisions with neutral or charged barium atoms. And there are CO_2^+ ions from the barium evaporator as well as BaO^+ and $BaOH^+$created from reactions of Ba^+ ions with CO_2, O_2 or H_2O from the residual gas or already in the evaporator. All theses unwanted species are removed now by applying suitable strong secular excitation scans that cover these species' resonance frequencies (Chapter 3.3). Typically a few scans of a few seconds are performed. Alternatively, molecular fragments from loading can also be removed directly after their loading before adding the barium ions, if they are of similar mass as the barium ions in order not to remove the latter.
6. Tuning and locking lasers
   After the clean sweeps and provided that the number of molecular ions is not too high, the purified cloud of barium ions and molecular ions can cool down and crystallize. Therefore the lasers need to be tuned to optimum wavelengths in case they are not already locked from a previous experiment. In total, such a preparation procedure can be finished within less than a minute.

Molecule	Abbreviation	m / Da	Q / e	$\frac{m}{Q}$ / Da	T / mK
Tyrosine	$TyrH^+$	182	+ 1	182	ND
Alanine-tyrosine	$AlaTyrH^+$	253	+ 1	253	ND
AlexaFlour350	AFH^+	411	+ 1	411	< 140
Glycyrrhetinic acid	GAH^+	472	+ 1	472	< 80
Cytochrome c	Cyt^{17+}	$\simeq$ 12,400	+ 17	729	< 730
Cytochrome c	Cyt^{12+}	$\simeq$ 12,400	+ 12	1,033	$< 1{,}200$

Table 5.1: Overview of ESI-produced, sympathetically cooled molecular species. Given are the masses m of the trapped, protonated molecules. The charge state Q is equivalent to the grade of protonation. The last column gives the upper temperature limits that have been determined via MD simulations as described in Chapter 5.2.3 (ND: not determined).

Once the ions are crystallized and the lasers are locked, such an ensemble of molecular ions can be kept cold for many minutes and in principle for hours. The main restriction beside laser lock stability are loss reactions of the barium ions with residual gas particles. As described in detail in a paper published during this project [19], the laser-excited $^{138}Ba^+$ ions in the $6^2P_{1/2}$ state can react with CO_2, O_2 and H_2O molecules from the residual gas forming BaO^+ and $BaOH^+$ ions. The ground state barium isotope ions, however, do not have a sufficiently high activation energy, so only the number of the laser-cooled $^{138}Ba^+$is reduced due to these loss reactions. In consequence, the sympathetic cooling power of the laser-cooled $^{138}Ba^+$ subensemble decreases until the whole ion ensemble can no longer be kept cold. For vacuum pressures of $< 1 \cdot 10^{-9}$ mbar the loss reactions are less significant, and storage times for cold molecular ion ensembles of more than 20 min have been realized.

5.1.3 Cooled molecular species

In this work, the sympathetic cooling of ESI-produced molecular ions to temperatures below 1 K has been demonstrated for different types of molecules, such as dyes, pharmaceutical agents, amino acids, peptides, and even proteins, covering a mass range from 182 to 12,400 Da. Tab. 5.1 gives an overview of the molecular species that have been verifiably trapped and cooled.

As the temperature determination for sympathetically cooled ion species (Chapter 5.2.3) is a time-consuming task, it has only been performed for some of the species. The achieved temperatures for $TyrH^+$ and $AlaTyrH^+$ remain not determined, but are expected to be < 100 mK because their ion ensembles crystallized just as in the cases of the other ion species. Additionally, such temperatures would agree with the observed and expected tendency, that for ion species of lower mass-to-charge ratios generally lower temperatures can be achieved. This is due to the fact, that in a linear quadrupole trap sympathetic cooling is more efficient for ions of mass-to-charge ratios similar to that of the laser-cooled ion species because of their closer radial distance and hence, a stronger Coulomb interaction (Chapter 2.2.1).

However, the achieved temperatures also depend on many other factors, for example the cooling laser detunings, the vacuum pressure, and as well the ratio of the numbers of sympathetically cooled and laser-cooled ions. Thus, in cases of similar mass-to-charge ratios, conditions are possible where ions of a higher mass-to-charge ratio can have a lower temperature as observed in the case of GAH^+ and AFH^+ (compare Tab. 5.1).

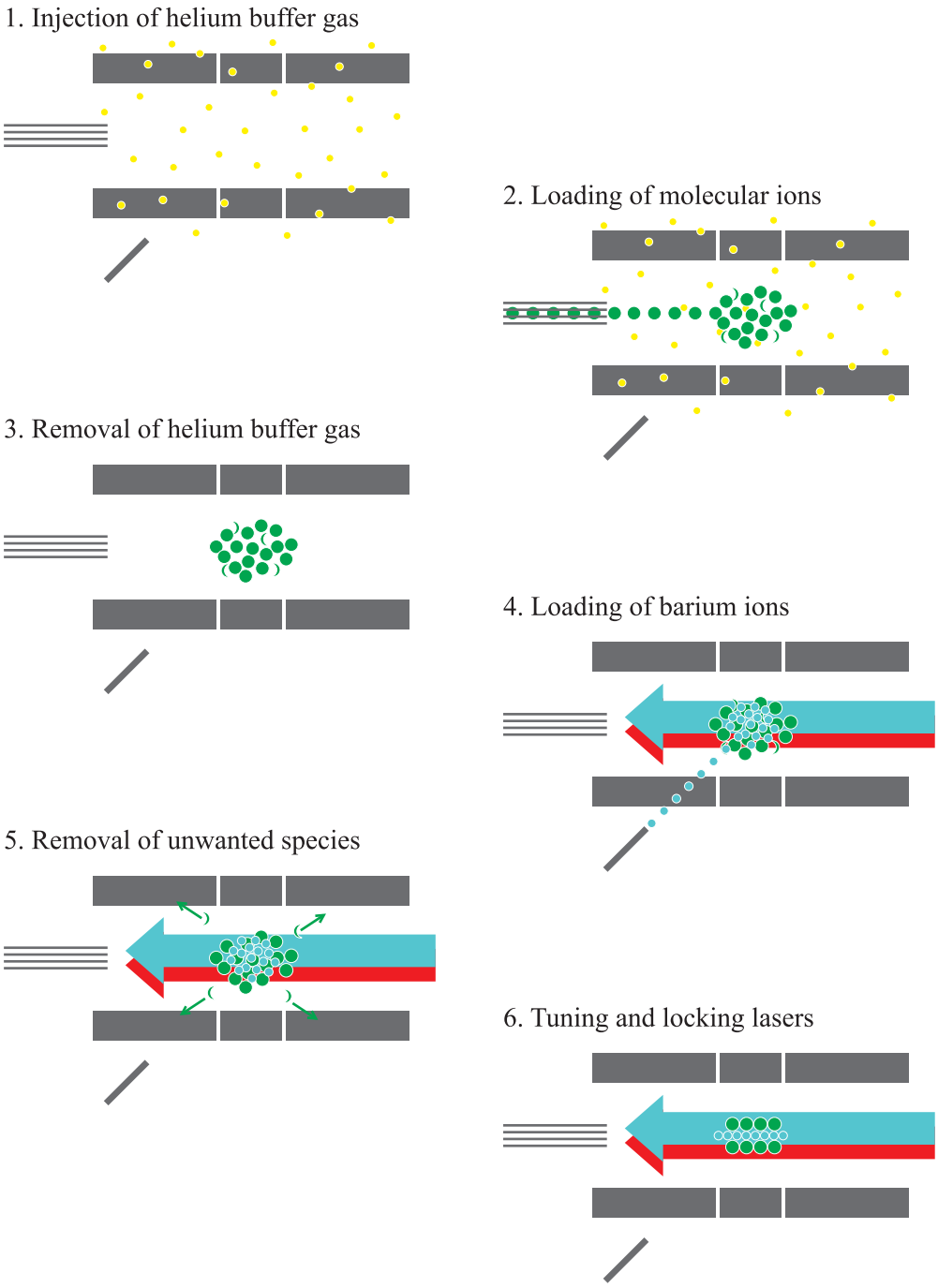

Figure 5.3: Preparation procedure for cold molecular ion ensembles. 1. Helium buffer gas (yellow circles) is injected into the ion trap vacuum chamber. 2. Molecular ions (green circles) transferred to the trap by the octopole ion guide accumulate in the trap due to deceleration by collisions with the buffer gas atoms. 3. The buffer gas is removed and a cloud of molecular ions and possible fragments (broken green circles) remains confined in the trap at UHV conditions. 4. Barium ions (blue circles) from the evaporator are added to this cloud with the cooling and repumping laser exposed to the trapped ions assisting the capture of barium ions. 5. Unwanted species are removed by the application of suitable strong secular excitation frequency scans. 6. The purified ion cloud cools down and crystallizes when the lasers are tuned to optimum wavelengths.

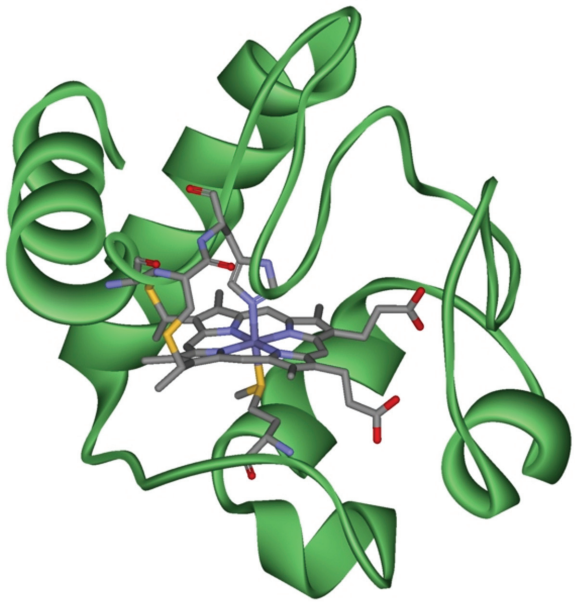

Figure 5.4: Three-dimensional structure of cytochrome c. Cytochrome c consists of about 100 amino acids that are represented as green helices and loops surrounding a central heme group.

5.2 Cooling of cytochrome c

The demonstration of sympathetic cooling of cytochrome c molecules has two special features compared to the other handled species: The molecules are much heavier (more than 26 times) and the trapped molecular ions are multiply charged (up to 17 times). The preparation procedures are similar, but parameter values up to the limits of what is experimentally feasible have to be applied.

5.2.1 Multiple protonation

Cytochrome c is a comparatively small protein which consists of about 100 amino acids and a functional heme group with a total mass of about 12,400 Da. It is found in animals, plants and unicellular organisms where it is an essential component of the electron transport chain. Unlike other proteins it is highly soluble, which makes it easily applicable for electrospray ionization. There are several ways to illustrate the three-dimensional structure of a protein. All-atom representations are often too complex and unclear. Fig. 5.4 shows the structure of cytochrome c in a commonly used simplified way, where the amino acids are represented as helices and loops surrounding the central heme group.

Amino acids contain amine groups that include a basic nitrogen atom with a lone electron pair. Due to its large number of amino acids, cytochrome c has numerous basic sites to which protons can attach in acidic solution (Chapter 3.2). The number of protons attached, depends on the pH-value of the solution and shows a distribution as shown in Fig. 5.5. The higher the acid concentration of the solution, the higher is the average grade of protonation. Fig. 5.5 compares the ESI mass spectra of solutions of cytochrome c from horse heart (*Fluka BioChemika*) at a concentration of 10 µmol/l in a 1:1 mixture of methanol and water with (a) 0.5 % and (b) with 2 % acetic acid added. In the mass spectrum of the 0.5 % solution, cytochrome c molecules with protonation grades of 7 to 15 can be identified, in the one of the 2 % solution, grades of 7 to 17. All theses different

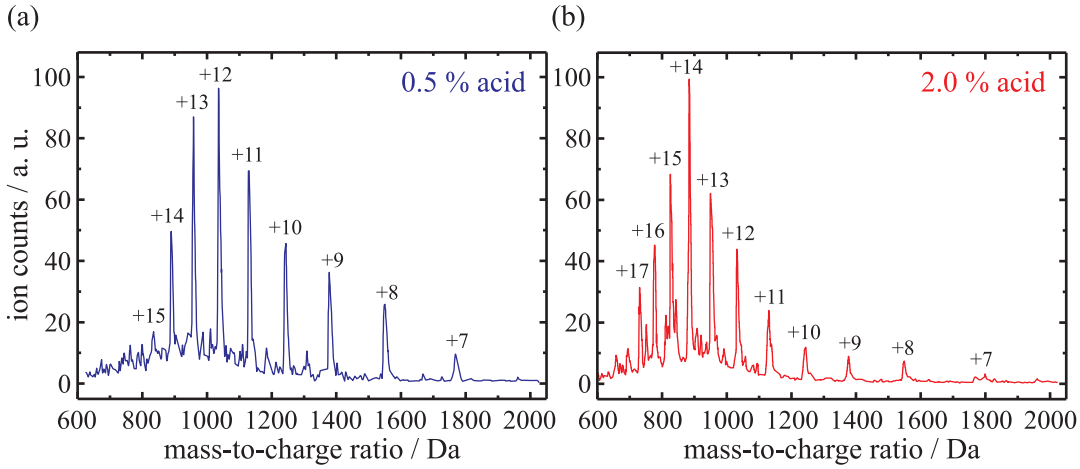

Figure 5.5: ESI mass spectra of cytochrome c. The plots show ESI mass spectra of cytochrome c solutions in 1:1 mixtures of methanol and water with different concentrations of acetic acid. Higher acid concentrations lead to an higher average grade of protonation. In the solution with 0.5 % acid (a) the most prevalent species is 12-fold protonated cytochrome with a mass-to-charge ratio of 1033 Da, and in the solution with 2.0 % acid (b) it is the 14-fold protonated molecule with 886 Da.

species can be transferred to the ion trap with ion fluxes roughly proportional to the height of the peaks in the mass spectra with a maximum flux of 40,000 ions per second. Thus, the ion fluxes are lower than for other singly protonated molecules, especially for the lower protonation grades which only yield fluxes of a few thousand ions per second reaching the trap center.

The lower the protonation grade, the higher is the mass-to-charge ratio and the more difficult it becomes to capture the molecular ions, on the one hand because of the lower ion fluxes, and on the other hand because of the lower capture efficiency for higher mass-to-charge ratios (Fig. 5.2(c)). For all species, an RF amplitude of 500 V needs to be applied, which enables to capture cytochrome molecules with protonation grades of 17 down to 10. Molecules with protonation grades lower than 10 cannot be captured efficiently because the RF amplitude cannot be increased above 500 V and the ion fluxes are too low.

As an example, 12- and 17-fold protonated cytochrome molecules, Cyt^{12+} and Cyt^{17+}, have been verifiably trapped and cooled as described in detail in the following Chapters 5.2.2 and 5.2.3. For the production of Cyt^{12+} ions the above mentioned solution with 0.5 % acetic acid has been used because here, the achievable ion flux for this species is maximum (Fig. 5.5(a)). However, for the production of Cyt^{17+} ions a solution with a higher acid concentration (2 %) had to be used, as this species does not occur in the less acidic solution.

Due to the high mass of the cytochrome molecules, comparatively high buffer gas pressures of up to $10 \cdot 10^{-5}$ mbar have to be applied to increase the capture efficiency. As a result, it takes longer to remove the buffer gas and sometimes minutes to return to pressures $< 1 \cdot 10^{-9}$ mbar. Consequently, loss reactions of the laser-cooled $^{138}Ba^+$ ions are more significant here. With the decreasing number of laser-cooled $^{138}Ba^+$ ions the available sympathetic cooling power decreases and it becomes more difficult to keep the entire ion crystal cold. This is additionally complicated by the loss reaction product BaO^+. These ions accumulate in the ion crystal and claim on their part a fraction of the sympathetic cooling power. Therefore the BaO^+ ions are removed from time to time with strong secular

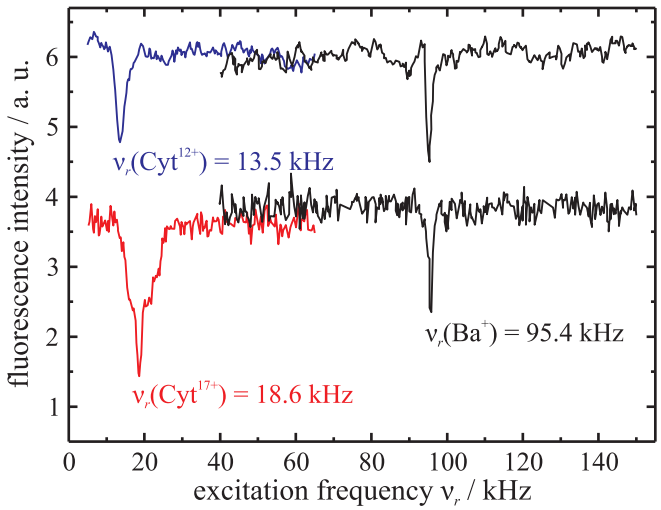

Figure 5.6: Secular excitation spectra of barium/cytochrome ion crystals. The upper curves (Ba^+/Cyt^{12+}) and the lower curves (Ba^+/Cyt^{17+}) have been acquired at the same trap parameters and therefore yield the same Ba^+ resonance frequency of 95.4 kHz. Cyt^{12+} and Cyt^{17+} can be distinguished by their different resonance frequencies which are well confirmed by their theoretical values.

excitation scans.

5.2.2 Detection of trapping and cooling

According to the preparation procedure described in Chapter 5.1.2, cold ensembles of Cyt^{12+} and Cyt^{17+} ions have been prepared and investigated in this work. Successful trapping of the desired molecular species can be proved by secular excitation mass spectrometry (Chapter 4.1). Fig. 5.6 shows secular excitation spectra of two ion crystals consisting of Ba^+ and Cyt^{12+} ions (upper curves), or Cyt^{17+} ions (lower curves) respectively. The upper and lower curves are composed of two different scans – one from 5 to 65 kHz for the detection of the cytochrome ions, and one from 40 to 150 kHz with a ten times lower excitation amplitude for the barium ions in order to avoid a destruction of the ion crystal. As all scans have been acquired at the same trap parameters (with $U_{RF} = 362\,\mathrm{V}$), the barium resonances coincide at $\nu_r(\mathrm{Ba}^+) = 95.4\,\mathrm{kHz}$ and can be used for calibration. With the single-ion resonance frequency $\nu_r \sim Q/m$ for $-a_z \ll q$ (see Eq. (2.12)) the expected frequencies for the cytochrome ions can be calculated as

$$\nu_r^{calc}(\mathrm{Cyt^{n+}}) = \nu_r(\mathrm{Ba^+})\frac{m(\mathrm{Ba^+})}{Q(\mathrm{Ba^+})}\frac{Q(\mathrm{Cyt^{n+}})}{m(\mathrm{Cyt^{n+}})}, \tag{5.1}$$

which yields $\nu_r^{calc}(\mathrm{Cyt^{12+}}) = 12.8\,\mathrm{kHz}$ and $\nu_r^{calc}(\mathrm{Cyt^{17+}}) = 18.1\,\mathrm{kHz}$. These values are well confirmed by the experimental results of $\nu_r(\mathrm{Cyt^{12+}}) = 13.5\,\mathrm{kHz}$ and $\nu_r(\mathrm{Cyt^{17+}}) = 18.6\,\mathrm{kHz}$. The small differences of less than 5 % can be ascribed to space charge and motional coupling effects.

Another method to identify trapped ion species and to gain qualitative information about their temperature is ion extraction mass spectrometry (Chapter 4.2). Fig. 5.7 shows the ion extraction spectra of a cooled (blue) and a non-cooled (black) ensemble consisting of Ba^+ and Cyt^{17+} ions. In the non-cooled case, the barium cooling lasers were blocked and the peaks for both species in the extraction spectrum appear temperature broadened. In the cooled case, not only the peak of the laser-cooled Ba^+ ions is narrower, but also the

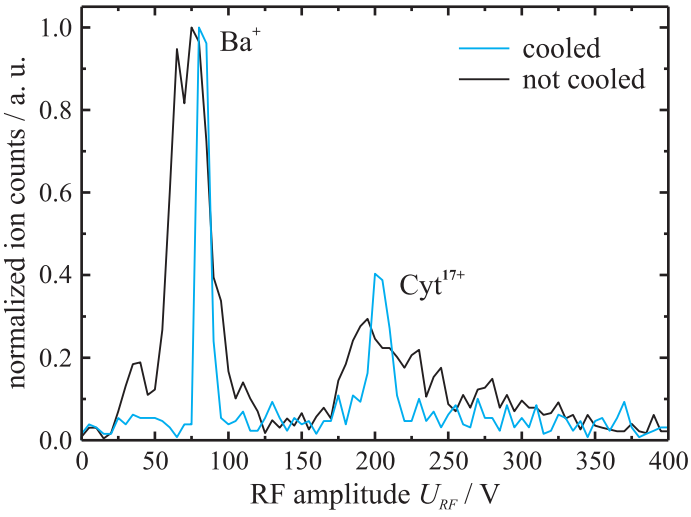

Figure 5.7: Ion extraction spectra of cooled and not cooled Ba^+/Cyt^{17+} ion ensembles. In the non-cooled case (black), the peaks of both species are temperature broadened. In the cooled case (blue), not only the peak of the laser-cooled Ba^+ ions is narrower, but also the one of the Cyt^{17+} ion which is a qualitative proof of their sympathetic cooling.

one of the Cyt^{17+} ions, which is a qualitative proof of their sympathetic cooling. A method for the quantitative determination of temperatures of sympathetically cooled ion species is described in the next section.

From the RF amplitude U_{RF} at which an ion species leaves the trap during an ion extraction, one can derive its mass-to-charge ratio via Eq. (4.1). Using the Ba^+ peak at $U_{RF} = 82.5\,\mathrm{V}$ in Fig. 5.7 (cooled case) for calibration, a mass-to-charge ratio of 828 Da for the Cyt^{17+} peak at $U_{RF} = 202.5\,\mathrm{V}$ can be calculated. Compared to the real mass-to-charge ratio of Cyt^{17+} of 729 Da (Tab. 5.1) the derived value is about 14 % too high. This needs to be ascribed to the lower mass resolution of the ion extraction method for warmer ion crystals as discussed in Chapter 4.2. Indeed, the peaks in this ion extraction spectrum are wider and hence temperatures are higher than in the case shown in Fig. 4.5, where the mass determination was more precise.

5.2.3 Temperature determination

In contrast to the laser-cooled $^{138}Ba^+$ ions, sympathetically cooled ions are not visible in the CCD images, so a direct temperature determination via comparison of real and simulated CCD images is not possible. However, indirectly their temperature can be determined by their effect on the laser-cooled ions. Therefore, two CCD images of the barium ion crystal are considered − one with the sympathetically cooled ions present (denoted as image 1), and one with the sympathetically cooled ions removed (denoted as image 2). The latter barium ion crystal looks colder than the one with the sympathetically cooled ions because it is not heated by the sympathetically cooled ions. This temperature difference together with the different shape of the ion crystals due to their Coulomb interaction in the trap are the input for the temperature determination of sympathetically cooled ions.

In the following, the procedure of temperature determination using MD simulations is described step by step using the example of a Ba^+/Cyt^{17+} ion crystal (Fig. 5.8):

1. Determination of the barium ion number
   In order to simulate CCD images, the numbers of the trapped ions need to be known

as input for the simulations. They can be determined by reproducing the observed ion crystals in length, diameter, shape and inner structure as described in Chapter 4.3. The first step in temperature determination is to find the numbers of laser-cooled $^{138}Ba^+$ and barium isotope ions in image 2. As their mass-to-charge ratios are very similar and therefore the ions do not radially separate, one first reproduces the crystal disregarding the dark isotopes to obtain the total number of barium ions $N_2(Ba^+)$. Then, the numbers of isotopes $N_2(^{136}Ba^+)$ and laser-cooled barium ions $N_2(^{138}Ba^+)$ can be found by adapting these numbers to obtain agreement with image 2 concerning the length of the visible $^{138}Ba^+$ structure, keeping $N_2(Ba^+) = N_2(^{136}Ba^+) + N_2(^{138}Ba^+)$. To simplify the simulations, the six present barium isotopes (see Tab. 2.1) are treated as one species with a mass of 136.0 Da, weighted according to their abundance.
In the example of Fig. 5.8(d), simulations of image 2 yield a total barium ion number of $N_2(Ba^+) = 350$, with $N_2(^{138}Ba^+) = 140$ and $N_2(^{136}Ba^+) = 210$. Note here that the fraction of $^{138}Ba^+$ with 40.0 % is significantly different to that in natural barium of 71.7 %. This is due to the loss reactions of laser-excited $^{138}Ba^+$ ions during the preparation of the Ba^+/Cyt^{17+} ion crystal (Chapter 5.1.2).

2. Determination of the barium ion heating rate
Image 1 and 2 have been taken at the same experimental parameters and conditions, so the damping coefficient β and the heating effects are the same. Thus, the heating rate that reproduces the blurring of the $^{138}Ba^+$ ion crystal in image 2 can also be taken for the simulation of image 1. In consequence, only the heating rate for the molecular ions needs to be adjusted to reproduce image 1 and to obtain the molecular ions' temperature.
In order to find the barium ions' heating rate, first an average damping coefficient of $\beta = 1.74 \cdot 10^{-22}$ kg/s calculated from 8-level Bloch equations using measured laser saturation parameters and detunings [61] is applied. Later, a lower and a higher value of β are used to find lower and upper limits for the heating rate, as described in point 5.
In the example, a simulation with a heating rate for the barium ions of $h(Ba^+) = 3.72\,\mathrm{K/s}$ reproduces the real CCD image 2 (compare Fig. 5.8(d) and (e)) and leads to temperatures $T_2(^{138}Ba^+) = 19\,\mathrm{mK}$ and $T_2(^{136}Ba^+) = 22\,\mathrm{mK}$. Here, the same heating rate is applied for the laser-cooled $^{138}Ba^+$ ions and the sympathetically cooled barium isotope ions, which is a legitimate approximation in view of the two species' similarity.

3. Determination of the molecular ion number
As described above, image 2 is taken after the molecular ions have been removed from the ion ensemble. The removal works via a partial ion extraction in which the trap RF amplitude is not lowered to zero, but only to a value between the extraction RF amplitude of the barium and the molecular ions. When image 2 has been taken, all residual ions are extracted and counted with a full ion extraction. Assuming the same detection efficiency for the barium and the molecular ions, one can conclude the number of molecular ions from the ratio of the counted ions and the simulated number of barium ions. However, this does not work for highly charged molecular ions as the detection efficiency is not the same as for the singly charged barium ions. Here the number of molecular ions is determined with regard to their effect on the shape of the observed $^{138}Ba^+$ ion crystal. As described in Chapter 2.3.2, ions of a higher mass-to-charge ratio arrange around the barium ions, and radially squeeze as well as axially prolong the $^{138}Ba^+$ ion crystal. Thus, the number of trapped molecular ions can be found by variations of ion numbers until the best agreement of the real and simulated CCD image 1 is achieved.
In the example in Fig. 5.8(b) and (c), the simulations yield a number for the Cyt^{17+}

ions of $N_1(\mathrm{Cyt}^{17+}) = 53$. However, the number of barium ions in image 1 is different to that in image 2. For image 1, the simulations yield $N_1(^{138}\mathrm{Ba}^+) = 158$ and $N_1(^{136}\mathrm{Ba}^+) = 230$ with $N_1(\mathrm{Ba}^+) = 388$. The total number of barium ions is higher in image 1 than in image 2 due to unintended losses of barium ions during the partial extraction of the molecular ions.

4. Determination of the molecular ion heating rate
   With all ion numbers and the heating rate of the barium ions known and set in the simulation program, in this step the heating rate for the molecular ions is adjusted so as to reproduce image 1 (compare Fig. 5.8(b) and (c)) . From the simulated ion ensemble in thermal equilibrium, the secular temperatures of the trapped ion species can be derived according to Eq. (2.17).
   In the example, with the average damping coefficient a heating rate for the Cyt^{17+} ions of $h(\mathrm{Cyt}^{17+}) = 71.6\,\mathrm{K/s}$ is found, which leads to the temperatures $T_1(^{138}\mathrm{Ba}^+) = 66\,\mathrm{mK}$, $T_1(^{136}\mathrm{Ba}^+) = 109\,\mathrm{mK}$, and $T_1(\mathrm{Cyt}^{17+}) = 704\,\mathrm{mK}$.

5. Determination of upper and lower temperature limits
   The used average damping coefficient is only a probable value and does not necessarily describe the actual laser cooling efficiency, which varies depending on numerous factors. Therefore, a lower and an upper value of β are used to determine lower and upper heating rates for the ions, and hence lower and upper limits for the achieved ion temperatures. The procedure for this purpose is as follows:

   a) With a lower (upper) value of $\beta = 1.0(2.0) \cdot 10^{-22}\,\mathrm{kg/s}$, the barium ion crystal without the molecular ions from image 2 is simulated and a lower (upper) heating rate is searched, which yields the same temperature for the barium ions $T_2(^{138}\mathrm{Ba}^+)$ and $T_2(^{136}\mathrm{Ba}^+)$ as determined for the average value of β.
      In the example, the simulations yield a lower (upper) barium heating rate of $h(\mathrm{Ba}^+) = 2.13(4.28)\,\mathrm{K/s}$.

   b) With this lower (upper) heating rate for the barium ions, the barium ion crystal with the molecular ions from image 1 is simulated and a lower (upper) heating rate for the molecular ions is searched, for which the same temperature for the barium ions $T_1(^{138}\mathrm{Ba}^+)$ and $T_1(^{136}\mathrm{Ba}^+)$ is achieved as determined for the average value of β. As a result, a lower (upper) limit for the molecular ions' temperature is found.
      In the example, the simulations yield a lower (upper) heating rate for the Cyt^{17+} ions of $h(\mathrm{Cyt}^{17+}) = 42.4(83.5)\,\mathrm{K/s}$, which leads to a lower (upper) temperature limit of $T_1(\mathrm{Cyt}^{17+}) = 680(730)\,\mathrm{mK}$.

This procedure of temperature determination is extremely time-consuming due to the fact that the simulation program typically needs a few hours until the ions have thermalized and equilibrium states are reached with new parameters. The computing times scale approximately as the square of the total ion number N_{tot}^2 (Chapter 4.3), so thermalization times of a few days are also possible for large ion ensembles. However, for the determination of ion numbers the ion temperature is not relevant, so that real and simulated CCD images with different ion numbers can be compared within seconds.

Ensembles of cold cytochrome ions of different charge states have been routinely produced within this project. But due to the high evaluation efforts, achieved temperatures have only been determined exemplarily for the above case of a $\mathrm{Ba}^+/\mathrm{Cyt}^{17+}$ ensemble and a $\mathrm{Ba}^+/\mathrm{Cyt}^{12+}$ ensemble shown in Fig. 5.9. In this example, the Cyt^{12+} ions reached a temperature of $T(\mathrm{Cyt}^{12+}) = 1.2^{+0.05}_{-0.28}\,\mathrm{K}$ which is significantly higher than the temperature which was reached for the Cyt^{17+} ions of $T(\mathrm{Cyt}^{17+}) = 704^{+26}_{-24}\,\mathrm{mK}$. This can be due to less advantageous cooling conditions, but is mainly caused by the higher mass-to-charge ratio

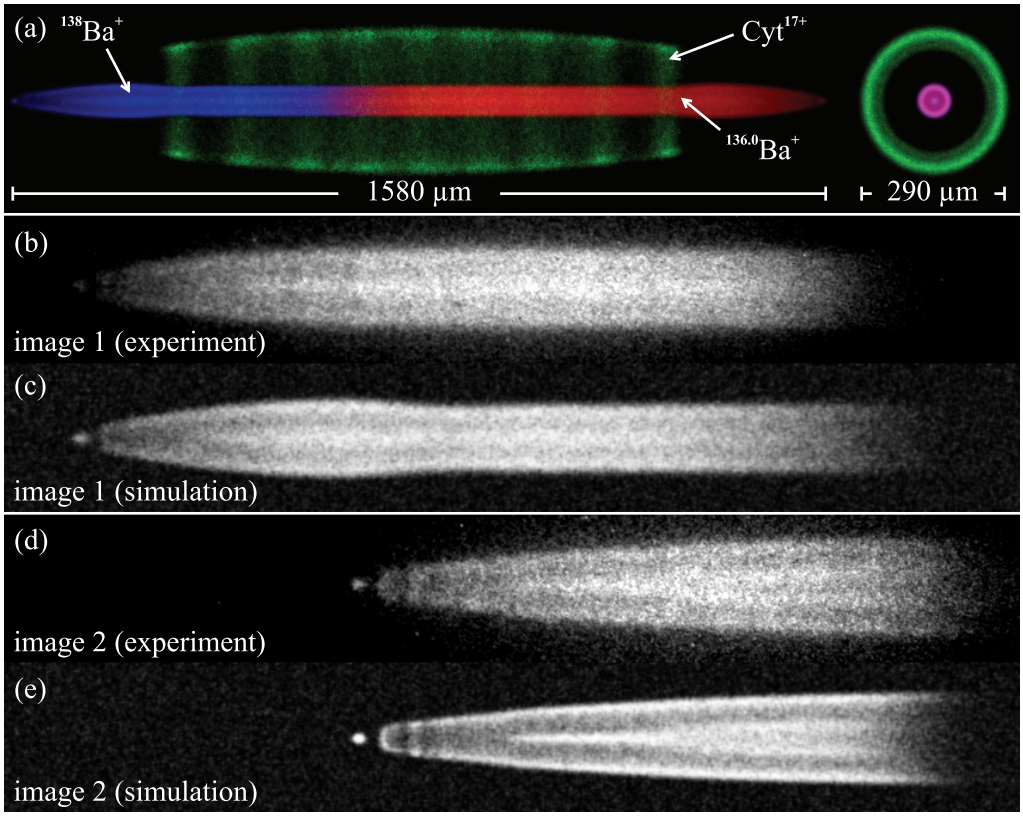

Figure 5.8: Temperature determination of sympathetically cooled Cyt^{17+} ions. (a) Simulated image of an ion crystal consisting of 158 laser-cooled $^{138}Ba^+$ ions (blue), 230 sympathetically cooled $^{136.0}Ba^+$ isotope ions (red) and 53 sympathetically cooled Cyt^{17+} ions (green). The image shows the crystal as it would appear, if all ions fluoresce, in radial (left) and axial (right) view. (b) Experimental CCD image of this ion crystal (denoted as image 1 in the text) showing the $^{138}Ba^+$ ions surrounded by the not visible Cyt^{17+} ions at temperatures of $T_1(^{138}Ba^+) = 66\,\mathrm{mK}$, $T_1(^{136}Ba^+) = 109^{+6}_{-17}\,\mathrm{mK}$, and $T_1(Cyt^{17+}) = 704^{+26}_{-24}\,\mathrm{mK}$. (c) Simulated image 1 showing the fluorescing $^{138}Ba^+$ ions only. (d) Experimental CCD image of the ion crystal after removal of the Cyt^{17+} ions (denoted as image 2 in the text) showing the $^{138}Ba^+$ ion crystal radially expanded and no longer axially prolonged nor heated by the Cyt^{17+} ions at temperatures of $T_2(^{138}Ba^+) = 19\,\mathrm{mK}$ (140 ions) and $T_2(^{136}Ba^+) = 22\,\mathrm{mK}$ (210 ions). (e) Simulated image 2 showing the fluorescing $^{138}Ba^+$ ions only.

of the Cyt^{12+} ions that leads to a larger radial distance from the laser-cooled barium ions and hence a less efficient sympathetic cooling in this case. In the case of the Ba^{+}/Cyt^{17+} crystal, the radial gap between the cytochrome and the barium ions is 64 µm and in the case of the Ba^{+}/Cyt^{12+} it is 87 µm.

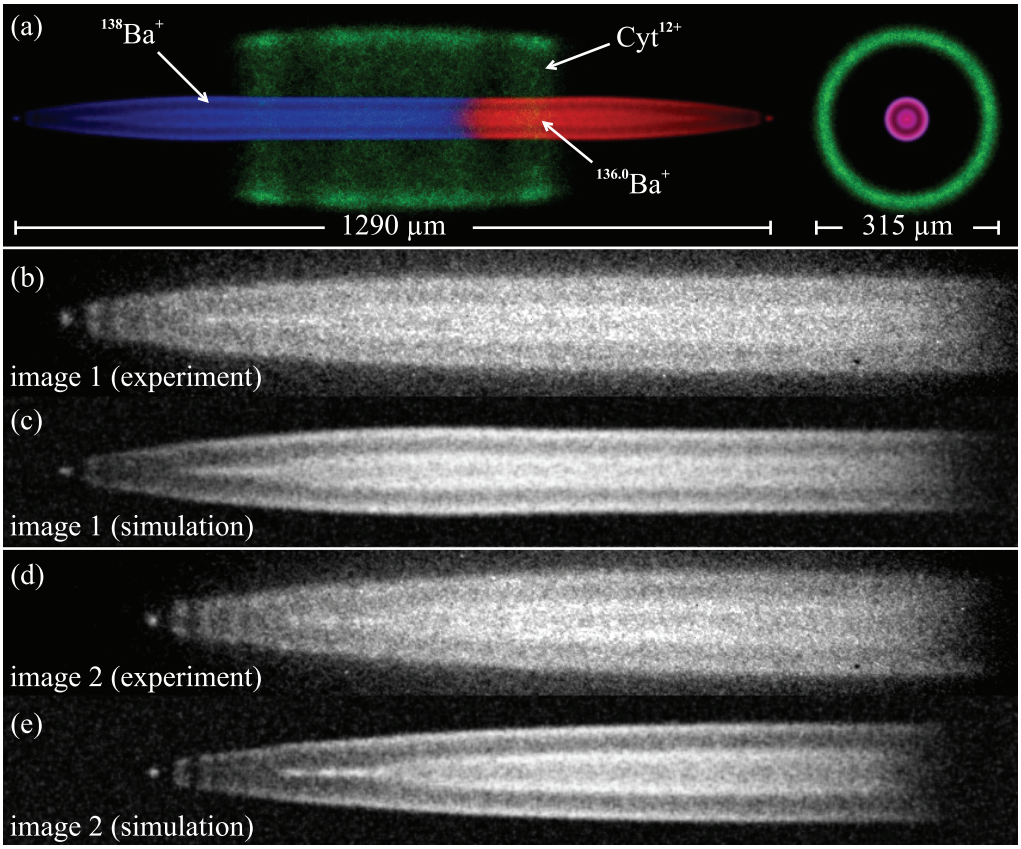

Figure 5.9: Temperature determination of sympathetically cooled Cyt^{12+} ions. (a) Simulated image of an ion crystal consisting of 170 laser-cooled $^{138}Ba^+$ ions (blue), 280 sympathetically cooled $^{136.0}Ba^+$ isotope ions (red) and 28 sympathetically cooled Cyt^{12+} ions (green). The image shows the crystal as it would appear, if all ions fluoresce, in radial (left) and axial (right) view. (b) Experimental CCD image of this ion crystal showing the $^{138}Ba^+$ ions surrounded by the not visible Cyt^{12+} ions at temperatures of $T_1(^{138}Ba^+) = 26\,\mathrm{mK}$, $T_1(^{136}Ba^+) = 35^{+2}_{-5}\,\mathrm{mK}$, and $T_1(Cyt^{12+}) = 1.2^{+0.05}_{-0.28}\,\mathrm{K}$. (c) Simulated image (b) showing the fluorescing $^{138}Ba^+$ ions only. (d) Experimental CCD image of the ion crystal after removal of the Cyt^{12+} ions, showing the $^{138}Ba^+$ ion crystal radially expanded and no longer axially prolonged nor heated by the Cyt^{12+} ions at temperatures of $T_2(^{138}Ba^+) = 16\,\mathrm{mK}$ (280 ions) and $T_2(^{136}Ba^+) = 19\,\mathrm{mK}$ (170 ions). (e) Simulated image (d) showing the fluorescing $^{138}Ba^+$ ions only.

6 Measurement of photodestruction rates

One of the main goals of this work was to develop the experimental techniques required for high-resolution vibrational spectroscopy of cold, trapped complex molecular ions. As described in Chapter 1.1, such molecules have complex and over-crowded spectra so that cooling is essential in order to resolve spectral features. Here, our setup provides advantageous conditions. However, a problem of spectroscopy on such small molecular samples in the gas-phase is that there is no or very low fluorescence emitted upon excitation. So there is no easily accessible signal for spectroscopy. A solution is destructive spectroscopy where photodestruction rates of the parent molecular ions are measured [9].

This chapter describes two methods for measuring such destruction rates of cold, trapped complex molecular ions developed within this work, using the example of singly protonated glycyrrhetinic acid molecules (GAH^+) dissociated by a UV laser at 266 nm. In the *secular excitation method,* the decay of the parent molecular ions is detected during one photodestruction process via repeated secular excitation of the parent ions' resonance, which produces signals proportional to the number of remaining parent ions (Chapter 6.2). In the *ion extraction method,* the composition of a set of initially similar Ba^+/GAH^+ ion crystals is analyzed via extractions of the ions from the trap after different times of exposition to the UV laser (Chapter 6.3).

Measurements of the photodestruction rate were performed at different intensities of the UV laser, and rates of less than $0.05\,s^{-1}$ have been determined, which is only possible due to the long ion storage times that can be achieved with this apparatus. For the UV laser wavelength of 266 nm a destruction cross section of $(1.1 \pm 0.1) \cdot 10^{-17}\,cm^2$ for GAH^+ has been determined. These results are described in Chapter 6.4 and have been published in *Journal of Physics B: Atomic, Molecular and Optical Physics* [62].

6.1 Test molecule: Glycyrrhetinic acid

Glycyrrhetinic acid is a pharmacologically active substance with the empirical formula $C_{30}H_{46}O_4$, a molecular weight of 471 Da, and a chemical structure as shown in Fig. 6.1. It is used in this work as a test molecule for calibration and tuning procedures, and for exemplary investigations. It has been chosen because it is chemically stable and inexpensive, and it can be produced at high electrospray ion fluxes.

Ensembles of cold singly protonated glycyrrhetinic acid molecules (GAH^+) are routinely prepared within less than 1 min, according to the preparation procedure described in Chapter 5.1.2. Here, with solutions of glycyrrhetinic acid (*Sigma-Aldrich*) at a concentration of 10 µmol/l in a 1:1 mixture of acetonitrile and water with $5 \cdot 10^{-3}$ % formic acid added for protonation, ion fluxes of several hundred thousand GAH^+ ions per second leaving the octopole ion guide are obtained. The achieved GAH^+ temperatures are usually $< 150\,mK$. Fig. 6.2 shows an example of a Ba^+/GAH^+ ion crystal with BaO^+ impurities that has been fully simulated regarding ion numbers and temperatures according to the temperature determination procedure as described in Chapter 5.2.3. In this case, the 1250 GAH^+ ions had a translational temperature of $134^{+8}_{-24}\,mK$, the 240 $^{138}Ba^+$ ions were at 74 mK,

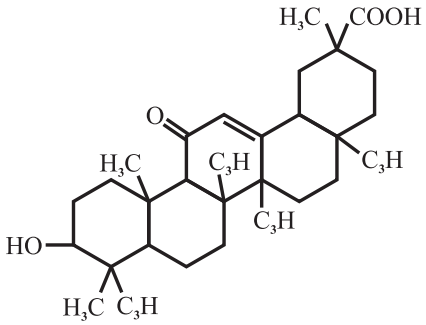

Figure 6.1: Chemical structure of glycyrrhetinic acid (GA).

the 165 $^{136.0}Ba^+$ ions at 122^{+5}_{-20} mK, and the 150 BaO^+ ions at 119^{+5}_{-19} mK. Note that for the $^{138}Ba^+$, the $^{136.0}Ba^+$, and the BaO^+ ions the same heating rates have been used as a reasonable approximation. Note further, that the $^{138}Ba^+$ loss reaction product can be either BaO^+ from the reaction with O_2 or CO_2, or $BaOH^+$ from the reaction with H_2O. As their mass-to-charge ratios differ by 1 Da only, they cannot be distinguished here and are treated as one species BaO^+.

When trapped GAH^+ ions are exposed to UV laser light of a wavelength of 266 nm, they dissociate and various fragments with mass-to-charge ratios between 40 and 82 Da are created as determined via ion extraction mass spectrometry (see Fig. 6.7). These fragments are trapped for the most part and accumulate along the trap axis forming a dark core in the $^{138}Ba^+$ ion crystal. A sequence of experimental CCD images in Fig. 6.3 shows, how an ensemble of Ba^+ and GAH^+ ions changes during exposure to very low intensity UV light. With the growing number of fragments, the dark core (orange dashed line) expands until it extends through the whole $^{138}Ba^+$ ion crystal. A dissociation of GAH^+ by the barium cooling and repumping lasers alone has not been observed.

With our apparatus we cannot give insight into the precise nature of the dissociation process of GAH^+ or of other molecular species. The mass resolution is too low to distinguish all generated fragment ion species. In addition, the further dissociation of the fragments due to the comparatively long UV exposure times complicates the interpretation. Various pathways for the unimolecular dissociation of GAH^+ are possible, like loss of neutral or charged groups, or cleavage of the molecules at weak bonds [63]. Generally, gas-phase biomolecules of sizes comparable to that of GAH^+ can dissociate after the absorption of one single UV photon of 266 nm [64, 65, 66], which is well confirmed by the linear intensity dependence of the measured destruction rates of GAH^+ (Fig. 6.10). After absorption of the UV photon, such molecules either dissociate within less than microseconds from an electronically excited state (*non-statistical dissociation*) or on a timescale of milliseconds after redistribution of the internal energy to vibrational modes (*statistical dissociation*). Especially for protonated molecules of sizes comparable to that of GAH^+, the immediate non-statistical dissociation is the dominant process [66].

Based on this assumption the destruction process can be described by a simple rate equation model as motivated in [67], given by

$$\frac{dN_e(t)}{dt} = N_g(t) \cdot R - N_e(t) \cdot (R + \Gamma + k) \tag{6.1}$$

$$\frac{dN_g(t)}{dt} = -N_g(t) \cdot R + N_e(t) \cdot (R + \Gamma)\,. \tag{6.2}$$

Here, GAH^+ ions in the electronic ground state with an ion number $N_g(t)$ absorb laser photons with the absorption rate $R = \sigma_{abs} I/h\nu$, where σ_{abs} is the absorption cross section

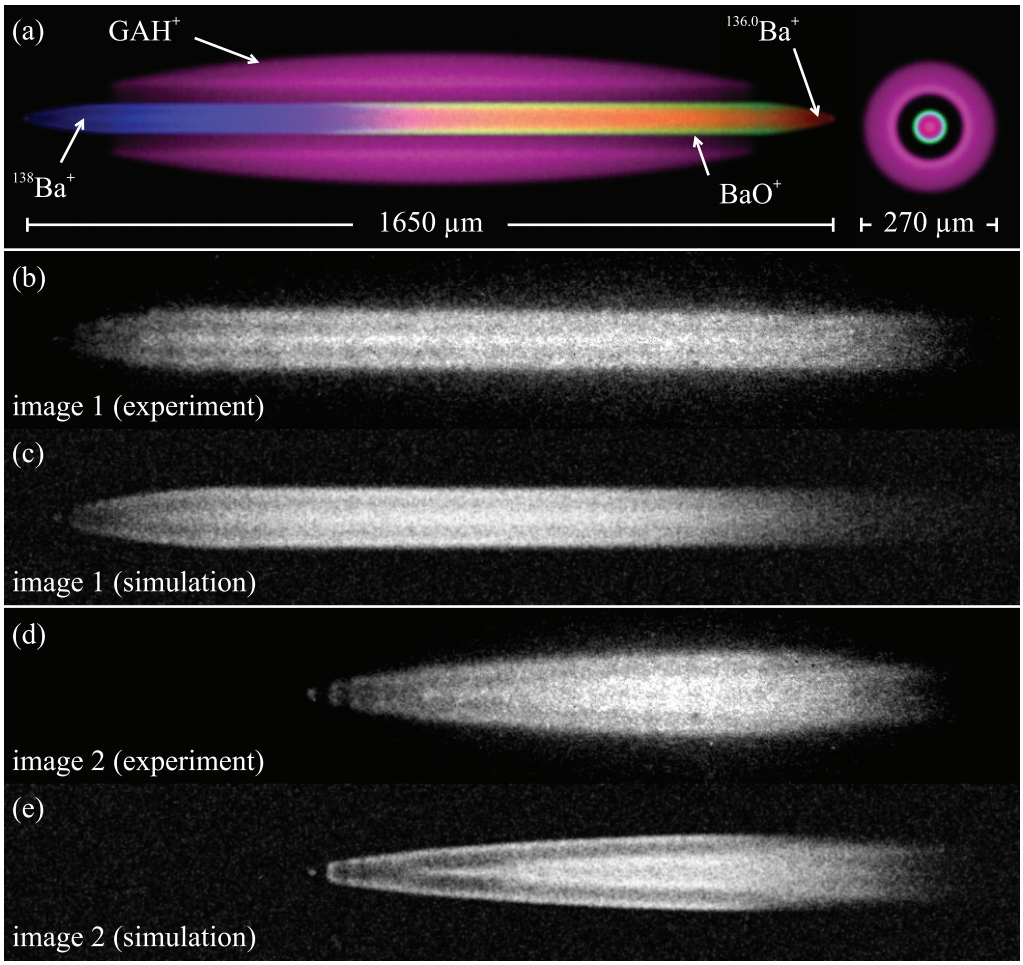

Figure 6.2: Temperature determination of sympathetically cooled GAH^+ ions. (a) Simulated image of an ion crystal consisting of 240 $^{138}Ba^+$ ions (blue), 165 $^{136.0}Ba^+$ ions (red), 150 BaO^+(green), and 1250 GAH^+(pink). The image shows the crystal as it would appear, if all ions fluoresce, in radial (left) and axial (right) view. Colors are for better visibility only. (b) Experimental CCD image of this ion crystal showing the $^{138}Ba^+$ ions surrounded by the not visible GAH^+ and BaO^+ ions at $T_1(^{138}Ba^+) = 74\,\mathrm{mK}$, $T_1(^{136.0}Ba^+) = 122^{+5}_{-20}\,\mathrm{mK}$, $T_1(BaO^+) = 119^{+5}_{-19}\,\mathrm{mK}$, and $T_1(GAH^+) = 134^{+8}_{-24}\,\mathrm{mK}$. (c) Simulated image (b) showing the fluorescing $^{138}Ba^+$ ions only. (d) Experimental CCD image of the ion crystal after removal of the GAH^+ ions for temperature determination. Here, the Ba^+ ion crystal is radially expanded and no longer axially prolonged nor heated by the GAH^+ ions. It consists of 225 $^{138}Ba^+$ ions at $T_2(^{138}Ba^+) = 28\,\mathrm{mK}$, 165 $^{136.0}Ba^+$ ions at $T_2(^{136.0}Ba^+) = 36^{+1}_{-3}\,\mathrm{mK}$, and 145 BaO^+ ions at $T_2(BaO^+) = 36^{+0}_{-3}\,\mathrm{mK}$. (e) Simulated image (d) showing the fluorescing $^{138}Ba^+$ ions only.

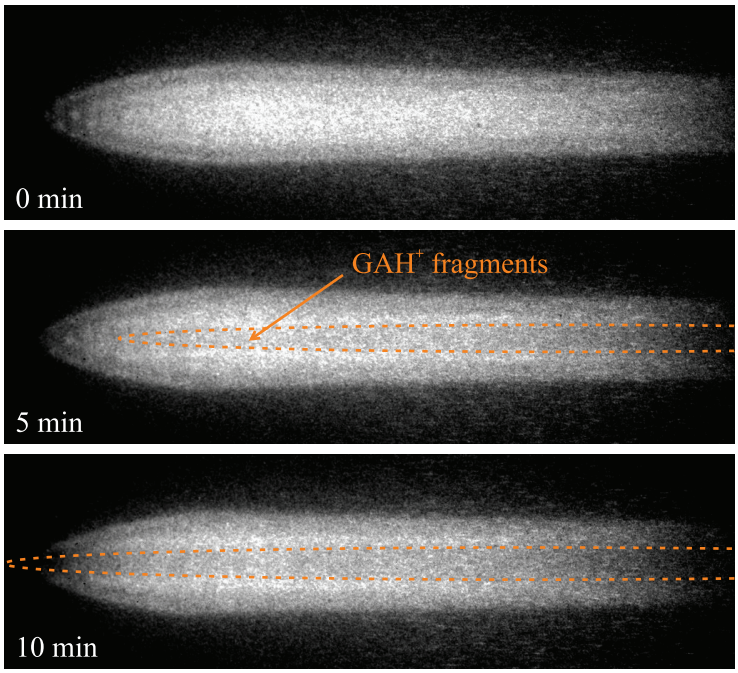

Figure 6.3: Observation of GAH^+ photodestruction. An ion crystal consisting of laser-cooled $^{138}Ba^+$ ions (visible in these CCD images), Ba^+ isotopes, BaO^+ and GAH^+ (all three not visible) is continuously exposed to 266 nm laser light of low intensity. The GAH^+ ions dissociate within minutes, their fragments accumulate along the trap axis and form a dark core (orange dashed line) inside the $^{138}Ba^+$ ion crystal.

of GAH^+ and I the intensity of the dissociation laser at the frequency $\nu = c/(266\,\mathrm{nm})$. $N_e(t)$ is the ion number in the electronically excited state. Its decay is characterized by the fluorescence rate Γ, and its photodissociation channel by the unimolecular dissociation rate k. The solution for the total parent ion number $N(t) = N_g(t) + N_e(t)$ in the relevant case $R \ll k, \Gamma$ at the low intensities I used in our measurements is given by

$$N(t) = N(0) \cdot \exp(-\gamma t) \tag{6.3}$$

with the photodestruction rate

$$\gamma = \frac{kR}{k+\Gamma}. \tag{6.4}$$

The decay of the total parent GAH^+ ion number $N(t)$ is measured with the two methods described in the two following chapters. Fits with Eq. (6.3) to the obtained decay curves yield the photodestruction rates γ. Note again that this rate is not a photodissociation rate in the sense of an inverse lifetime of an excited molecule against dissociation. Instead, it is determined by the absorption rate R, the fluorescence rate Γ, and the rates for various dissociation pathways.

6.2 Secular excitation method

As described in Chapter 4.1, the excitation of motional resonance frequencies in a multi-species ion crystal leads to dips of the laser-cooled barium ions' fluorescence. The height of these dips depends on several factors, such as the excitation amplitude or the laser cooling power, but as well on the number of ions of the excited species.

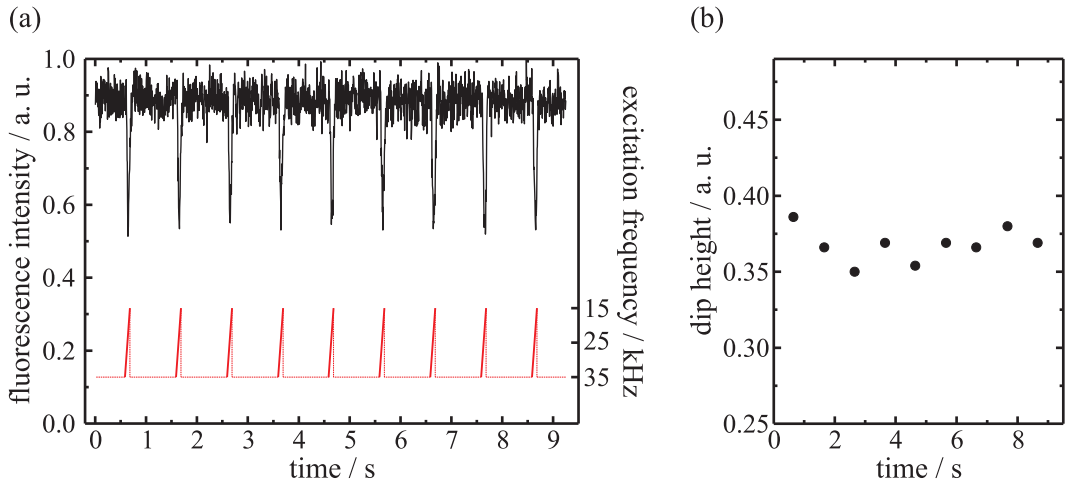

Figure 6.4: Secular excitation of GAH^+. (a) With a repetition frequency of 1 Hz, excitation scans (red curve) from 35 to 15 kHz within 0.1 s duration are applied to a Ba^+/GAH^+ ion crystal. Fluorescence dips (black curve) occur at the GAH^+ resonance frequency of 24.5 kHz. (b) The dips are all of the same height with fluctuations of less than 5 %.

When a motional resonance is scanned repeatedly under constant conditions, fluorescence dips of the same height with fluctuations of less than 5 % are produced. Fig. 6.4 shows an example of a Ba^+/GAH^+ ion crystal that is repeatedly excited with a repetition frequency of 1 Hz with frequency scans from 35 to 15 kHz within 0.1 s. The GAH^+ fluorescence dip at 24.5 kHz is reproduced in its height at every scan because the number of GAH^+ ions does not change.

However, when the number of ions of the excited species decreases, the height of the fluorescence dips decreases as well. This is due to the fact that the excitation of a smaller number of ions leads to a lower effect on the barium ions and their fluorescence intensity. The dip height is approximately proportional to the number of the excited ions [68], which has also been confirmed in this work (Chapter 6.4). Thus, secular excitation can be used to observe the photodestruction of a trapped molecular species live during the whole decay process.

Fig. 6.5 shows an example of a Ba^+/GAH^+ ion crystal which is exposed to 266 nm UV laser light. During the photodestruction of the GAH^+ ions, frequency scans covering the GAH^+ resonance at 29.1 kHz[1] are applied with a repetition frequency of 0.8 Hz. The height of the fluorescence dips decreases exponentially until it scatters around a certain value. An exponential fit using Eq. (6.3) yields a photodestruction rate for GAH^+ of $\gamma = 0.17\,\mathrm{s}^{-1}$ at a wavelength of 266 nm and an intensity of 12 $\mathrm{mW/cm^2}$.

The high deviations of the measured dip heights from the exponential fit curve have to be ascribed to the strong changes of the ion ensemble during the photodestruction process. Every single ion that leaves or enters the ion ensemble causes a rearrangement of all other ions due to their strong Coulomb interaction. Additionally, the produced GAH^+ fragment ions can have high kinetic energies and heat up the ion ensemble until they are finally trapped inside the barium ion ensemble.

Most striking, however, is the fact that the GAH^+ resonance dips do not vanish completely when all parent ions are destructed. This is due to an unfortunate circumstance for this test

[1] Note that the resonance frequencies of the trapped ion species mainly depend on the applied trap RF amplitudes. Therefore, the GAH^+ resonance frequencies in the cases presented in Fig. 6.4, Fig. 6.5, and Fig. 6.6 differ due to different RF amplitudes applied.

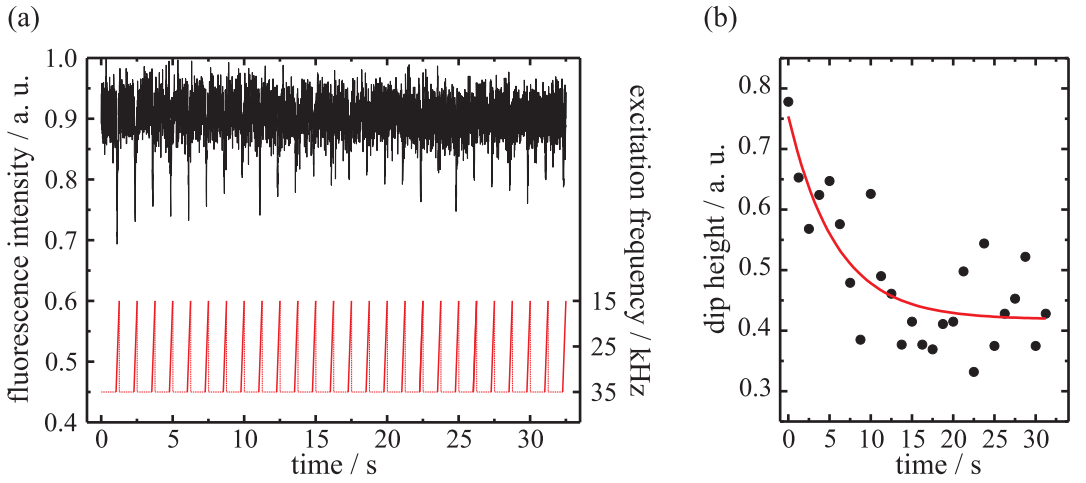

Figure 6.5: Secular excitation of GAH^+ during photodestruction. (a) A Ba^+/GAH^+ ion crystal is exposed to 266 nm UV laser light at an intensity of 12 mW/cm^2. During the photodestruction of the GAH^+ ions, excitation scans from 35 to 15 kHz within 0.2 s at a repetition frequency of 0.8 Hz are applied. At the GAH^+ resonance frequency of 29.1 kHz fluorescence dips occur whose heights vary. (b) The dip heights decrease exponentially to a certain value. A fit using Eq. (6.3) yields a photodestruction rate of $\gamma = 0.17\,s^{-1}$.

molecule GAH^+ and probably also for other molecules with similar masses (471 ± 50 Da). Here, during the photodestruction a new resonance arises close to the parent GAH^+ ion resonance, which cannot be resolved and just slightly broadens the observed parent ion dip (Fig. 6.6). This new resonance can be explained as being due to the generated fragment ions. Their mass-to-charge ratios of 40 to 82 Da do not only lead to radial resonances between 260 and 130 kHz as measured and expected from Eq. (2.12) with $U_{RF} = 291$ V as applied in the case of Fig. 6.5, but also to an additional resonance which coincidentally agrees with that of the parent ions (≈ 29 kHz in this case, see Fig. 6.6 for details). This can be explained by the motional coupling of all trapped ions (Chapter 4.1).

Even so, an evaluation of the rates of the GAH^+ photodestruction processes measured with this method is possible and leads to results that agree well with those measured with the ion extraction method (see Fig. 6.10, open circles) described in the next chapter. For other parent ion masses sufficiently different from that of GAH^+, this problem will not occur, as their resonances can be resolved from those arising from their fragments.

6.3 Ion extraction method

In order to measure photodestruction rates using the ion extraction method (Chapter 4.2), ion crystals prepared under identical conditions containing the desired molecular ions are exposed to the destruction laser for different, sequentially increased times. The resulting ion crystals in different stages of the destruction process are analyzed via ion extraction. Thus, the decay of the parent ion number is fully described by such a set of ion extraction spectra.

Fig. 6.7 shows ion extraction spectra of identically prepared Ba^+/GAH^+ ion crystals in different stages of the GAH^+ destruction by 266 nm laser light of 55 mW/cm^2 intensity. The red curve is the extraction spectrum of an intact Ba^+/GAH^+ ion crystal acquired directly after preparation showing only the two species. The green curve was acquired after an

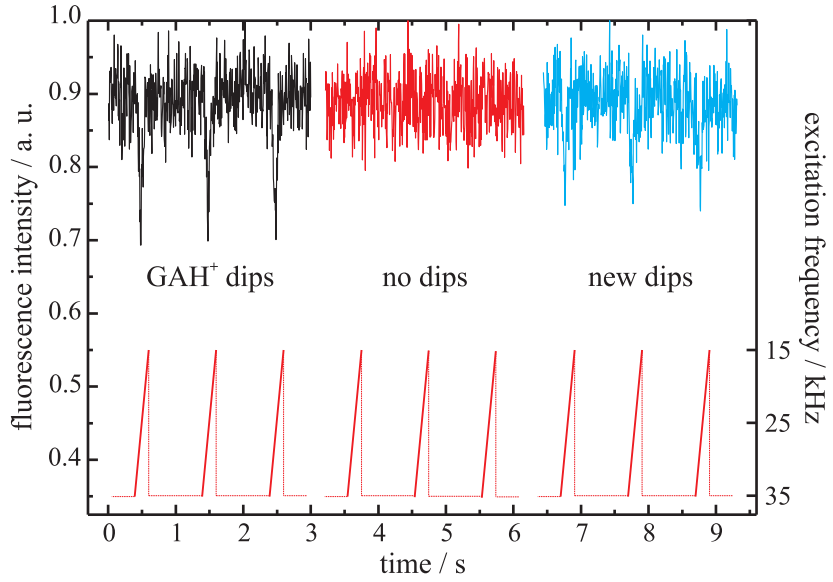

Figure 6.6: GAH^+ fragment coupling resonances. The three plots show the barium fluorescence intensity of three different ion ensembles at identical trap parameters during 1 Hz repeated excitation scans from 35 to 15 kHz within 0.2 s. The black curve belongs to a Ba^+/GAH^+ ion crystal with GAH^+ resonance dips at 27.0 kHz. The red curve was acquired after the GAH^+ ions have been removed from the trap completely by a strong excitation, so there are no dips in the scanned frequency range anymore. The blue curve belongs to a Ba^+/GAH^+ ion crystal in which all GAH^+ ions have been destructed. Thus, the resonance dips at 28.7 kHz cannot be ascribed to GAH^+ ions and have to be generated by the GAH^+ fragment ions through motional coupling with all other ions.

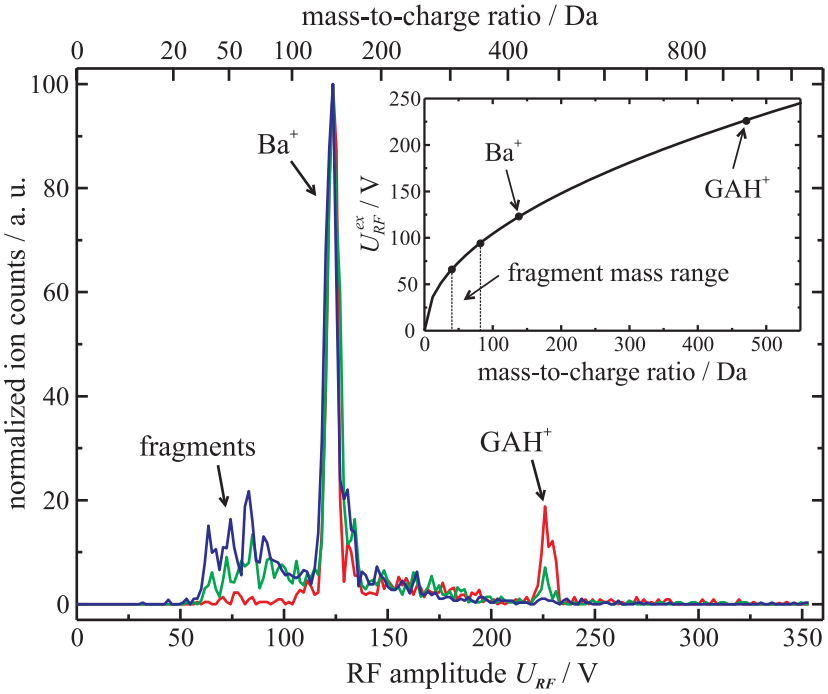

Figure 6.7: Ion extraction spectra of different GAH^+ destruction stages. The red curve is the extraction spectrum of an intact Ba^+/GAH^+ ion crystal showing only the two peaks. The green curve shows the extraction spectrum of an identically prepared crystal after a 1.2 s exposition to 266 nm laser light at 55 mW/cm^2 with a reduced GAH^+ ion number and appearing fragments. After 2.4 s (blue curve) all GAH^+ ions are dissociated, and the number of fragments reaches a final maximum. The inset shows the dependency of the extraction RF amplitude U_{RF}^{ex} on the mass-to-charge ratio which, calibrated with the known mass of barium, confirms trapping of GAH^+ and reveals the mass-to-charge ratios of the fragments.

UV exposition of 1.2 s and shows a reduced number of GAH^+ ions and the appearance of fragments. After 2.4 s, all GAH^+ ions are dissociated and the number of fragments reaches a final maximum as shown in the blue curve. From the RF amplitude U_{RF} at which an ion species leaves the trap during an ion extraction its mass-to-charge ratio can be derived. Using the Ba^+ peak for calibration, the mass-to-charge ratio of GAH^+ is well confirmed (see inset of Fig. 6.7), and the fragments mass-to-charge ratio range can be determined to $40 - 82$ Da.

By adding the ion counts of the parent ion peak in each extraction spectrum, a parent ion decay curve is obtained from such a set of ion extraction spectra (Fig. 6.8(a)). However, although all starting ion crystals of a dissociation run are prepared under identical conditions, there are deviations in the numbers of loaded molecular ions which have to be ascribed to the irregular ion flux of the ESI ion source as treated below. Therefore, several complete destruction runs need to be measured for the same conditions (same laser intensity and wavelength) and averaged in order to minimize this non-systematic error.

Fig. 6.8(a) shows the decay of the GAH^+ parent ion number in four sets with each consisting of 11 ensembles exposed to UV light for sequentially increased durations. The numbers of counted GAH^+ ions for each UV exposure time have been averaged and are plotted in Fig. 6.8(b). An exponential fit with Eq. (6.3) to these data points yields the photodestruction rate $\gamma = (1.00 \pm 0.13)\mathrm{s}^{-1}$ for this destruction process at 55 mW/cm^2. In

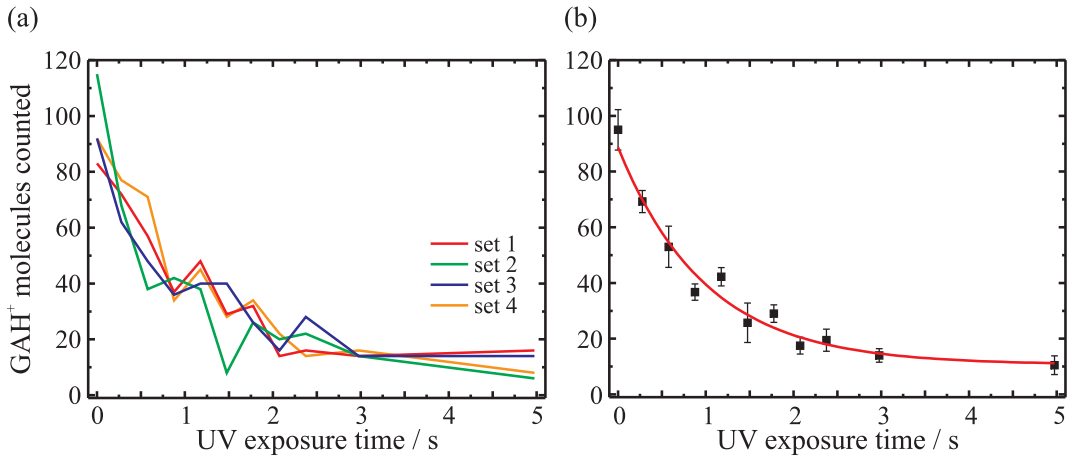

Figure 6.8: Photodestruction of GAH^+ measured via ion extraction. (a) Decay curves of the GAH^+ parent ion number in four sets with each consisting of 11 ensembles exposed to UV light for increased durations. (b) Average values of the four decay curves with an exponential fit that yields a photodestruction rate of $\gamma = (1.00 \pm 0.13)\,\mathrm{s}^{-1}$.

this work, the photodestruction rate of GAH^+ at 266 nm has been measured for different laser intensities in the range from 3 to 440 $\mathrm{mW/cm^2}$ mainly using the ion extraction method as presented in Chapter 6.4.

Averaging over several complete destruction runs is required in the ion extraction method due to the deviations in the preparation of initial Ba^+/GAH^+ ion crystals. These deviations have to be fully ascribed to the fluctuations of the molecular ion flux of the ion source which are in the range of 25 %, being typical for ESI based ion sources (Fig. 6.9(a)). Occurring within less than a second, these fluctuations are present to the full extent even on the typical timescales of loading the molecular ions to the trap (b). In consequence, the numbers of GAH^+ ions in the initial Ba^+/GAH^+ ion crystals (c), as well as in crystals exposed to UV light for the same duration (d) fluctuate in the same range of 25 to 30 %. Other factors that affect the trapping efficiency for the molecular ions, such as the buffer gas pressure, the endcap electrode voltage, the RF amplitude, or the octopole transfer time, are much better reproducible, so that their effect can be neglected. Fluctuations of this range can explain, why the number of residual GAH^+ ions in a crystal exposed to UV for a longer duration can be higher as that in a crystal exposed for a shorter time (see several cases in Fig. 6.8(a)). A higher reproducibility in the production of initial ion crystals could be achieved by loading for longer octopole transfer times with lower buffer gas pressures. However, even low buffer gas pressures maintained for longer time intervals have a negative effect on the vacuum in the ion trap chamber, as it will take longer to achieve the initial vacuum conditions.

6.4 Results

To demonstrate the practicability of the two methods, the photodestruction of GAH^+ with a cw 266 nm laser at low intensities ranging from 3 to 440 $\mathrm{mW/cm^2}$ has been investigated in this work. Fig. 6.10 shows the photodestruction rates obtained with the ion extraction method (filled circles) and the secular excitation method (open circles, inset). The measured rates range from 0.05 to 6.5 s^{-1} and linearly depend on the dissociation laser intensity indicating a single-photon process. Significantly lower rates can in principle be observed

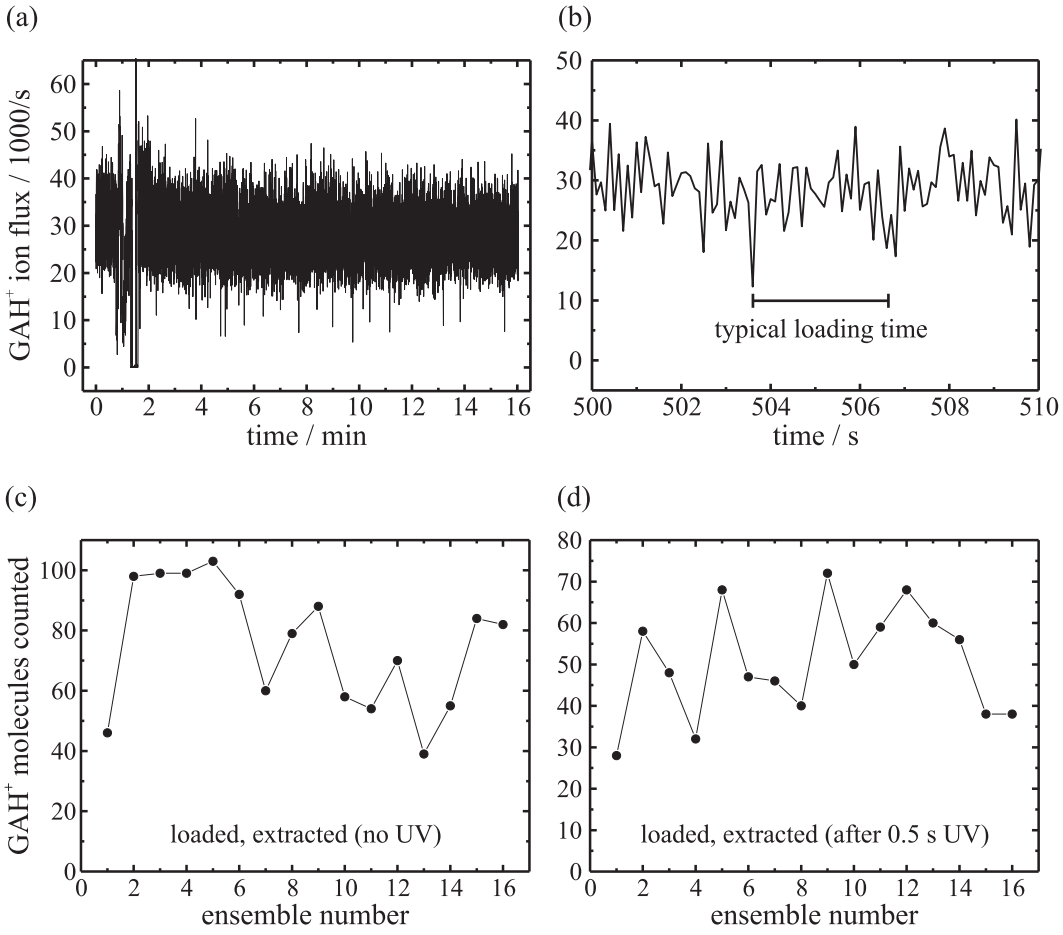

Figure 6.9: Fluctuations of the molecular ion flux. The GAH^+ ion flux reaching the ion trap fluctuates with a standard deviation of 25 % (a), even on the timescale of typical loading times as shown in (b). In consequence, the number of GAH^+ ions in the initial Ba^+/GAH^+ ion crystals (c) and in crystals exposed to UV light for the same duration (d) fluctuate in the same range, although prepared under identical conditions.

due to the long-term stable storage of the molecular ions of up to hours. Measurements of rates higher than $\sim 0.5\ \mathrm{s}^{-1}$ are not possible with the secular excitation method as the excitation repetition rate is limited to $\lesssim 2$ Hz. With higher repetition rates the crystals cannot cool down sufficiently after excitation to maintain crystallization. In contrast, in the extraction method the upper limit of measurable rates is only limited by the shutting time of the destruction lasers, which is in the range of milliseconds using mechanical shutters (used here) or nanoseconds for electro-optical switches.

With the relation $\gamma = \sigma \cdot I/h\nu$ valid for the rate γ of single photon processes and Eq. (6.4), one can define a photodestruction cross section

$$\sigma_{pd} = \sigma_{abs} \frac{k}{k + \Gamma}. \tag{6.5}$$

A linear fit to the data in Fig. 6.10 yields a photodestruction cross section at 266 nm of translationally cold, trapped GAH^+ ions of $\sigma_{pd} = (1.1 \pm 0.1) \cdot 10^{-17}\,\mathrm{cm}^2$. Only few quantitative measurements on UV photodestruction cross sections of trapped molecular ions have been performed. Similar measurements on trapped, but warm CH_4^+ [69] yielded smaller photodestruction cross sections on the order of $1 \cdot 10^{-19}$ cm^2 for visible wavelengths, with a tendency to increase with decreasing wavelengths.

In our model, for high photodissociation rates $k \gg \Gamma$, the photodestruction cross section σ_{pd} would equal the absorption cross section σ_{abs}. There are no quantitative measurements on the UV absorption cross section of GAH^+, but numerous absorption cross sections of other similar gas-phase organic molecules have been measured. For example, a gas-phase amide (C_4H_9NO) shows an absorption cross section at 266 nm of $\sigma_{abs}(266\mathrm{nm}) \approx 5 \cdot 10^{-19}$ cm^2 [70] and neopentylperoxy radical molecules ($C_5H_{11}O_2$) $\sigma_{abs}(266\mathrm{nm}) \approx 4 \cdot 10^{-18}$ cm^2 [71]. Both are lower than the measured photodestruction cross section of GAH^+, which itself is lower than the absorption cross section according to Eq. (6.5). Thus, compared with these examples, the absorption cross section of cooled, trapped GAH^+ is significantly higher. Another example that shows a more comparable absorption cross section are fullerenes (C_{60}), for which at the same wavelength an absorption cross section of $\sigma_{abs}(266\mathrm{nm}) \approx 4 \cdot 10^{-16}$ cm^2 has been measured [72].

6.5 Comparison

The two methods presented are based on fundamentally different principles and therefore show diverse advantages and difficulties. The most striking difference is the time it takes to measure a photodestruction rate for a given spectroscopy condition. Under best experimental conditions, such a measurement takes a few minutes with the secular excitation method, whereas it takes at least one hour with the ion extraction method. This is because in the latter case dozens of ion crystals need to be prepared and destructed to achieve lower relative uncertainties, compared to only one crystal in the first case.

However, this speed difference is often compensated by the higher experimental effort of the secular excitation method. Here, it is a complex task to produce ion crystals with a certain required critical ratio of numbers of laser-cooled atomic ions and sympathetically cooled molecular ions. Two conditions need to be balanced − the signal-to-noise ratio of the resonance dips needs to be sufficiently high, and the ion ensembles need to stay in the crystal state during the whole destruction process. The first condition, a high signal-to-noise ratio, can easily be achieved with a higher number of molecular ions that is only limited by the finite sympathetic cooling power of the laser-cooled ions. However, the maintenance of the crystal state is more critical because every resonant excitation

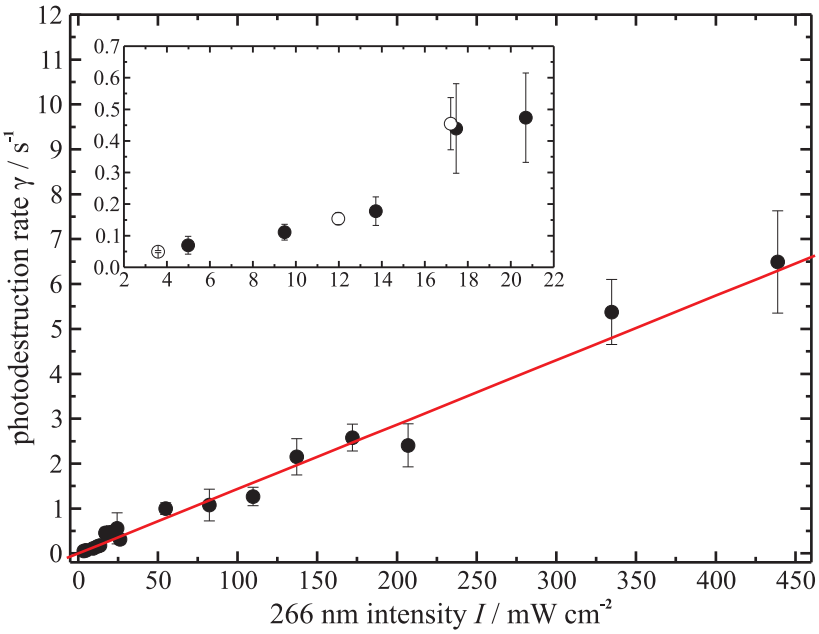

Figure 6.10: Photodestruction rates of cold GAH^+ at different laser intensities. The rates γ show a linear dependence on the 266 nm destruction laser intensity I in the range of intensities covered (the red line is a linear fit). The rates measured with the secular excitation method (open circles, inset) agree well with those measured with the ion extraction method (filled circles).

of the ions implies a disturbance. When the number of molecular ions is too large, the ion crystals melt before the destruction process is finished, as they are perturbed by the produced fragment ions due to their stronger sympathetic interaction with the laser-cooled ions. In addition, with higher numbers of molecular ions and their fragments, the ion crystals are more sensitive, so that slightly stronger or more frequent excitations can easily melt the crystals. Thus, the preparation and the handling of barium/molecule ion crystals for the application of the excitation technique requires a precise and critical control of the loading and excitation parameters.

In comparison, the extraction method is less sensitive, but more straightforward as it does without the crucial excitation. Here, the only condition to be fulfilled, is to prepare ion crystals with a sufficient number of molecular ions that produces a distinct peak in the ion extraction spectra. Once the right settings are found, it is an uncomplicated step-by-step procedure to produce, destruct, and extract the molecular ion ensembles, which can be automated to a large extent. Thus, for spectroscopic studies, where hundreds of rates at different wavelengths need to be measured, the ion extraction method would be the method of choice.

6.6 Outlook

In future, the presented methods, especially the ion extraction method, could be applied for systematic acquisitions of highly resolved photodestruction spectra. Several spectroscopic schemes are possible, such as the direct destruction using low intensity, tunable cw UV lasers, or IR depletion spectroscopy as described by Stearns et al. [9] (see Fig. 6.11). Here, cooled, trapped protonated alanine-tyrosine ions ($AlaTyrH^+$) are excited with a fixed frequency UV dissociation laser above the dissociation threshold, and a certain fragment ion

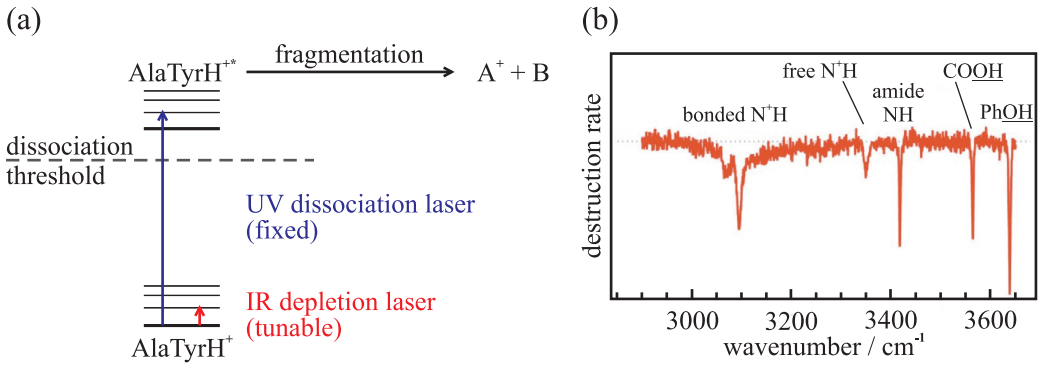

Figure 6.11: Principle of IR depletion spectroscopy [9]. (a) Cold, trapped protonated alanine-tyrosine ions ($AlaTyrH^+$) are exposed to UV and IR laser light. The dissociation of the molecules by the fixed frequency UV dissociation laser can be reduced by a tunable IR depletion laser at vibrational resonances. (b) In the IR spectrum of the fragment ion yield, which corresponds to the parent ion destruction rate, vibrational transitions can be identified by comparison to calculated spectra.

yield is measured that corresponds to a certain parent ion destruction rate. An additional tunable IR laser is used to excite vibrational transitions of the molecular ions. In case of a vibrational resonance, the population in the vibrational ground state is depleted and the destruction rate is reduced. Hence, the dips in the destruction rate spectrum (Fig. 6.11(b)) correspond to certain vibrational transitions.

Similar measurements could be performed in our apparatus on these $AlaTyrH^+$ ions, which have already been trapped and sympathetically cooled within this work (see Tab. 5.1). Here, the detection of the weak phenol OH-stretching transition PhOH at the wavenumber $\bar{\nu}_0 = 3656\,\mathrm{cm}^{-1}$ could be a starting point for further spectroscopic investigations. Even for overtone transitions, which are more easily accessible with conventional diode lasers, excitation rates would be satisfactory as described in the following estimation.

Ishiuchi et al. [73] measured the absorption oscillator strengths f_k of the fundamental ($k = 0$) and overtone ($k = 1, 2, 3, ...$) phenol OH-stretching transition on jet-cooled phenol. For the first overtone transition at $\bar{\nu}_1 = 7143\,\mathrm{cm}^{-1}$, which corresponds to the conveniently producible wavelength $\lambda_1 = 1.40\,\mu\mathrm{m}$, the oscillator strength is given as $f_1 = 6.87 \cdot 10^{-7}$. According to [74], the absorption oscillator strength can be expressed as

$$f_k = \frac{4\epsilon_0 m_e c}{e^2} \int \sigma_{abs,k}(\nu)\mathrm{d}\nu, \tag{6.6}$$

where $\sigma_{k,abs}(\nu)$ stands for the absorption profile of the concerning transition k. Assuming a Gauß profile

$$\sigma_{abs,k}(\nu) = \sigma_{abs,0,k} \exp\left(-4\ln 2 \frac{(\nu - \nu_k)^2}{\Delta\nu_k^2}\right), \tag{6.7}$$

with a maximum absorption cross section $\sigma_{abs,0,k}$ and a full width at half maximum (FWHM) $\Delta\nu_k$, Eq. (6.6) yields

$$f_k = 2\sqrt{\frac{\pi}{\ln 2}} \frac{\epsilon_0 m_e c}{e^2} \sigma_{abs,0,k} \Delta\nu_k. \tag{6.8}$$

With the oscillator strength f_k and the line broadening $\Delta\nu_k$ known, Eq. (6.8) allows one to calculate the excitation rate

$$\frac{\mathrm{d}N}{\mathrm{d}t} = N\,\sigma_{abs,0,k}\,F_{laser}, \tag{6.9}$$

where N is the number of molecular ions exposed to the excitation laser with the photon flux $F_{laser} = I_{laser}/h\nu_k$, the laser intensity I_{laser} and the frequency ν_k.

For translationally cooled, trapped $AlaTyrH^+$ ions at an internal temperature of 300 K, the first overtone of the phenol OH-stretching transition is effectively broadened due to an overlapping of rotational transitions to $\Delta\nu_1 = 1.2\,\mathrm{THz}$ [73]. Probed by a narrowband diode laser with an intensity of $I_{laser} = 10\,\mathrm{W\,cm^{-2}}$, the excitation rate for a molecule is $\frac{dN/dt}{N} \simeq 1.0\,\mathrm{s^{-1}}$. At our experimental conditions with storage times of many minutes, such a rate would be large enough to saturate the considered transition. Collisions of the molecular ions with background gas particles are almost negligible, as collision rates for a trapped ion under typical experimental conditions are on the order of less than $0.02\,\mathrm{s^{-1}}$ according to [32]. Alternatively, in order to achieve higher excitation rates, the fundamental of the phenol OH-stretching transition with a ten times higher oscillator strength of $f_0 = 7.93 \cdot 10^{-6}$ could be probed. This would require a wavelength of $\lambda_0 = 2.74\,\mu\mathrm{m}$, which could be obtained using an optic parametric oscillator (OPO) laser that can provide intensities in the range of $10,000\,\mathrm{W\,cm^{-2}}$. Here, the excitation rate for a molecule could be significantly higher at $\frac{dN/dt}{N} \simeq 23,000\,\mathrm{s^{-1}}$.

With the current setup used in this work, the molecular ions are only cooled translationally. However, for vibrational spectroscopy a reduction of the molecular ion's internal energy is eligible in order to investigate them in the vibrational ground state and to reduce spectral congestion due to the presence of numerous conformers. This would also lead to higher excitation rates due to lower effective line broadenings as mentioned above. A cooling of the internal degrees of freedom could be implemented by radiative cooling in a cryogenic environment [75], or by collisions with cold neutral particles using cryogenic buffer gas [9] or even laser-cooled neutral atoms. Within this project, feasibility studies for the latter suggestion have been performed as described in the next chapter.

7 Collisions of neutral atoms and trapped ions

A conventional way of cooling both internal and external degrees of freedom of molecular ions in traps is using cryogenic buffer gases leading to translational and internal temperatures of a few Kelvin, but not to strong spatial confinement. A combination of sympathetic translational cooling via laser-cooled atomic ions and internal cooling might be feasible via collisional cooling of the trapped molecular ions with laser-cooled neutral atoms. Therefore, an ion trap and a magneto-optical trap could be overlapped, or a beam of laser-cooled neutral atoms could be directed to the trapped ions. In this way, temperatures $< 1\,\mathrm{K}$, i. e. below that of conventional cryogenic approaches, could possibly be reached.

A suitable neutral atomic species needs to fulfill two conditions for this purpose: It should be conveniently laser-coolable with lasers of preferable high wavelengths in order not do dissociate the molecular ions. And its ionization energy needs to be high enough in order to prevent a charge exchange with both the laser-cooled barium ions and the molecular ions.

In this work, neutral atoms of the alkali metals Li, Na, K, Rb, and Cs from dispensers and the rare earth metal Yb from an oven have been collided with trapped laser-cooled and not cooled Ba^+ ions, as well as complex molecular ions in order to test their suitability for collisional cooling. For all species charge exchange reactions with Ba^+ ions have been observed as described in Chapter 7.2 so that these species would not be suitable for collisional cooling. In contrast to the alkali metals, the collisions of Yb atoms with trapped GAH^+ and $AlaTyrH^+$ molecules were reactive and lead to the formation of adducts and fragments (Chapter 7.3).

7.1 Neutral atom sources

Neutral atoms of the alkali metals Li, Na, K, Rb, and Cs have been produced with alkali metal dispensers (*SAES Getters*) that are mounted in the ion trap chamber at a distance to the trap center of about 40 mm. Due to the dispensers' large-angle emission of atoms, trapped ion ensembles can be exposed to a uniform low-density gas of neutral alkali atoms. Alkali metal dispensers have been chosen for these studies because they feature several advantages [76]:

- very pure alkali metal output
- low gas emission and therefore suitable for application at ultra-high vacuum conditions
- rate of evaporation easily controllable via electric currents (typically 3.5 to 4.5 A)
- reproducible rate of evaporation

The alkali metal (Me) generating material inside the dispenser is a mixture of an alkali metal chromate and a reducing agent (RA). The reducing agent itself is a mixture of 84 %

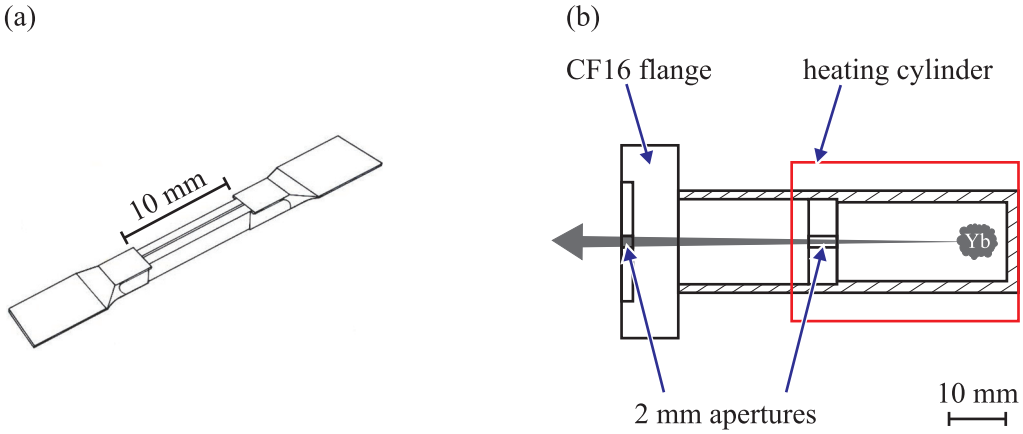

Figure 7.1: Neutral atom sources. (a) Alkali metal dispenser (*SAES Getters*) containing an alkali metal chromate with a reducing agent (image taken from [76]). When the dispenser is heated by a current, alkali atoms are released through a 10 mm long slit. (b) Ytterbium oven (*self-made*) consisting of a 60 mm steel cylinder attached to a CF16 flange. The Yb metal inside the steel cylinder is heated by a surrounding heating cylinder, two apertures of 2 mm diameter form a beam of Yb atoms.

Zr and 16 % Al, that is also able to absorb all the gases which are produced during the reduction reaction

$$\mathrm{Me_2CrO_4 + RA \longrightarrow 2\,Me + RA_2CrO_4.}$$

This mixture of reducing agent and chromate is held within a metal container with a 10 mm long slit to allow evaporation of the alkali metal vapor (Fig. 7.1(a)). A fine metal wire inside the container closes the slit, which opens when a sufficient current runs through the dispenser and starts the reduction reaction. At electric currents on the order of 4 A, the dispenser reaches temperatures of about 550 °C, and alkali metal output flows of a few micrograms per minute can be achieved [77].

In contrast to alkali metals, ytterbium is relatively stable in dry air and can be handled in elemental form. Therefore, the production of neutral Yb atoms is much easier because it can be directly evaporated from an elemental sample. Fur this purpose, a simple oven constructed in the group of Prof. Axel Görlitz consisting of a 60 mm long steel cylinder of 18 mm diameter, welded to a standard CF16 flange has been applied (Fig. 7.1(b)). A sample of several grams of pure, elemental Yb metal inside the steel cylinder can be heated with a heating cylinder surrounding the steel cylinder to temperatures of more than 700 °C. The generated Yb vapor is formed to a divergent beam of Yb atoms by using two apertures of 2 mm diameter. The oven is mounted to the ion trap chamber at a radial port that is directed to the trap center with a distance of about 200 mm to the aperture, which is made from oxygen-free copper and serves as flange gasket. Typically, the oven is heated up to 450 °C for a few minutes or seconds, increasing the pressure in the ion trap chamber to $\sim 5 \cdot 10^{-8}$ mbar due to outgassing of the Yb sample. The output flow rate of Yb can hardly be estimated, but is expected to be on a similar order of micrograms per minute as that of the alkali metal dispensers, because both oven and dispensers showed similar behaviors in tests where the metal output was deposited on a glass plate.

As the collision experiments described in this chapter were not intended to give quantitative, but rather qualitative results, the experimental setup of alkali dispensers and Yb

Species	Ionization energy / eV	Charge exchange with Ba^+in the state		
Ba	5.21	$6^2S_{1/2}$	$5^2D_{3/2}$	$6^2P_{1/2}$
Li	5.39	not studied	not studied	observed
Na	5.14	not studied	not studied	observed
K	4.34	observed	not studied	observed
Rb	4.18	observed	not studied	observed
Cs	3.89	observed	not studied	observed
Yb	6.25	observed	observed	observed

Table 7.1: Ionization energies from [78] and experimental results.

oven are very basic. No mechanisms or electronics are installed to precisely control the atom fluxes. Both the dispensers and the oven are heated by adjustable electric currents leading to atom fluxes that slowly rise to and decay from a maximum in non-determined ways. Thus, it is impossible to measure rates of the observed charge exchange reactions, also considering that the absolute atom fluxes and densities are completely undetermined.

7.2 Charge exchange reactions

Charge exchange between an ion A^+ and a neutral atom B can occur when the absolute value of the ion's electron affinity $|E_{aff}(A^+)|$ is higher than that of the neutral's ionization energy $|E_{ion}(B)|$. Note that the electron affinity of a singly ionized atom A^+ equals the negative ionization energy of the neutral atom A, i. e. $E_{aff}(A^+) = -E_{ion}(A)$. In other words, the charge exchange reaction between trapped Ba^+ ions and neutral metal atoms Me

$$Ba^+\,(\text{trapped}) + Me \longrightarrow Ba + Me^+\,(\text{trapped})$$

is allowed for $E_{ion}(Me) < E_{ion}(Ba)$.

Tab. 7.1 gives an overview of the ionization energies of the investigated atomic species and the studied charge exchange reactions depending on the different excitation states of the Ba^+ ions. The observation of the charge exchange with Li and Yb should not be possible considering the ionization energies of the involved particles alone. However, in such inelastic collisions all forms of energies of the collision partners need to be considered as they are redistributed in the collision. Thus, the required energy for the ionization of the neutral atoms does not fully have to come from the ion's electron affinity, but can be supplemented by kinetic or internal energy of both particles. In these experiments, there are the following contributions:

- The thermal kinetic energy of the neutral atoms in directed beams from the sources at temperatures of up to $T = 550\,°C$ is on the order of $E_{therm} = \frac{1}{2}k_BT \simeq 0.1\,eV$.
- The secular energy of the trapped Ba^+ ions at typical temperatures of $T = 25\,mK$ is about $E_{sec} = \frac{3}{2}k_BT \simeq 3\,\mu eV$.
- The maximum micromotion energy (Eq. (2.18)) for a Ba^+ ion in a typical ion crystal is around $E_{micro} = \frac{1}{2}m(\frac{1}{2}qr\Omega)^2 \simeq 4\,meV$.
- The internal electronic excitation energy of a Ba^+ ion in the $6^2P_{1/2}$ state is 2.51 eV, and in the $5^2D_{3/2}$ state 0.60 eV referred to the ground state.

In consequence, the translational energies of the particles E_{therm}, E_{sec}, and E_{micro} only contribute to a negligible amount of less than 0.1 eV. But the internal energy of excited

Ba^+ ions can enable charge exchange reactions that would not be possible with ions in the electronic ground state as observed for Li and Yb atoms (Chapters 7.2.3 and 7.2.4). Similar observations have been made within this project with laser-induced chemical reactions of Ba^+ ions with O_2 and CO_2 gas as described in [23, 19].

A special feature in the case of Li and Na is that their ions cannot be stably trapped in our linear quadrupole trap in the available parameter range, as their mass-to-charge ratio is too low. Thus, in contrast to K, Rb, Cs, and Yb, an accumulation of the produced ions in the trap cannot be observed. However, a loss of Ba^+ ions has been observed when they were exposed to Li and Na atoms which can only be explained by reactive charge exchange collisions.

In the following, the charge exchange reactions of K and Rb with Ba^+ (Chapter 7.2.1), of Cs with Ba^+ (Chapter 7.2.2), of Li and Na with Ba^+ (Chapter 7.2.3), and of Yb with Ba^+ (Chapter 7.2.4) are treated separately, because they differ either in the experimental procedures or in the detection methods.

7.2.1 Charge exchange of K and Rb with Ba^+

When laser-cooled Ba^+ ion crystals are exposed to K or Rb vapor from a dispenser, charge exchange between the neutral alkali metal atoms and the Ba^+ ions can be observed with the CCD camera as shown in Fig. 7.2(a) using the example of Rb. Here, the Rb dispenser is operated at 3.5 A for about 14 min, and Rb^+ ions produced at charge exchange collisions with Ba^+ ions accumulate in the ion trap. As they have a lower mass-to-charge ratio than the Ba^+ ions ($\frac{m}{Q}(Rb^+) = 85.5\,\mathrm{Da} < \frac{m}{Q}(Ba^+) = 137.3\,\mathrm{Da}$), the Rb^+ ions spatially arrange along the trap axis inside the Ba^+ ion ensemble, forming a dark core as visible in the CCD images. Fig. 7.3 shows another Ba^+/Rb^+ ion crystal as observed experimentally (a) and in a simulated view (b), in which the spatial arrangement of the Rb^+ ions (green) is illustrated.

During the 14 min the Rb dispenser is operated in the presented case, the pressure in the ion trap chamber rises from initial $8 \cdot 10^{-10}$ to maximum $9 \cdot 10^{-9}$ mbar due to the emission of various gases from the ~ 500 °C hot dispenser. As mentioned above, higher pressures lead to an increased incidence of loss reactions of laser-excited Ba^+ ions towards BaO^+ and $BaOH^+$ (usually treated as BaO^+ due to the negligible mass difference). In Fig. 7.2(a) the number of $^{138}Ba^+$ ions obviously decreases, on the one hand due to the charge exchange reactions with Rb, and on the other hand due to the laser-excited loss reaction. The accumulating BaO^+ ions arrange on the right side of the ion crystal and cause a deformation of the $^{138}Ba^+$ ion ensemble. The ion extraction mass spectrum of the resulting multi-species ion crystal after 14 min of Rb exposure (Fig. 7.2(b)) clearly shows the three species, the residual Ba^+ ions and the produced Rb^+ and BaO^+ ions.

The same observations have been made with K instead of Rb. K^+ ions with their even lower mass-to-charge ratio of $\frac{m}{Q}(K^+) = 39.1\,\mathrm{Da}$ arrange as well inside the $^{138}Ba^+$ ion ensemble and form a dark core without a visual difference to the Rb^+ core. However, K^+ and Rb^+ can be clearly distinguished and verified in ion extraction and secular excitation mass spectra (Fig. 7.4). For this purpose, pure ion ensembles have been produced that only contain Ba^+ ions and K^+ or Rb^+ ions. This can be realized, either by removing the produced BaO^+ ions via strong excitation of their secular resonance, or by exposure of a not laser-cooled Ba^+ ion ensemble to the alkali metal atoms. In the latter case, a charge exchange between Ba^+ and K or Rb is possible because the ionization energies of the two alkali metals are lower than that of Ba. However, loss reactions of Ba^+ ions with background gases are not possible because they would require laser excitation.

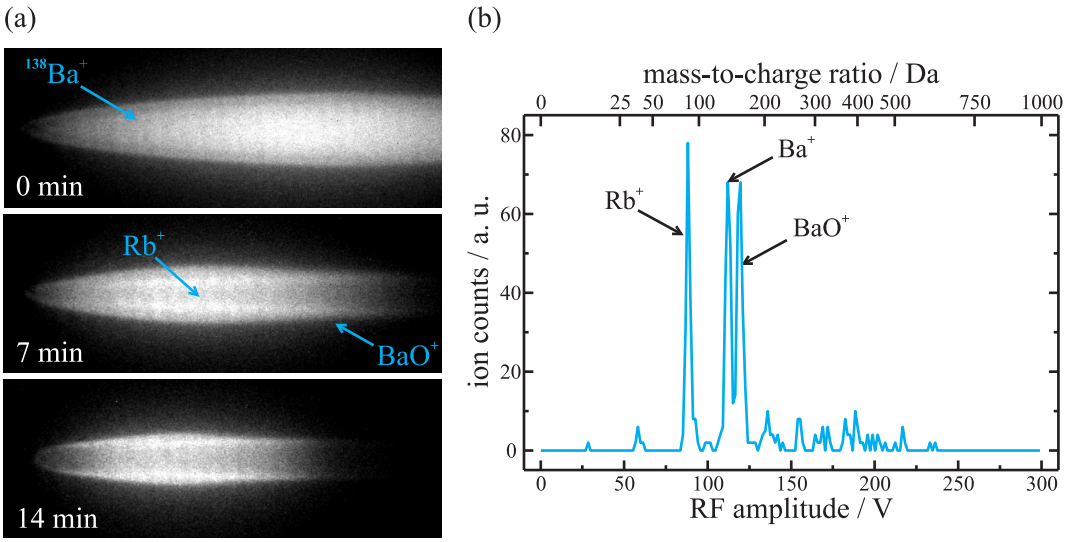

Figure 7.2: Accumulation and detection of Rb^+. (a) A laser-cooled Ba^+ ion crystal is exposed to a vapor of neutral Rb atoms. Rb^+ ions produced by charge exchange with Ba^+ accumulate in the center of the Ba^+ ion crystal, BaO^+ is produced by reactions of Ba^+ ions with background gases. (b) Ion extraction mass spectrum of the resulting ion crystal (the lower one in (a)).

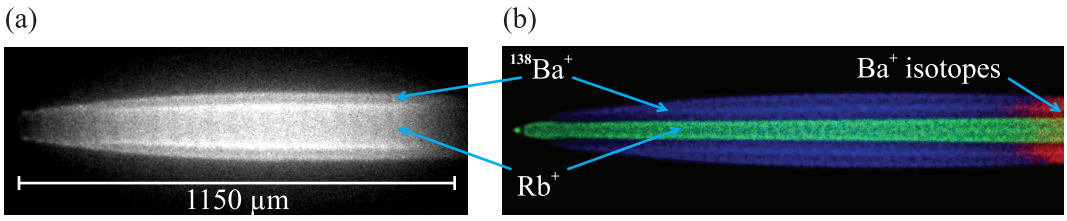

Figure 7.3: Spatial arrangement of Rb^+. (a) Experimental CCD image of a Ba^+/Rb^+ ion crystal. (b) Simulated CCD image of this crystal showing the spatial arrangement of the involved ion species $^{138}Ba^+$ (blue), Rb^+ (green), and Ba^+ isotopes (red).

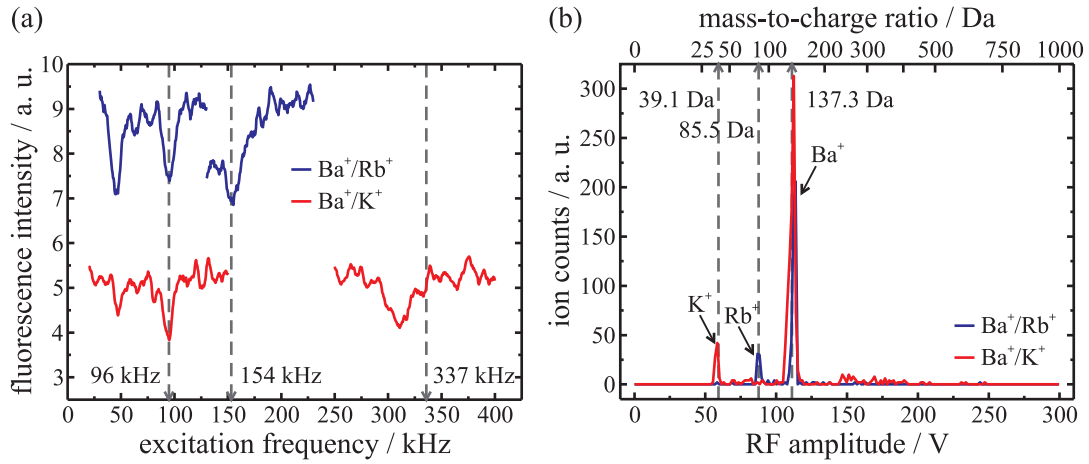

Figure 7.4: Detection of Rb^+ and K^+. (a) Secular excitation spectra of a Ba^+/Rb^+ (blue) and a Ba^+/K^+ (red) ion crystal. In both cases, the Ba^+ resonance at 96 kHz has been scanned with a lower amplitude. The expected resonances of Rb^+ (156 kHz) and K^+ (331 kHz) are well confirmed by the observed fluorescence dips. (b) Ion extraction mass spectra of these ion crystals. The upper mass-to-charge ratio axis is calibrated to the known mass of the Ba^+ ions (137.3 Da). The peaks for Rb^+ and K^+ appear close to the ions' masses of 85.5 and 39.1 Da respectively.

Such prepared pure two-species Ba^+/K^+ and Ba^+/Rb^+ ion crystals have been analyzed via secular excitation at identical trap parameters. In both cases the Ba^+ resonance occurs at a radial excitation frequency of $\nu_r^{exp}(Ba^+) = 96\,\text{kHz}$. Similar to Eq. (5.1) one can calculate the single-ion resonance frequencies expected for K^+ and Rb^+ to $\nu_r^{calc}(K^+) = 337\,\text{kHz}$ and $\nu_r^{calc}(Rb^+) = 154\,\text{kHz}$. The expected frequency for Rb^+ is very well confirmed by the measured value of $\nu_r^{exp}(Rb^+) = 155\,\text{kHz}$. The value for K^+ however with $\nu_r^{exp}(K^+) = 311\,\text{kHz}$ differs by about 8 %, which can be fully ascribed to space charge and coupling effects as described in Chapter 4.1. Indeed, coupling effects in the investigated ion crystals are very strong as the presence of the lighter alkali ions not only leads to the occurrence of their expected resonance dips above the Ba^+ resonance frequency, but also to coupling resonances slightly below 50 kHz (see Fig. 7.4(a)). The almost exact agreement of calculated and measured resonance frequency for Rb^+ could be explained by a compensation of space charge and coupling effects in this special case.

Ion crystals produced in the same way have been analyzed via ion extraction (Fig. 7.4(b)). Calibrated via the Ba^+ peak, the peaks for K^+ and Rb^+ yield the masses $m_{exp}(K^+) = 37\,\text{Da}$ and $m_{exp}(Rb^+) = 82\,\text{Da}$, that well confirm the real masses $m(K^+) = 39.1\,\text{Da}$ and $m(Rb^+) = 85.5\,\text{Da}$.

7.2.2 Charge exchange of Cs with Ba^+

Charge exchange has also been observed for Ba^+ ions and neutral Cs atoms. With a mass-to-charge ratio of $\frac{m}{Q}(Cs^+) = 132.9\,\text{Da}$ being close to that of the Ba^+ ions, the Cs^+ ions do not obviously radially separate from the Ba^+ ions. Hence, none of the usual detection schemes can be applied to verify the trapping of Cs^+ ions. In both the secular excitation and the ion extraction mass spectra the signals of Cs^+ and Ba^+ ions overlap and cannot be distinguished. However, in a Ba^+/Cs^+ ion crystal the constant light pressure force of the cooling lasers pushes the $^{138}Ba^+$ ions in propagation direction of the lasers (in all CCD images shown here this means to the left) leading to an axial separation of the Cs^+ ions

that accumulate on the right side of the crystal together with the barium isotope ions (Fig. 7.5(b)).

Such an accumulation of Cs^+ ions in a Ba^+ ion crystal has been observed experimentally and fully analyzed via MD simulations as shown in Fig. 7.5, where it is not intended to reproduce the ion temperatures, but just the ion numbers. As the Cs dispenser has been operated for in total 60 min at a current of 4.0 A reaching temperatures of about 550 °C, the amount of gases emitted from the dispenser would have lead to serious loss reactions of the laser-excited $^{138}Ba^+$ ions. To avoid this, the Cs dispenser was operated for 10 min intervals with the cooling lasers blocked, and CCD images of the Ba^+ ion crystal were taken after each exposure to the Cs atom vapor when the pressure had reached usual values of $< 1 \cdot 10^{-9}$ mbar at which loss reactions are of little importance.

The resulting series of experimental CCD images shown in Fig. 7.5(a) clearly illustrates the decrease of the number of $^{138}Ba^+$ ions. The CCD camera position and all trap parameters stayed the same when the images were taken, so the left end of the ion crystal was indeed almost fixed as it seems. This means, that the total number of trapped ions stayed the same during the whole experiment, provided that the exchanged ions had similar mass-to-charge ratios (for significantly different mass-to-charge ratios, the crystal shape would have changed completely). Comparing the real experimental and simulated CCD images allows one to determine the numbers of the trapped ion species, in this case $^{138}Ba^+$, Cs^+, $^{138}BaO^+$, and $^{136.0}Ba^+$ isotopes. The simulations for the images of this series were performed under the following conditions and reasonable assumptions:

- The total number of ions is constant.
- The numbers of Cs^+ and $^{138}BaO^+$ ions can only increase, the numbers of $^{138}Ba^+$ and $^{136.0}Ba^+$ isotope ions can only decrease.
- Cs^+ ions are produced by charge exchange collisions with both $^{138}Ba^+$ and $^{136.0}Ba^+$ isotope ions. That means, the increase of the Cs^+ ion number leads to a reduction of the barium ions distributed among the isotopes according to their proportions.
- $^{138}BaO^+$ ions are only produced from laser-excited $^{138}Ba^+$ ions.

Due to several experimental factors, these conditions cannot be combined to a theoretical model that would describe the development of ion numbers in this special case. Therefore, the control of the Cs atom flux, the vacuum pressure and the timing of procedures has not been accurate enough, as only qualitative observations were intended. However, MD simulations of each experimental CCD image under the above conditions lead to to the chronological sequence of ion numbers as presented in Fig. 7.6. Note that in this plot the continuous lines are no fits due to the lack of a model, but only help to illustrate the time behavior of the ion numbers. The total Ba^+ ion number (blue squares) decreases in an exponential-like way, and accordingly the Cs^+ (pink circles) and the $^{138}BaO^+$ (green triangles) ion numbers rise showing saturation characteristics.

7.2.3 Charge exchange of Li and Na with Ba^+

As well for neutral Li and Na atoms, charge exchange reactions with Ba^+ ions have been observed. However, in contrast to K, Rb, Cs, and Yb, the mass-to-charge ratios of the formed Li^+ and Na^+ ions are so low that they cannot be stably trapped in our ion trap at usual trap parameters. According to Eq. (2.10) and Fig. 2.4, the trap RF amplitude needs to be reduced in order to trap ions of lower mass-to-charge ratios, which in return would not allow a stable trapping of the Ba^+ ions. Thus, instead of an accumulation of the produced Li^+ and Na^+ ions in the center of the Ba^+ ion crystal, only a loss of Ba^+

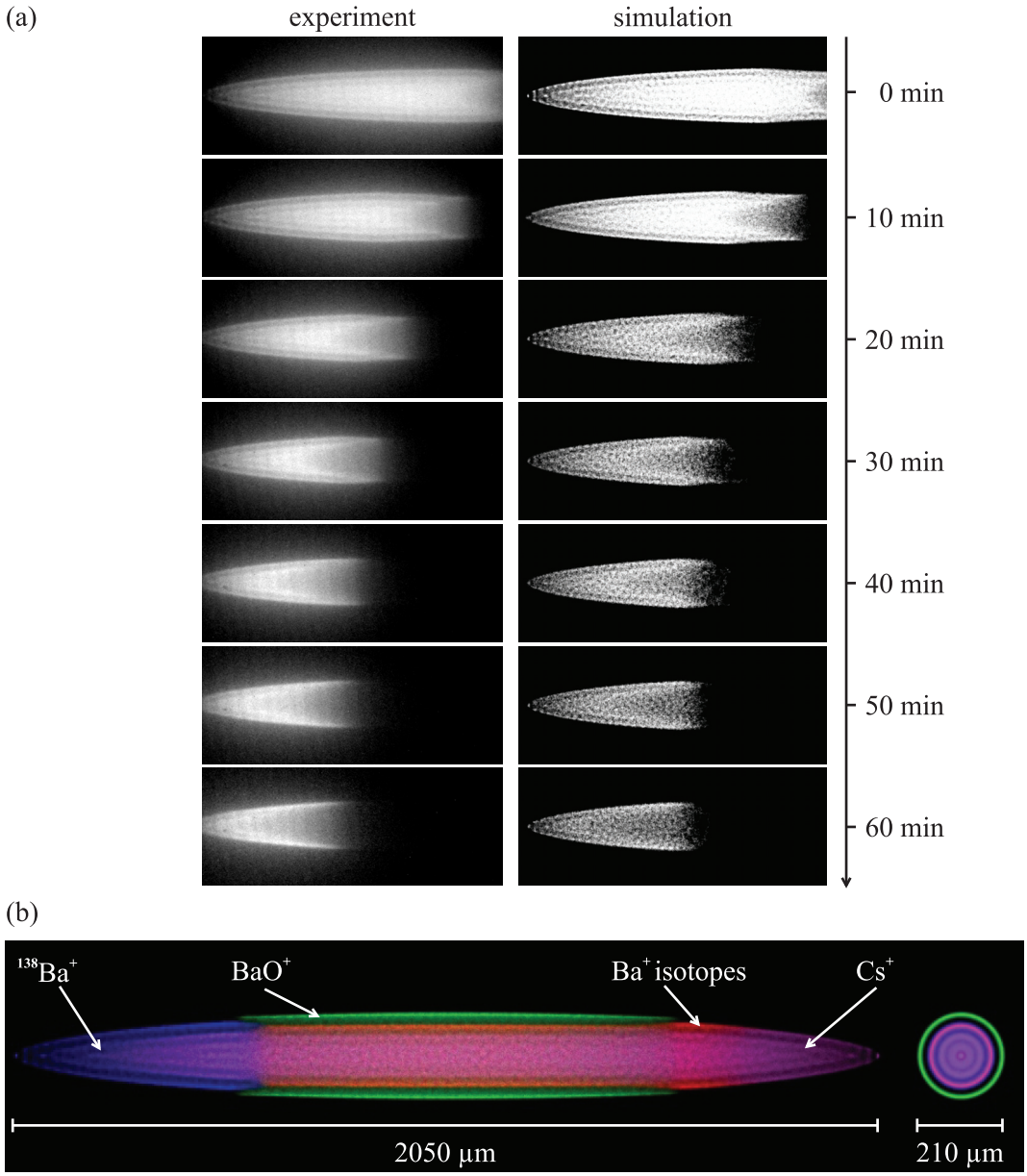

Figure 7.5: Accumulation of Cs^+. (a) A Ba^+ ion ensemble was exposed to Cs vapor from a dispenser for six 10 min intervals without laser cooling. The CCD images in the left column were taken in the beginning and after each exposure interval, when the dispenser was switched off and the vacuum pressure was at normal values. The right column shows the corresponding simulated CCD images that are not intended to reproduce the ion temperatures, but just the ion numbers (see Fig. 7.6). (b) Simulated CCD image of the 60 min image showing all involved ion species in radial (left) and axial view (right) with the $^{138}Ba^+$ ions (blue), the $^{138}BaO^+$ ions (green), the $^{136.0}Ba^+$ isotopes (red), and the Cs^+ ions (pink).

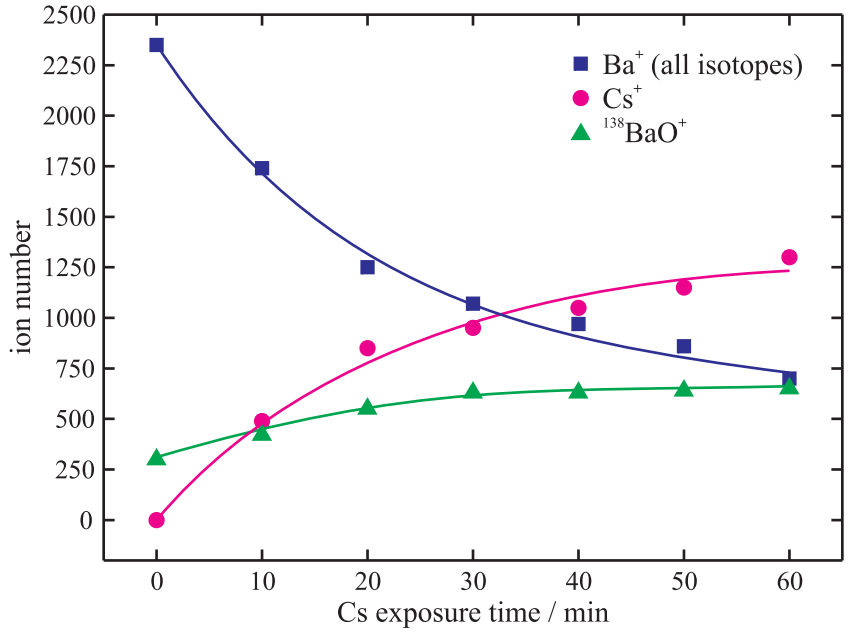

Figure 7.6: Development of ion numbers during the accumulation of Cs^+. By comparison of the experimental CCD images from Fig. 7.5 with simulated ones, the ion numbers of the involved species could be determined. The total number of Ba^+ ions (blue squares) decreases in an exponential-like way, accordingly the numbers of Cs^+ (pink circles) and $^{138}BaO^+$ ions (green triangles) grow saturation-like.

ions can be observed when a Ba^+ crystal is exposed to Li and Na vapor (Fig. 7.7 and 7.8). A loss due to elastic collisions of the neutral atoms and the trapped ions can be excluded, as the depth of the trap potential is in the range of several electronvolts and the kinetic energy of the neutral atoms from the dispenser only in the range of tens of an electronvolt.

Fig. 7.7(a) shows a Ba^+ ion crystal before and after the exposition to neutral Li atoms from a dispenser operated for 12 min at up to 3.8 A reaching a temperature of $\sim$ 500 °C. Afterwards, the Ba^+ ion crystal is much smaller due to two loss channels: Firstly, BaO^+ ions have been formed from laser-excited Ba^+ ions and background gases and accumulated in the ion trap leading to a radial constriction on the right side of the Ba^+ ion crystal. Secondly, reactive collisions of neutral Li atoms with laser-excited Ba^+ ions lead to the formation of Li^+ ions and neutral Ba atoms which were both not trapped. Fig. 7.7(b) shows the ion extraction spectrum of the resulting ion crystal where only the Ba^+ and BaO^+ can be detected and no Li^+ ions at all. As the ion crystal has not been imaged completely unfortunately, only approximate simulations could be performed to derived the numbers of the involved ion species. Before the exposition to Li, there were about 1300 Ba^+ ions, and afterwards their number was reduced to about 600, while about 300 BaO^+ ions have been formed. Thus, about 400 Ba^+ ions were lost during charge exchange reactions with neutral Li atoms, i. e. about 30 %. This reaction rate agrees very well with the charge exchange reactions observed, for example, between Cs and Ba^+ as shown in Fig. 7.6.

Similar results have been obtained for Na. Fig. 7.8(a) shows a Ba^+ ion crystal before and after the exposition to neutral Na atoms from a dispenser operated for 18 min at up to 3.8 A reaching a temperature of $\sim$ 500 °C. The CCD images show a loss of Ba^+ ions due to the formation of BaO^+ (trapped) and Na^+ (lost), which is reflected in the ion extraction spectrum shown in Fig. 7.8(b) in which only Ba^+ and BaO^+ occur. Approximate simu-

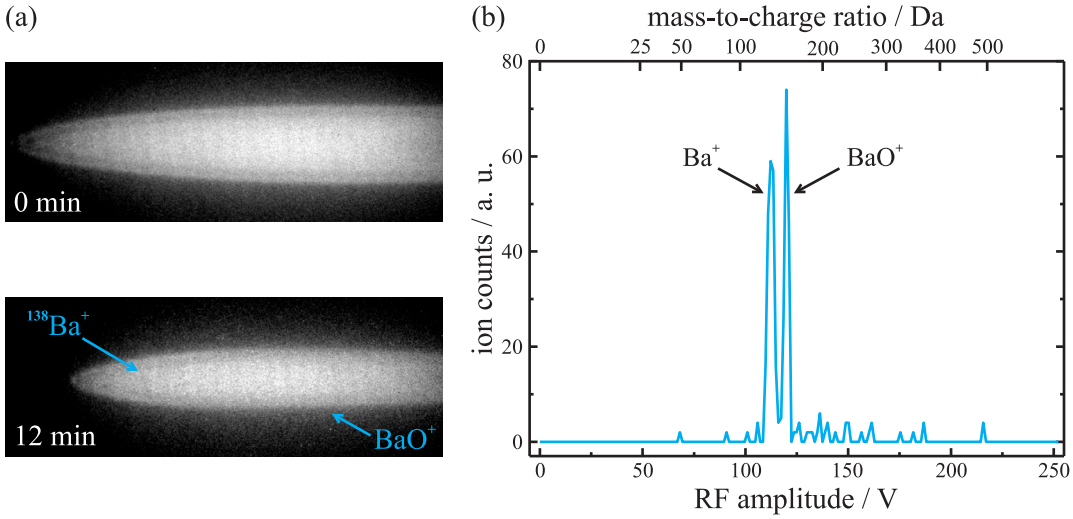

Figure 7.7: Ba^+ loss due to charge exchange with Li. (a) A Ba^+ ion crystal was exposed to Li vapor from a dispenser for 12 min. Charge exchange collisions lead to a loss of Ba^+ and a production of Li^+ ions, which cannot be stably trapped due to their low mass. (b) The ion extraction spectrum of the lower CCD image does not show Li^+ ions, but only Ba^+ and BaO^+ ions which were produced by reactions of laser-excited $^{138}Ba^+$ ions with background gases.

lations in this case yield, that the initial number of about 1000 Ba^+ ions was reduced to about 300, while about 300 BaO^+ ions have been formed. Thus, approximately 400 Ba^+ ions were lost during charge exchange reactions with neutral Na atoms, i. e. about 40 %.

7.2.4 Charge exchange of Yb with Ba^+

Charge exchange reactions have been observed between neutral Yb atoms from an evaporation oven and trapped Ba^+ ions with different rates depending on the Ba^+ ions' excitation state as described below. With a mass-to-charge ratio of $\frac{m}{Q}(Yb^+) = 173.0\,\mathrm{Da}$ being sufficiently larger than that of the Ba^+ ions, the Yb^+ ions radially separate and form a sheath around the the visible $^{138}Ba^+$ ion crystal. This causes a characteristic radial contraction of the $^{138}Ba^+$ ion ensemble as shown in Fig. 7.9. In this example, MD simulations yield that the Ba^+ ion crystal consists of about 515 $^{138}Ba^+$ ions (blue) and 195 $^{136.0}Ba^+$ isotope ions (red), and is radially squeezed by about 295 Yb^+ ions (green).

To produce such a Ba^+/Yb^+ ion crystal, a pure Ba^+ ion crystal is prepared and exposed to Yb vapor from the evaporation oven operated at typically 460 °C for about 1 min. During this time the pressure in the vacuum chamber rises up to $8 \cdot 10^{-8}\,\mathrm{mbar}$ due to the emission of gases from the oven walls and the Yb sample itself. BaO^+ ions produced by the unavoidable loss reactions of the laser-excited $^{138}Ba^+$ ions can be removed via a strong secular excitation of their motional resonance. Fig. 7.10 shows the ion extraction mass spectrum of a pure Ba^+/Yb^+ ion crystal. Calibrated with the Ba^+ peak, the peak for Yb^+ yields the mass $m_{exp}(Yb^+) = 172\,\mathrm{Da}$ which very well confirms its real mass mentioned above.

Although a selective removal of BaO^+ with a mass-to-charge ratio of $\frac{m}{Q}(BaO^+) = 154.0\,\mathrm{Da}$ even closer to that of Ba^+ than Yb^+ is possible, Yb^+ cannot be distinguished in secular excitation spectra. During the removal of an ion species via strong secular excitation, the ion crystal melts completely. During the acquisition of a secular excitation spectrum the ion crystal should not melt. However, motional coupling between the trapped ion species

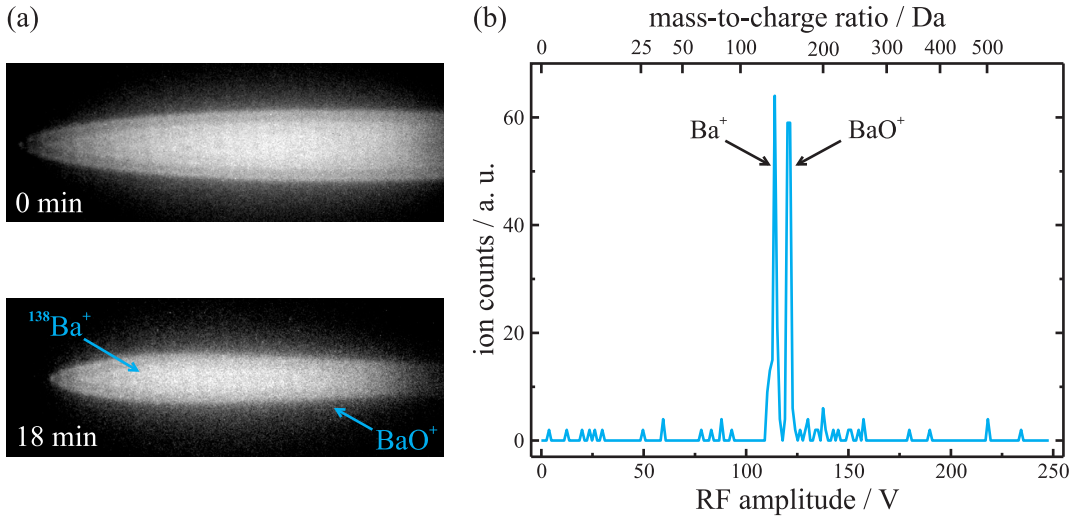

Figure 7.8: Ba^+ loss due to charge exchange with Na. (a) A Ba^+ ion crystal was exposed to Na vapor from a dispenser for 18 min. Charge exchange collisions lead to a loss of Ba^+ and a production of Na^+ ions, which cannot be stably trapped due to their low mass. (b) The ion extraction spectrum of the lower CCD image does not show Na^+ ions, but only Ba^+ and BaO^+ ions which were produced by reactions of laser-excited $^{138}Ba^+$ ions with background gases.

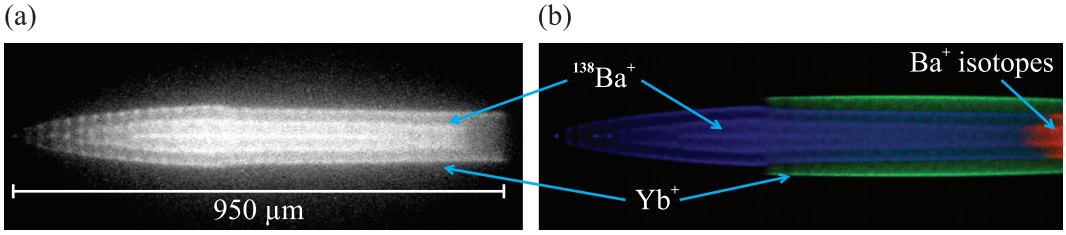

Figure 7.9: Spatial arrangement of Yb^+. (a) Experimental CCD image of a Ba^+/Yb^+ ion crystal. (b) Simulated CCD image of this crystal showing the spatial arrangement of the involved ion species $^{138}Ba^+$ (blue), Yb^+ (green), and Ba^+ isotopes (red).

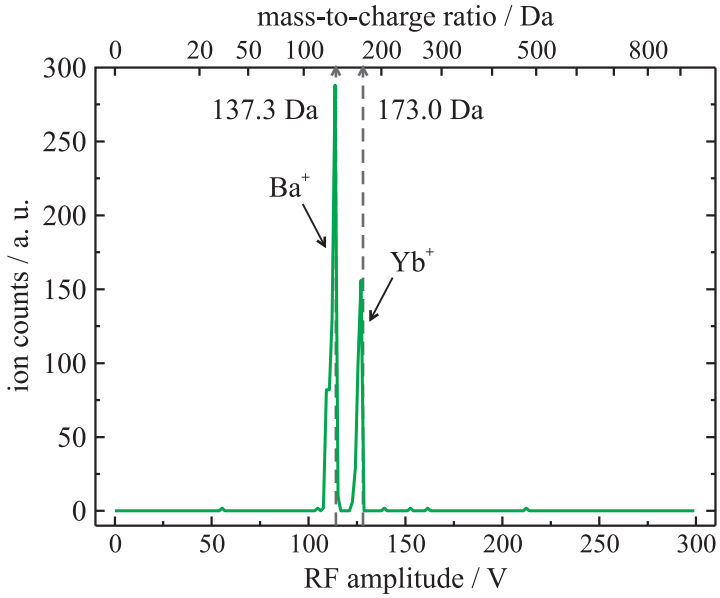

Figure 7.10: Ion extraction spectrum of a Ba^+/Yb^+ ion crystal. The upper mass-to-charge ratio axis is calibrated to the known mass of the Ba^+ ions of 137.3 Da. The Yb^+ peak well agrees with the Yb mass of 173.0 Da.

of too similar mass-to-charge ratios prevents the resolution of the single species' resonances without melting the ion crystal.

Concerning the ionization energies of Ba (5.21 eV) and Yb (6.25 eV), a charge exchange between Ba^+ ions and Yb neutrals should not be possible for Ba^+ ions in the electronic ground state $6^2S_{1/2}$. However, with Ba^+ ions in the excited state $6^2P_{1/2}$, i. e. after absorption of a cooling laser photon at 493 nm with an energy of 2.51 eV, charge exchange collisions are energetically possible. This has been proved and described above by exposing laser-cooled and hence excited $^{138}Ba^+$ ions to Yb vapor. Ba^+ ions in the metastable $5^2D_{3/2}$ state at an energy of 0.60 eV above the ground state should energetically not be capable of performing charge exchange collisions. But indeed, charge exchange has also been observed for ground state and metastable state Ba^+ ions with much lower rates.

To quantify this within the bounds of experimental possibilities, in total 34 ensembles of trapped Ba^+ ions in the three different electronic excitation states have been exposed to Yb vapor for different times between 10 s and 20 min. Every time the evaporation oven was heated up to an average measured temperature of 453 °C within a range of ±10 °C, which should not cause major differences in the Yb atom flux. After the exposure, the ion ensembles were analyzed via ion extraction and the amount of Ba^+ and Yb^+ ions was counted to determine the fraction of the initial Ba^+ ion number that charge exchanged with Yb atoms. To obtain comparable charge exchange rates, theses fractions were divided by the Yb exposure time. The averaged results for the three excitation states of Ba^+ are presented in Fig. 7.11 with error bars resulting from the statistical evaluation of the ion extraction spectra. With both the cooling and the repumping laser on and tuned to their resonances, the $^{138}Ba^+$ ions in the $6^2P_{1/2}$ state show a charge exchange rate of $(35.6\pm4.8)\,\%\mathrm{min}^{-1}$. With the repumping laser blocked, the charge exchange rate of $^{138}Ba^+$ ions in the metastable $5^2D_{3/2}$ state can be measured and is found to be about 19 times lower with $(1.9\pm0.6)\,\%\mathrm{min}^{-1}$. With both lasers blocked, a charge exchange rate of $^{138}Ba^+$ ions in the $6^2S_{1/2}$ ground state is hardly detectable and on the scale of the measurement uncertainty with $(0.6\pm0.6)\,\%\mathrm{min}^{-1}$.

As mentioned above, for Yb atoms with the ionization energy $E_{ion}(\mathrm{Yb}) = 6.25\mathrm{eV}$ and Ba^+

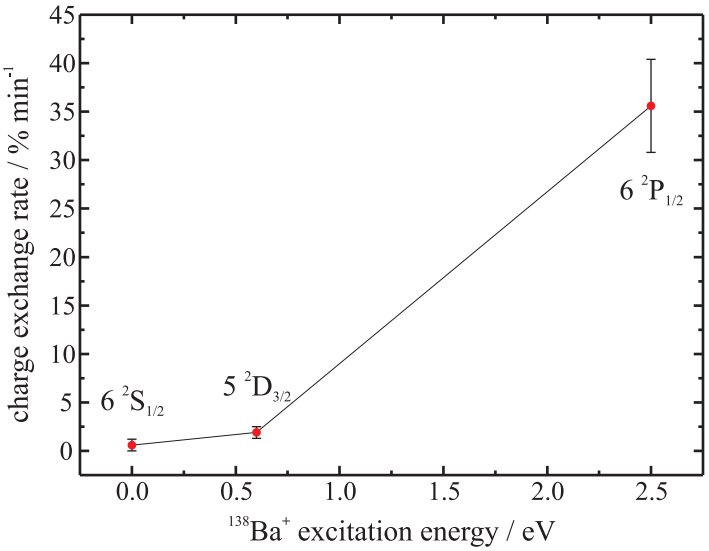

Figure 7.11: $^{138}Ba^+$ excitation state dependent charge exchange rate with Yb. Given are the fractions of the initial Ba^+ ion number that exchanged charge with neutral Yb atoms divided by the Yb exposure time. In total 34 ensemble of trapped Ba^+ ions in the three different excitation states $6^2S_{1/2}$, $5^2D_{3/2}$, and $6^2P_{1/2}$ were investigated and averaged.

ions with the electron affinity $E_{aff}(Ba^+) = -5.21$eV, an additional energy of $E_{ion}(Yb) + E_{aff}(Ba^+) = 1.04\,eV$ is required for a charge exchange collision between an Yb atom and a ground state Ba^+ ion. A Ba^+ ion in the metastable state has an excitation energy of 0.60 eV so that additional $1.04\,eV - 0.60\,eV = 0.44\,eV$ are required in this case. These missing energies can, for example, be contributed by Yb atoms with sufficiently high kinetic energies. In the Yb beam from the evaporation oven with the atoms at 453 ± 50 °C[1], the fraction of atoms with a kinetic energy higher than the required energy in the metastable state of 0.44 eV is about $0.7^{+0.4}_{-0.2}$ %, and the fraction with more than 1.04 eV required in the ground state is totally negligible with $1.0^{+1.8}_{-0.7} \cdot 10^{-4}$ % [79]. In the metastable state case, the measured charge exchange rate is $5.3^{+2.8}_{-2.1}$ % of that measured for the $6^2P_{1/2}$ state, in which all Ba^+ ions can charge exchange. Thus, the measured charge exchange rate in this case is about $\frac{5.3}{0.7} = 7.6$ times (or at least $\frac{5.3-2.1}{0.7+0.4} = 2.9$ times) higher than expected. As mentioned above, these collision experiments were not intended to give quantitative results and the control of the atom fluxes are not accurate, so that these deviations can in principle be explained by experimental imprecision. Another aspect not considered here, but which would lead to the higher charge exchange rates, are collisions involving a third particle, either a Ba^+ ion or an Yb atom. The same argumentation holds for the ground state case, where a not measurable charge exchange rate is expected when considering the distribution of the Yb atoms' kinetic energies alone.

7.3 Collisions of neutral atoms and trapped complex molecular ions

None of the investigated atomic species, neither the alkali metals Li, Na, K, Rb, and Cs, nor the rare earth metal Yb, is suitable to be applied for collisional cooling of molecular

[1]The large temperature range has been chosen as the exact temperature of the Yb atoms is unclear because only the oven temperature is measured and not the temperature of the Yb sample itself.

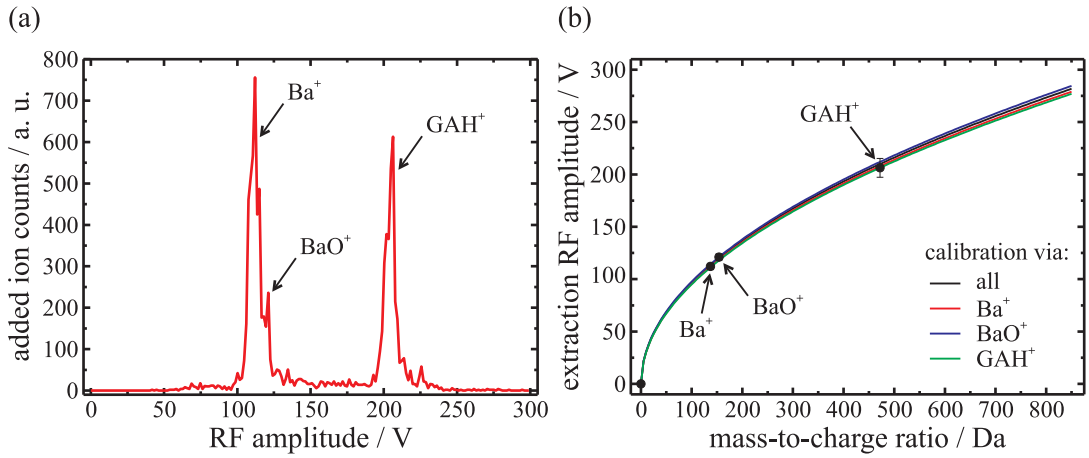

Figure 7.12: Identification of trapped ion species via ion extraction. (a) Ion extraction spectra of four identically prepared cold ion ensembles consisting of Ba^+ and GAH^+ ions and small amounts of BaO^+ added for averaging. (b) Theoretical dependence of the extraction RF voltage and the mass-to-charge ratio calibrated to the peaks from (a) for Ba^+ (red), BaO^+ (blue), and GAH^+ (green), as well as to an average of all (black). The dots are plotted at the measured extraction RF voltages from (a) and at the known mass-to-charge ratios, which are well confirmed in all calibration cases.

ions that are translationally cooled by laser-cooled Ba^+ ions. All species would exchange charge with the trapped Ba^+ ions causing a loss of the translational coolant. However, further investigations with these neutral atom species have been performed in order to test their interaction with trapped complex molecular ions. Both considered molecular species GAH^+ and ATH^+ (Tab. 5.1) are modified by collisions with neutral Yb atoms, but stay completely unchanged after collisions with the alkali atoms.

To avoid the laser-excited $^{138}Ba^+$ loss reactions with background gases, clouds of Ba^+ and GAH^+ ions have been exposed to Yb vapor without cooling lasers. When the vacuum pressure had reached normal values after such an Yb exposure, the trapped ion ensembles have been cooled down as far as possible (sometimes crystallization could not be achieved) and analyzed via ion extraction. Fig. 7.12(a) shows an ion extraction mass spectrum of reference ion ensembles, which have not been exposed to Yb vapor, consisting of Ba^+ and GAH^+ ions and small amounts of BaO^+. In this and several following cases, not only one ion extraction but many of identically prepared ion ensembles were acquired and added to average out effects of different ion numbers and to achieve a higher mass accuracy. Fig. 7.12(b) shows the dependence of the extraction RF amplitude and the mass-to-charge ratio $U_{RF}^{ex}(\frac{m}{Q})$ (see Eq. (4.1)) with different numerical calibration factors α according to the different known masses of Ba^+ (red), BaO^+ (blue), and GAH^+ (green), as well as to an average value of these (black). The black dots are plotted at the known mass-to-charge ratios of the ion species and the measured extraction RF amplitudes derived from the peaks in the ion extraction spectrum together with error bars following the width of the peaks. With all calibrations used, the measured values are well confirmed within their error bars, proving once more the suitability of the ion extraction method.

When non-cooled ion ensembles of Ba^+ and GAH^+ ions are exposed to Yb, two reactions can be observed: As described in Chapter 7.2.4, Yb atoms charge exchange with trapped Ba^+ ions and accumulate in the ion trap, even for Ba^+ ions in their electronical ground state. Moreover, Yb atoms stick to GAH^+ ions leading to the detection of species with masses of that of GAH^+ plus one or two Yb atoms. Fig. 7.13(a) shows again a composite

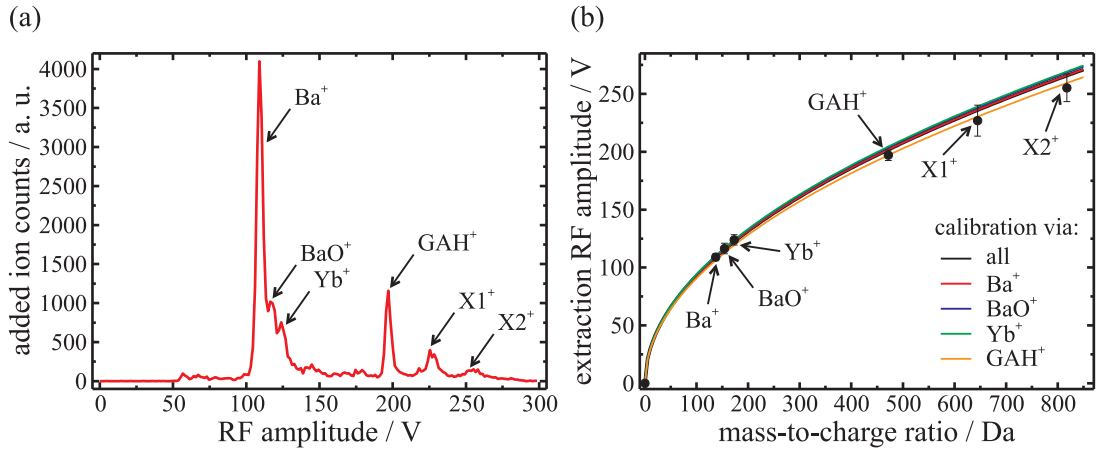

Figure 7.13: Identification of trapped ion species via ion extraction. (a) Composite ion extraction spectrum of in total 21 ion extraction spectra of similarly prepared ion ensembles added for averaging. In non-cooled ensembles of Ba^+ and GAH^+ ions (with small amounts of BaO^+) Yb atoms charge exchanged with trapped Ba^+ ions and attached to GAH^+ molecules forming the new molecular species $X1^+$ and $X2^+$. (b) Assuming the mass-to-charge ratios of GAH^+ plus one ($X1^+$) or two ($X2^+$) Yb atoms, the formation of such adducts is well confirmed by the differently calibrated theoretical curves of the extraction RF amplitude.

ion extraction spectrum achieved by adding in total 21 ion extraction spectra of similarly produced ion ensembles. Here, non-cooled clouds of Ba^+ and GAH^+ ions were exposed to Yb atoms from the evaporation oven at 410 to 420 °C for just a few seconds. Besides the usual peaks of Ba^+, BaO^+, Yb^+ and GAH^+ the ion extraction spectrum shows two additional peaks $X1^+$ and $X2^+$ with mass-to-charge ratios above that of GAH^+. Just as in Fig. 7.12(b), Fig. 7.13(b) shows the theoretical dependence of the extraction RF amplitude and the mass-to-charge ratio calibrated to the known masses of Ba^+ (red), BaO^+ (blue), Yb^+ (green), and GAH^+ (orange), as well as to an average of all (black). All curves well confirm the known species at their extraction RF amplitude (black dots). The unknown new species $X1^+$ and $X2^+$ are plotted at the measured extraction RF amplitudes and at the mass-to-charge ratios of a GAH^+ molecule with one ($X1^+$) or two ($X2^+$) Yb atoms attached. This assumption is well confirmed within the error bars for all calibration cases, but especially for the calibration with GAH^+. This might be due to the fact, that possible deviations from the square root dependence of $U_{RF}^{ex} \propto \sqrt{m/Q}$ appear less pronounced for a calibration with a more similar mass-to-charge ratio.

The same experiments on GAH^+ ions were performed with the alkali metals K, Rb, and Cs instead of Yb. Here, just the expected charge exchange reactions have been observed, but no modifications of the GAH^+ ions. The results of these experiments are illustrated in Fig. 7.14 and described in detail in the figure caption. In all cases, the GAH^+ peak in the ion extraction spectra appears unchanged although the occurrence of the corresponding alkali ion species accounts for the actual exposure of the ions to the alkali atoms. Note that in the case of Cs, the Cs^+ ions cannot be distinguished from the Ba^+ ions in the ion extraction spectra as described in Chapter 7.2.2 due to their too similar masses. But during the experiments a loss of Ba^+ ions was observed with the CCD camera, similar to the case shown in Fig. 7.5 which accounts for an exposure of the trapped ions to Cs atoms.

Collisions of neutral metal atoms as K, Rb, Cs, and Yb with trapped complex molecular ions represent a novel and uncommon field, which has not been explored so far, according to own literature research and to [80]. However, the fact that Yb atoms stick to the

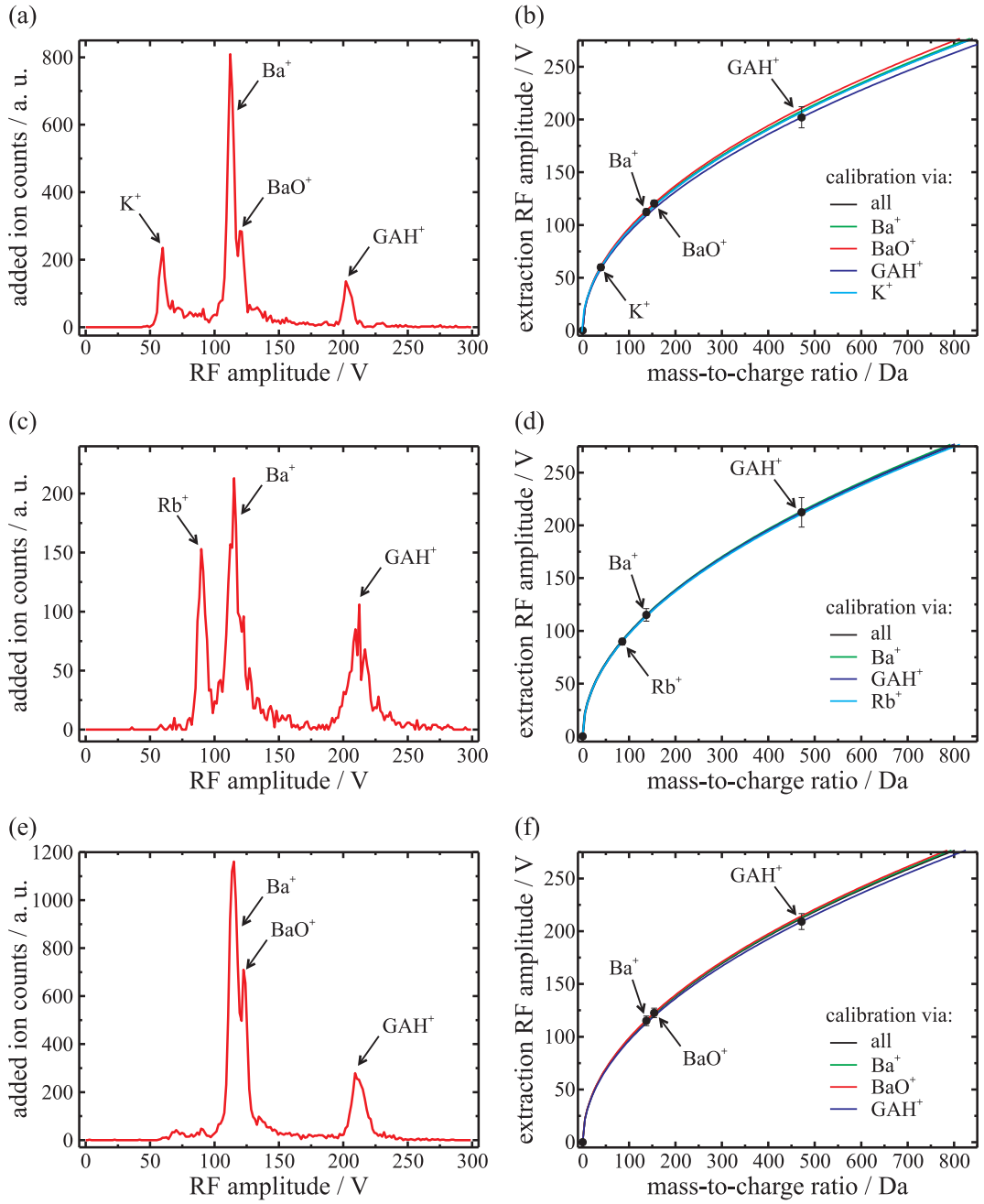

Figure 7.14: Identification of trapped ion species via ion extraction. The left column shows composite ion extraction spectra of similarly prepared ion ensembles added for averaging. Non-cooled ensembles of Ba^+ and GAH^+ ions (with small unavoidable amounts of BaO^+) were exposed to K atoms (a), Rb atoms (b), and Cs atoms (c), cooled down as far as possible after the exposure, and analyzed via ion extraction. In the first two cases, K^+ and Rb^+ ions were produced by charge exchange of the neutral atoms with the trapped Ba^+ ions as verified by their occurrence in the ion extraction spectra. The charge exchange of Cs atoms cannot be detected in this way due to the overlapping peaks of Cs^+ and Ba^+ ions as a result of their similar masses, but was observed with the CCD camera as described in Chapter 7.2.2. The GAH^+ peaks remained completely unchanged in all three cases, no adducts as with Yb were created with alkali atoms. The right column shows the dependence of the extraction RF amplitude and the mass-to-charge ratio calibrated to the species of known masses. All measured results (black dots) are well confirmed for all calibrations in each case.

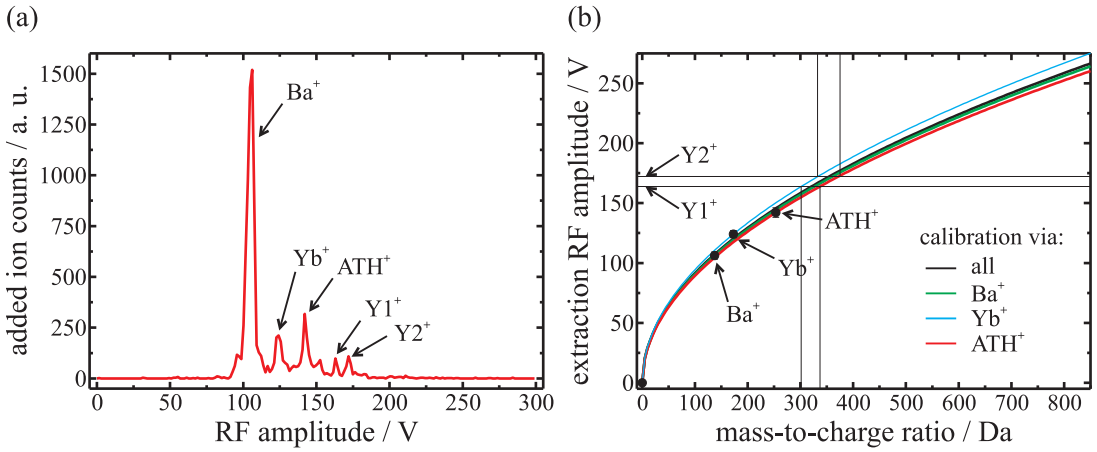

Figure 7.15: Identification of trapped ion species via ion extraction. (a) Composite ion extraction spectrum of in total eight ion extraction spectra of similarly prepared ion ensembles added for averaging. In non-cooled ensembles of Ba^+ and ATH^+ ions, Yb atoms exchanged charge with trapped Ba^+ ions leading to the accumulation of Yb^+ ions, and at least two new molecular species $Y1^+$ and $Y2^+$ were created. (b) The three species Ba^+, Yb^+, and ATH^+ are well confirmed by the theoretical dependence of $U_{RF}^{ex}(\frac{m}{Q})$. The masses of the new species $Y1^+$ and $Y2^+$ are too low to be adducts of Yb atoms and ATH^+ ions.

organic molecule GAH^+ and alkali atoms do not, can be explained by the high affinity of lanthanides to oxygen atoms and carboxylate derivates [81].

In order to explore if this is a general property of Yb atoms, the same experiments as described above have been performed with ions of the organic molecule alanine-tyrosine (ATH^+). The results of these experiments are less clear than in the case with GAH^+. However, the collisions of Yb atoms with ATH^+ ions lead to the creation of molecular species heavier than the parent ATH^+ ions as shown in Fig. 7.15(a). Here, eight non-cooled ensembles of Ba^+ and ATH^+ ions without BaO^+ have been exposed to Yb vapor from the evaporation oven operated at about 420 °C for a few seconds, cooled down after the exposure as far as possible, and analyzed via ion extraction. The composite ion extraction spectrum clearly shows, besides the usual Ba^+ peak, the peak of Yb^+ ions created by charge exchange reactions, and the ATH^+ peak, at least two peaks of the new and unknown species $Y1^+$ and $Y2^+$. According to the theoretical curves of $U_{RF}^{ex}(\frac{m}{Q})$ shown in Fig. 7.15(b), these species have mass-to-charge ratios in the range of about 300 to 330 Da ($Y1^+$) and 330 to 370 Da ($Y2^+$) depending on the considered ion species used for calibration. With respect to the masses of Yb (173.0 Da) and ATH^+ (253.3 Da), neither $Y1^+$ nor $Y2^+$ can be adducts of those two species as their mass-to-charge ratios are too small by at least 60 Da. Thus, the most likely explanation for these new species are adducts of fragments of ATH^+ that have been created during the exposure with Yb atoms, which either formed adducts with each other or with Yb atoms. For a more detailed analysis, the mass resolution of the available techniques is insufficient.

8 Theoretical studies on Coulomb crystallization

When the translational energy of a trapped ion ensemble is sufficiently reduced by laser cooling, a first-order phase transition from a liquid to a solid state occurs with the ion ensemble changing from a disordered ion cloud to an ordered ion crystal. This Coulomb crystallization usually comes along with a strong change in a thermodynamic potential of the observed system [51]. However, for smaller ion ensembles as considered in this work, these changes are much less pronounced as for infinite ones. So there is a need for an alternative approach to characterize the Coulomb crystallization of small ion ensembles.

Within this project, theoretical studies on the ion motion in such small ion ensembles at temperatures around this phase transition were performed using the simulation program *SOSC* that has been applied for the analysis of experimentally observed ion ensembles as described in the previous chapters. In a linear quadrupole trap, the ions arrange in shell structures which prevents a free diffusion in radial direction. Instead, the ions are constricted to the shells (Chapter 8.2) and can only move to neighboring shells, provided their kinetic energy is high enough to overcome the constricting potential barriers. In contrast to this radial ion motion between different shells, the ion motion within a shell, denoted as intrashell motion, is much less constricted by potential barriers. For ion temperatures above the Coulomb crystallization phase transition temperature, the intrashell ion motion changes from bound motion in local potential wells to a free, normal diffusion (Chapter 8.4).

The simulations have shown that intershell diffusion rates in the considered ion crystals increase exponentially when the ion temperatures exceed certain values that agree well with the predictions of other established models (Chapter 8.3). Ion ensembles of different ion numbers (300, 500, and 1000 $^{138}Ba^{+}$ ions) and different symmetries (prolate and spherical) have been investigated (Chapter 8.1) confirming a clear tendency for the phase transition temperatures (Chapter 8.5): The higher the ion number, the lower is the transition temperature [82].

8.1 Simulated ion ensembles

To investigate the Coulomb crystallization under realistic conditions, typical parameters of the ion trap used in this work have been applied in the simulations. An RF amplitude of $U_{RF} = 351.9\,\mathrm{V}$ and an endcap electrode voltage of $U_{EC} = 6.8\,\mathrm{V}$ yield a radial secular frequency for $^{138}Ba^{+}$ ions of $\nu_r = 91.8\,\mathrm{kHz}$ and an axial frequency of $\nu_z = 19.0\,\mathrm{kHz}$, i. e. a prolate crystal symmetry with $\nu_r/\nu_z \approx 5$ as shown in Fig. 8.1(a)-(c). To simplify the simulations and the interpretation of their results, ion ensembles consisting of $^{138}Ba^{+}$ ions only − without isotopes − have been considered. Ion numbers of 300, 500, and 1000 $^{138}Ba^{+}$ ions have been chosen, being typical on the one hand and still simulatable with acceptable computing times on the other hand.

Additionally, a spherical ion ensemble consisting of 500 ions (Fig. 8.1(d)) has been simulated to compare the ion dynamics with that of prolate crystals. Due to restrictions of

Ion number	Symmetry	Number of different heating rates	Temperature range / mK
300	prolate	24	0.7 - 32.9
500	prolate	20	0.8 - 12.5
1000	prolate	61	0.4 - 28.9
500	spherical	18	0.8 - 10.8

Table 8.1: Overview of investigated ion ensembles. The four different ion ensembles have been simulated with different heating rates leading to temperatures that cover the phase transition temperature.

parameter ranges in the simulation program, a spherical ensemble with $\nu_r/\nu_z = 1$ could only be realized with a shorter middle electrode length of 8.66 mm (compared to 20 mm in case of the ion trap used here). This leads to a stronger axial confinement, and with an RF amplitude of $U_{RF} = 349.9\,\mathrm{V}$ and an endcap electrode voltage of $U_{EC} = 20.0\,\mathrm{V}$ the resonance frequencies for $^{138}Ba^{+}$ ions are $\nu_r = \nu_z = 75.3\,\mathrm{kHz}$.

To analyze the ion motion, the coordinates of all ions for all simulation time steps have been recorded. Simulated time intervals were in the range of 1 to 10 ms, which leads to up to 25,000 coordinates recorded for each ion with simulation time steps of 400 ns. In all cases, a damping coefficient of $\beta = 1.74 \cdot 10^{-22}\,\mathrm{kg/s}$ has been applied and different temperatures were achieved by choosing different heating rates. As shown in Fig. 8.2, using the example of the prolate 500 ion ensemble, the ion temperature T depends linearly on the applied heating rate H. This dependence can be easily derived as follows: The heating rate $h = \mathrm{d}E/\mathrm{d}t$ according to Eq. (4.4) with $E = \frac{3}{2}k_BT$ yields the temperature increase rate

$$\left.\frac{\mathrm{d}T}{\mathrm{d}t}\right|_{\mathrm{heating}} = \frac{2}{3k_B}h \equiv H. \tag{8.1}$$

In thermal equilibrium, this temperature increase rate equals the temperature reduction rate from Eq. (4.3)

$$\left.\frac{\mathrm{d}T}{\mathrm{d}t}\right|_{\mathrm{cooling}} = -\frac{2}{3}\frac{\beta}{m}T,$$

leading to a linear relationship for the equilibrium temperature

$$T_{eq} = \frac{3}{2}\frac{m}{\beta}H. \tag{8.2}$$

Tab. 8.1 gives an overview of the four different ion ensembles concerning the simulated temperature ranges and the number of different heating rates applied in each case. Several ensembles have been simulated for several times with the same heating rate applied for statistical reasons or for different simulated time intervals. In total, a database with coordinates of more than 160 thermalized ion ensembles has been produced being the basis for the analysis of the ion motion presented in the following chapters.

8.2 Analysis of ion motion

At zero temperature, ions in a trap arrange in a spatial configuration of a minimum potential energy balancing the confining trap potential and the mutual Coulomb repulsion. Depending on the trap parameters, such an ion crystal shows a shell structure of either

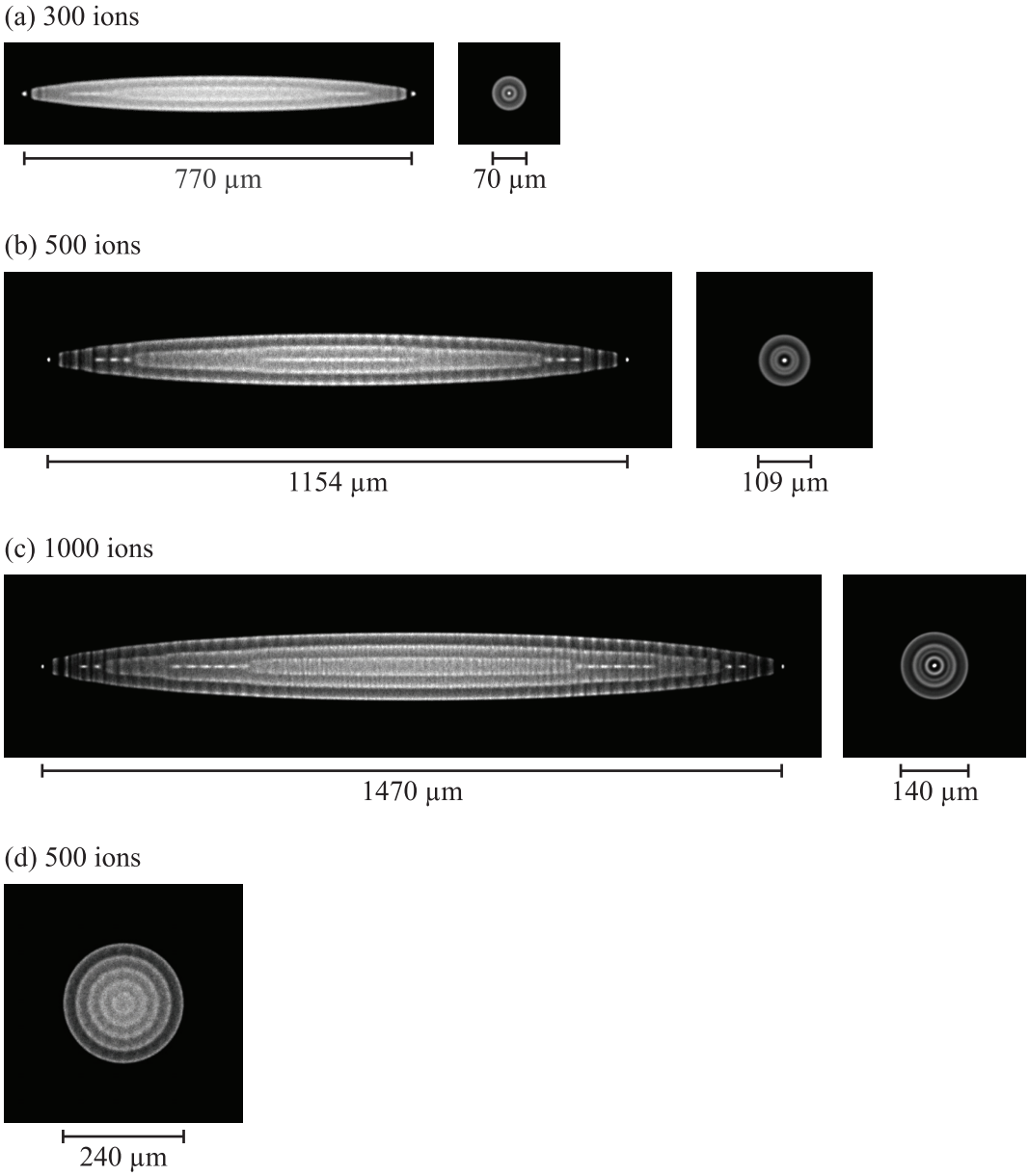

Figure 8.1: Overview of investigated ion ensembles. Simulated CCD images of the four different investigated ion ensembles drawn to scale. The figures (a) - (c) show the crystals of prolate symmetry in radial (left) and axial (right) view at arbitrarily chosen temperatures. Figure (d) shows the spherical ion crystal as appearing from any radial direction.

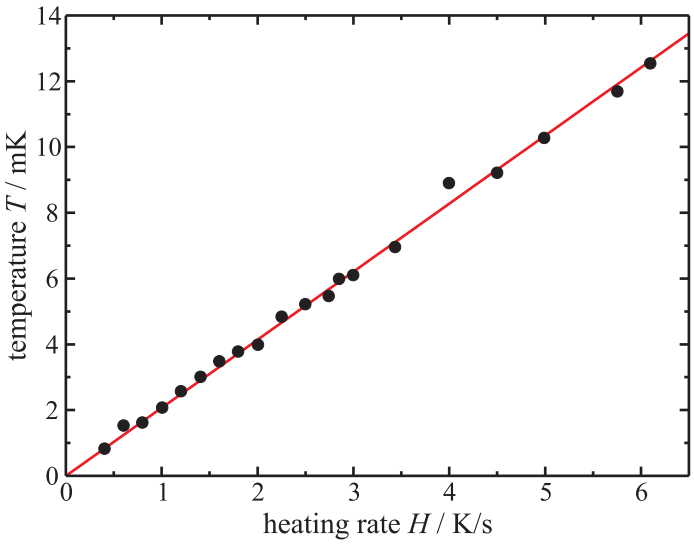

Figure 8.2: Ion temperature vs. heating rate. For the 500 ion ensemble in prolate symmetry, the plot shows the temperatures T reached for each of 20 different applied heating rates H (dots). The red line is a linear fit.

prolate or more spherical symmetry (see for example Fig. 8.1). In fact, the ions move around their equilibrium positions due to induced micromotion or secular kinetic energy. The higher their kinetic energy, i. e. their temperature, the more dynamic is the entire ion ensemble because an ion that leaves its equilibrium position causes all other ions to react and to arrange in a new configuration that provides a minimum potential energy.

Due to the shell structure, the ions cannot diffuse freely through an ion crystal. Leaving a shell and moving to a neighboring one, denoted as *intershell diffusion*, requires more kinetic energy to overcome radial potential barriers than the motion within a shell, denoted as *intrashell diffusion*. Thus, in prolate ion crystals the ion motion is different in axial and radial direction. Here, the axial and azimuthal intrashell motion is less restricted than the radial motion. The higher the ion temperature, the more ions move between the shells and the more the shell structure is washed out. Note that at temperatures above the Coulomb crystallization temperature, the shell structure is still clearly visible even for much higher temperatures. However, the term *ion crystal* is commonly used for ion ensembles that show some structure, in contrast to the term *ion cloud* which is used for ion ensembles that do not show an obvious structure or that are even not cooled at all.

In order to analyze the intershell diffusion behavior in prolate ion ensembles, the maximum radial motion range

$$\Delta r = r_{max} - r_{min} \tag{8.3}$$

is introduced with $r_{max}\,(r_{min})$ meaning the maximum (minimum) radial distance $r = \sqrt{x^2 + y^2}$ of an ion within a certain time interval Δt. Thus, when an ion stays within a shell during the time interval Δt, Δr is at most as large as the thickness of the shell. However, when the ion moves to the next shell or even further, Δr takes a value which is a multiple of the distance between two shells.

Fig. 8.3 shows histograms of the Δr values of all ions in a prolate 300 ion ensemble within a time interval of $\Delta t = 1\,\mathrm{ms}$. For a low temperature of $T = 2.39\,\mathrm{mK}$, which is far below the Coulomb crystallization, all ions stay within their shells and the motion of most ions spans a range of around $\Delta r = 6\,\mu\mathrm{m}$ (Fig. 8.3(a)). At a higher temperature of $T = 8.71\,\mathrm{mK}$, sligthly above the Coulomb crystallization temperature, the histogram

(c) shows the appearance of a second peak around $\Delta r = 35\,\mu$m. This has to be ascribed to ions that moved between shells in the considered time interval. The plot (d) shows the radial distance of ten ions arbitrarily selected from this ion ensemble. In comparison to plot (b) for the lower temperature, here the range of radial motion is up to twice as high for the ions that stay within their shell. Additionally, the kinetic energies are high enough to allow single ions to move to a neighboring shell (see light-green curve in (d) at $t = 0.6\,$ms). These tendencies increase with higher temperatures, until at a temperature of $T = 37.95\,$mK almost all ions move between the shells as shown in the histogram (g) and the plot (h).

In an ion crystal of spherical symmetry, the ion motion is the same in all directions. Here, the maximum motion range has to be defined in three dimensions as $\Delta r_{3D} = r_{3D,max} - r_{3D,min}$ with $r_{3D,max}$ ($r_{3D,min}$) meaning the maximum (minimum) radial distance $r_{3D} = \sqrt{x^2 + y^2 + z^2}$ of an ion within a certain time interval Δt. Fig. 8.4 shows histograms of the Δr_{3D} values of all ions in a spherical 500 ion ensemble for different temperatures T and time intervals Δt. The higher the temperature and the longer the time interval, the more ions diffuse between the shells and the more ions move further than only to the neighboring shell. As shown in Fig. 8.1(d), the spherical ion ensemble consists of five concentric shells. An ion in the outer shell, for example, can either stay in this shell or move to four other shells. Thus, it can contribute to five peaks in the histogram of the Δr_{3D} values. In the case $T = 10.81\,$mK and $\Delta t = 8\,$ms (Fig. 8.4) the ion temperature is so high, that only a few ions stay within their shells (peak around $\Delta r_{3D} = 20\,\mu$m) and the largest amount moves within four shells (peak around $\Delta r_{3D} = 90\,\mu$m). Some even move within all five shells (peak around $\Delta r_{3D} = 110\,\mu$m). Note that the maximum radial motion range Δr_{3D} (the same holds for Δr in the prolate ensembles) does not give any information how often the considered ion has moved to another shell, but only about the radial range. An ion that has moved between all five shells might have started in the most outer shell and stopped in the most inner shell, or it might have done this several times until it stopped in some middle shell − the resulting Δr_{3D} is the same.

As mentioned above in the context of prolate ion ensembles, the axial intrashell ion motion is not restricted to such an extent as the radial intershell motion. Within the shells and above the Coulomb crystallization temperature, the ions can diffuse more or less freely, though underlying the mutual Coulomb repulsion of all other ions, which is described in detail in Chapter 8.4. To directly demonstrate the difference between the radial and the axial ion motion, an equivalent maximum axial motion range $\Delta z = z_{max} - z_{min}$ with z_{max} (z_{min}) meaning the maximum (minimum) axial coordinate z of an ion within a certain time interval Δt is introduced. Fig. 8.5 shows histograms of the Δz values of all ions in a prolate 1000 ion ensemble together with the axial coordinate z of ten arbitrarily selected ions within a time interval of $\Delta t = 1\,$ms for different temperatures T. As expected, there is no such behavior in the axial motion as in the radial motion because the ion ensembles are not regularly structured along the axial direction. The distribution of the Δz values simply becomes wider and shifts to higher values for increasing ion temperatures.

8.3 Intershell ion motion

8.3.1 Intershell diffusion rates

In order to quantify the ions' intershell diffusion and to describe its temperature behavior, the histograms of the maximum radial motion ranges Δr (and Δr_{3D}) have been evaluated. As described in the previous chapter, these histograms show different peaks. The one around the lowest values corresponds to the ions that stay within their shell during the

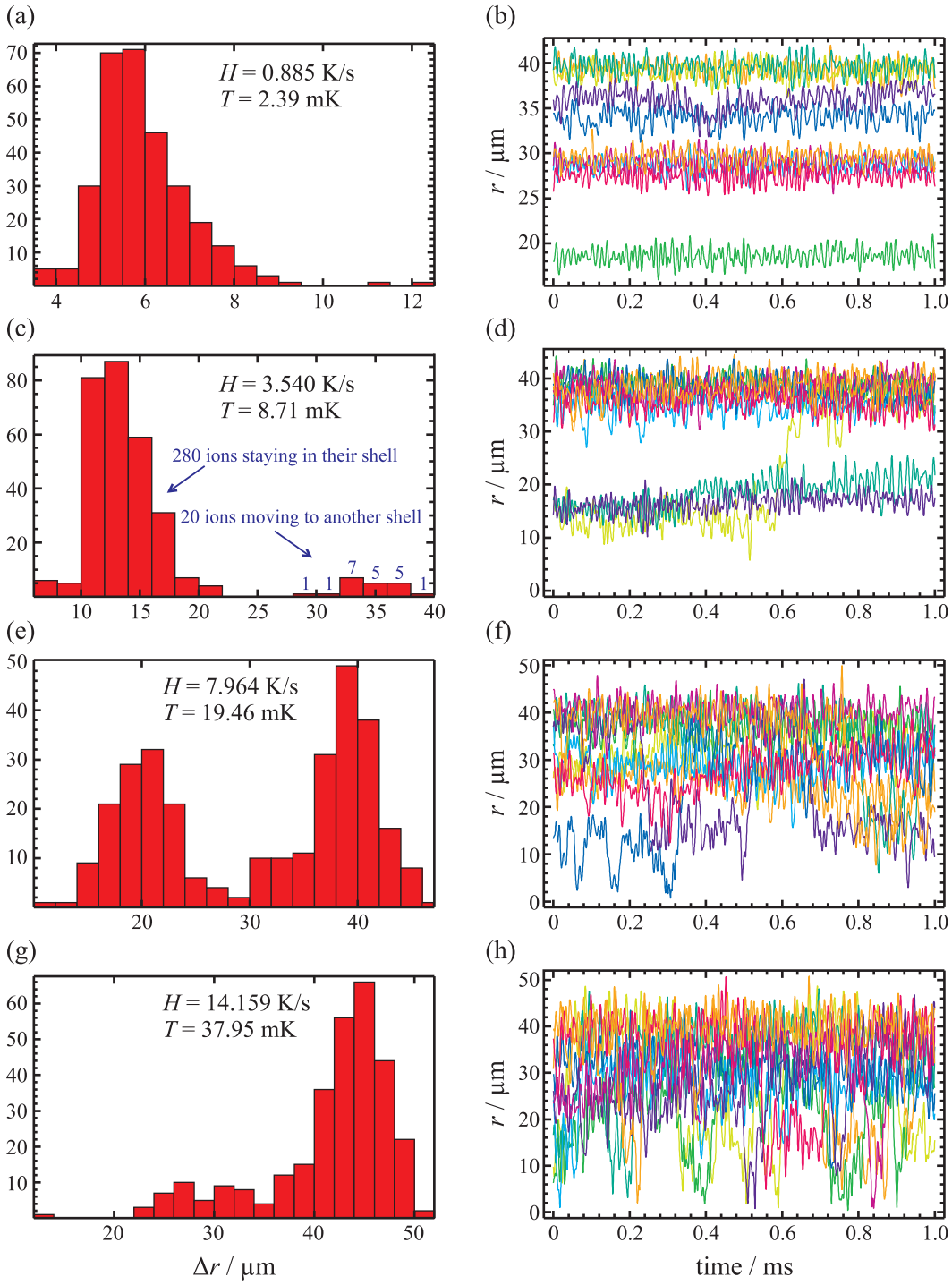

Figure 8.3: Radial motion in a prolate 300 ion ensemble. The left column shows histograms of the maximum radial motion range Δr for all ions in a prolate 300 ion ensemble for a time interval of $\Delta t = 1\,\mathrm{ms}$. The left peak has to be ascribed to ions that stay within their shell, the right peak to ions that move to the neighboring shell in the considered time interval. The higher the ion temperature T, the more ions move between shells. This is also illustrated in the plots in the right column that show the radial distance r of ten arbitrarily selected ions during the time interval.

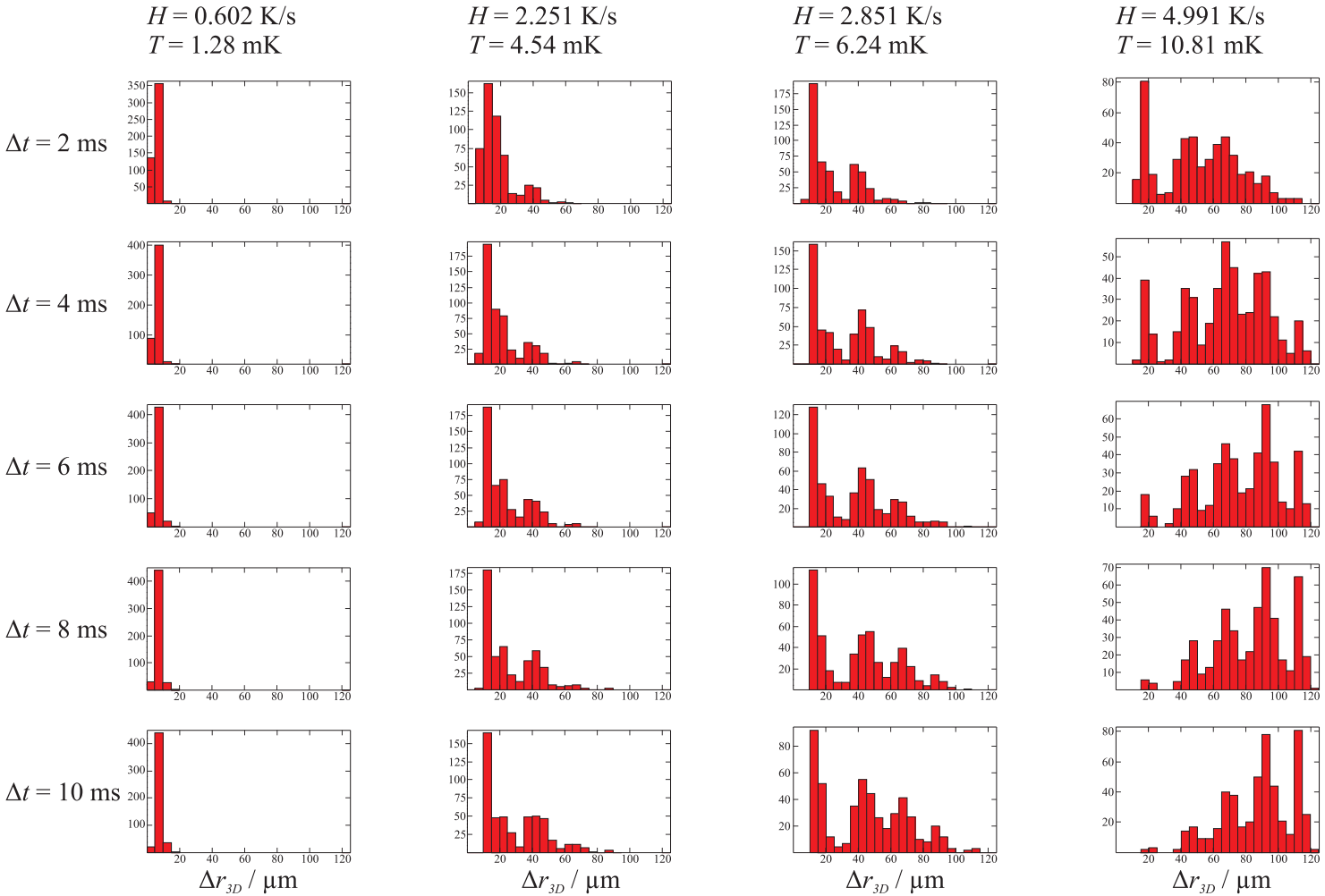

Figure 8.4: Radial motion in a spherical 500 ion ensemble. Shown are the histograms of the maximum radial motion range Δr_{3D} of all ions in a spherical 500 ion ensemble for different temperatures T and time intervals Δt. The higher the temperature and the longer the time interval, the more ions move between the shells and the more ions move further than only to the neighboring shell. (Note that the vertical axes are different as they are scaled to fit the histograms.)

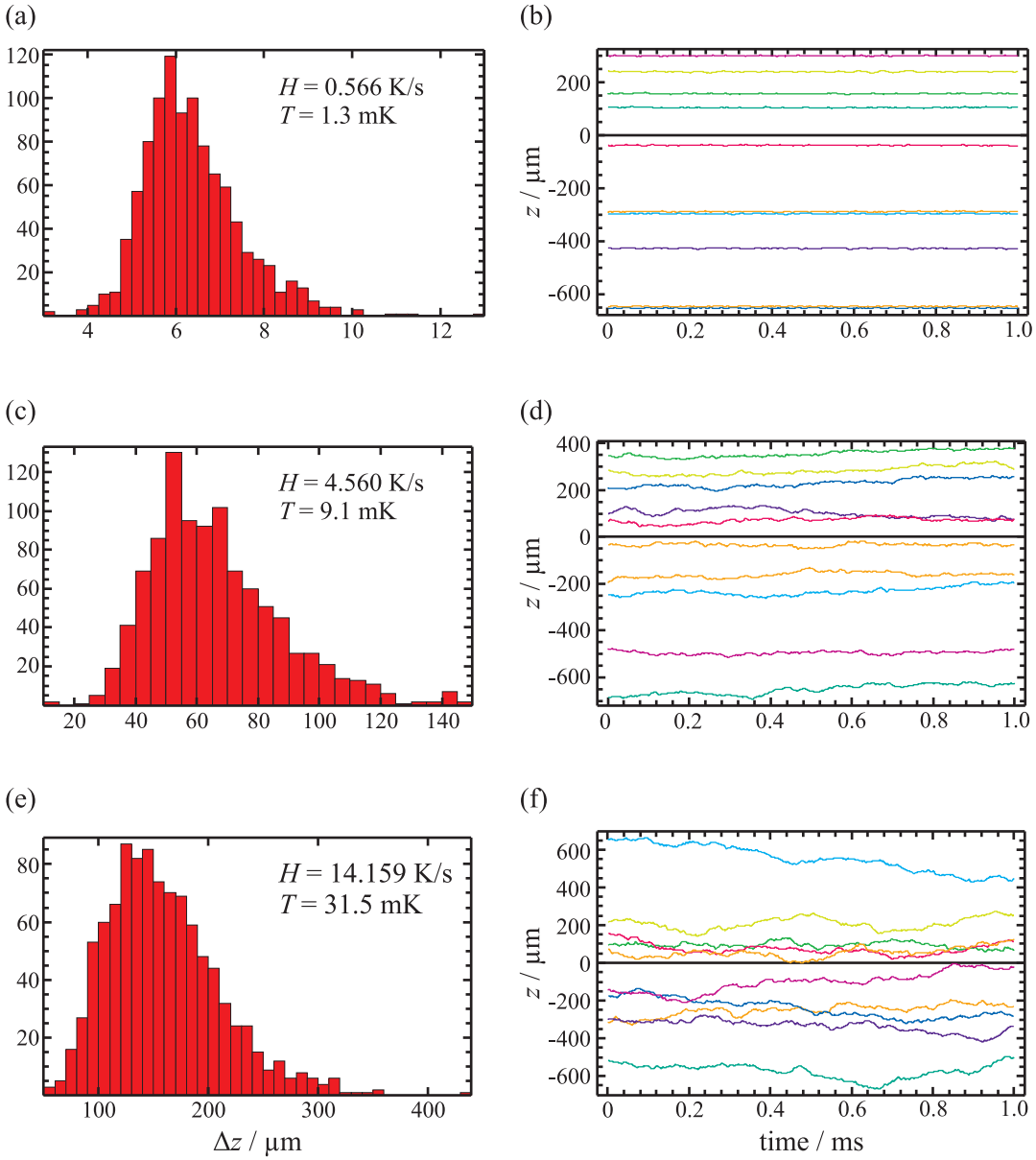

Figure 8.5: Axial motion in a prolate 1000 ion ensemble. The left column shows histograms of the maximum axial motion range Δz for all ions in a prolate 1000 ion ensemble for a time interval of $\Delta t = 1\,\mathrm{ms}$ for different temperatures. The distributions of the Δz values do not show separated peaks as in the radial case due to the lack of a regular structure in axial direction. This is also evident in the plots of the axial coordinate z of ten arbitrarily chosen ions shown in the right column.

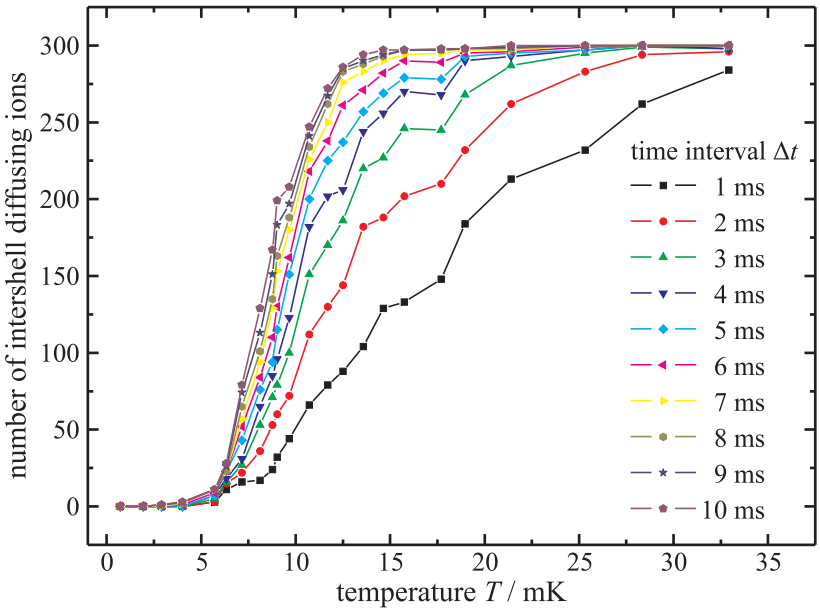

Figure 8.6: Number of intershell diffusing ions vs. temperature. For the prolate 300 ion ensemble the numbers of intershell diffusion ions within different time intervals Δt are shown for ion temperatures T in the range of 0.7 to 32.9 mK.

observed time interval Δt. All other peaks at higher values can be ascribed to ions that moved to other shells. Thus, adding up all columns of these peaks at higher values yields the number of ions that moved to other shells as illustrated in Fig. 8.3(c).

Fig. 8.6 shows the result of the histogram evaluation in case of the prolate 300 ion ensemble. Here, the black squares correspond to the histograms shown in Fig. 8.3 and give the number of intershell diffusing ions within a time interval of $\Delta t = 1\,\mathrm{ms}$ for temperatures in the range of 0.7 to 32.9 mK. In addition, the maximum radial motion ranges have also been determined and their histograms evaluated for longer time intervals of up to 10 ms. In the latter case (violet dots) the number of intershell diffusing ions strongly rises at a temperature of about 6 mK and completely saturates at about 15 mK. This means that at temperatures above 15 mK all ions move from shell to shell within the observed time interval of 10 ms, and that for temperatures below 6 mK the ions essentially stay in their shells, which represents the Coulomb crystallized state.

However, from the curves of the number of intershell diffusing ions depending on the temperature, no phase transition temperature can be determined as it would depend on the observed time interval (the shorter the time interval, the higher the derived phase transition temperature). Therefore, the temperature dependent intershell diffusion rate $k(T)$ is introduced. In plots of the number of intershell diffusing ions versus the time interval Δt, the intershell diffusion rate can be determined as the gradient of the initially linear slope of the saturating curves. Such plots are shown in Fig. 8.7 for the prolate 300 ion ensemble. Here, additional data points had to be acquired for ion ensembles of higher temperatures in order to cover the steep linear slope sufficiently accurate.

For all investigated ion ensembles and for all simulated temperatures, the intershell diffusion rates $k(T)$ have been determined in this way. In order to compare the rates of different ion ensembles, they have been divided by the ion number N of the associated ion ensemble to yield the relative intershell diffusion rates $k_{rel}(T) = k(T)/N$. Fig. 8.8 compares these relative rates for the prolate ion ensembles consisting of 300, 500, and 1000 ions (a) and for the prolate and spherical 500 ion ensemble (b). The rates increase with the temperature

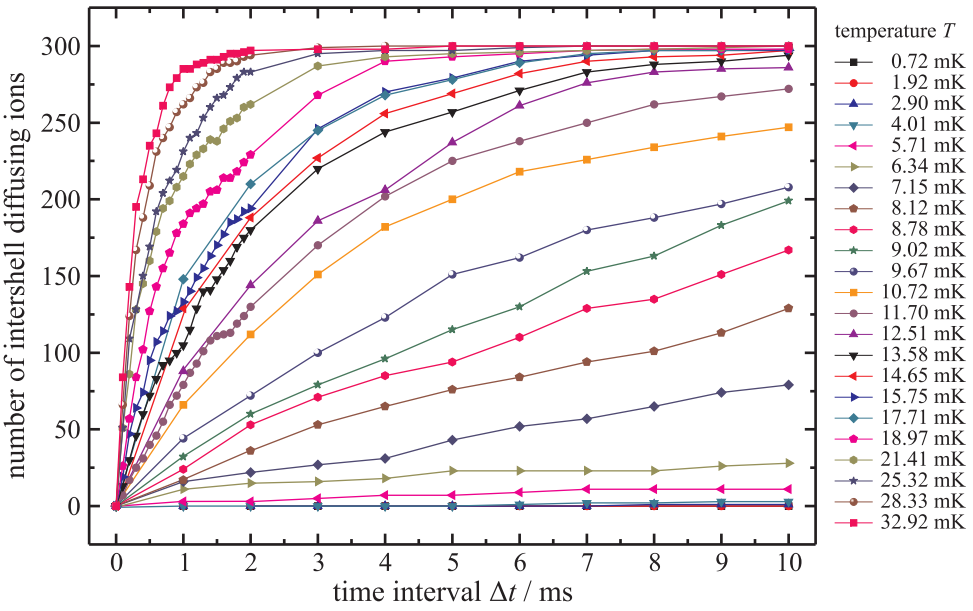

Figure 8.7: Intershell diffusing ions vs. time. Transposed representation of the data shown in Fig. 8.6 showing the number of intershell diffusing ions at different temperatures T for different time intervals Δt. Additional data points for ion ensembles of higher temperatures are included in order to enable a determination of the gradients of the initially linear slopes.

T and follow the equation

$$k_{rel}(T) = k_0 \exp\left(-\frac{T_0}{T}\right) \tag{8.4}$$

which is used as fit function in the plots with the fit parameters k_0 and T_0 described in the following paragraphs.

Two tendencies can be observed: In larger ion ensembles the intershell diffusion rates start increasing significantly at lower temperatures. In other words, larger ion crystals melt at lower temperatures. For ion ensembles of the same ion number but different symmetry, the more spherical ion ensembles seem to melt at lower temperatures. However, these plots do not yield well-defined phase transition temperatures, because this requires a definition of some threshold as treated in Chapter 8.5.

8.3.2 Potential barriers

The relative intershell diffusion rates following the temperature behavior of Eq. (8.4) well agree with the Arrhenius law, which describes the temperature dependence of thermally induced reactions and processes, such as diffusion or chemical reactions [83]. Treating Eq. (8.4) as an Arrhenius equation, k_0 represents the so-called pre-exponential factor and T_0 the activation temperature. Applied to chemical reactions, k_0 would correspond to a total rate of collisions leading to a reaction or not, and $E_0 = RT_0$ with the universal gas constant R would be the molar activation energy of that chemical reaction. In this case of intershell diffusing ions, with T_0 an average potential energy $k_B T_0$ can be associated, which the ions need to overcome when moving to a neighboring shell. The parameter k_0

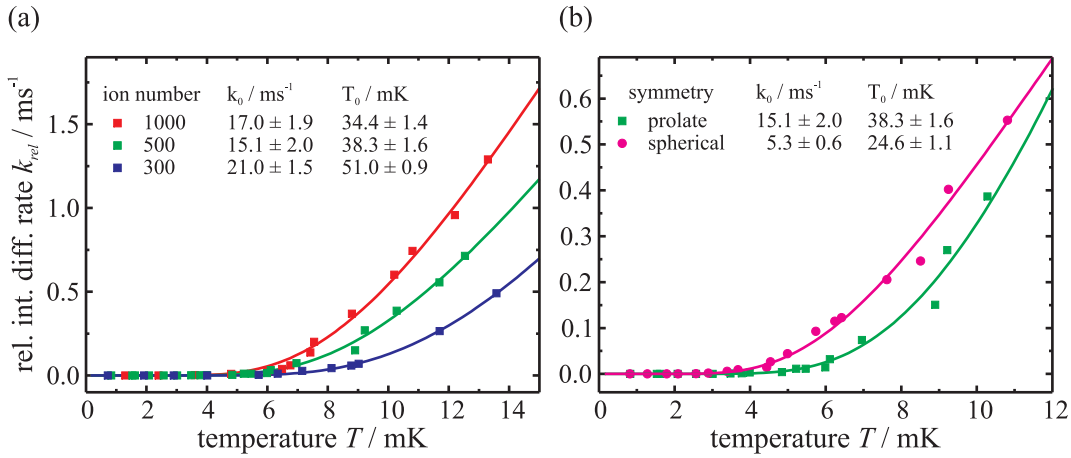

Figure 8.8: Relative intershell diffusion rates. The relative intershell diffusion rates k_{rel} describe the fraction of ions in an ion ensemble that move between the shells per time. They show an exponential behavior described by Eq. (8.4) used as fit function in these plots. In (a) the relative intershell diffusion rates are compared for the prolate ion ensembles consisting of 300 (blue), 500 (green), and 1000 (red) ions, and in (b) for the prolate (green) and spherical (pink) 500 ion ensemble.

can be interpreted as an average oscillation frequency in the local radial potential minima of the shells as described in the following paragraphs.

In order to investigate the potential barriers that ions have to overcome when moving to neighboring shells, simulations have been performed in which the total potential energies U_{tot} of an ion ensemble were calculated, when an additional test ion moves along a radial direction through the shell structure. Therefore, the test ion (same species as the other ions) was fixed at positions along a radial path through the ensemble, at which the ion ensemble was given the time to equilibrate with a high damping coefficient of $\beta = 80 \cdot 10^{-22}\,\mathrm{kg/s}$ in order to quickly arrange in that ion configuration which exhibits the lowest total potential energy. The total potential energy U_{tot} is the sum of the potential energies in the trap's pseudo potential Φ_{ps} (Eq. (2.14)) of all ensemble ions and the test ion, and the Coulomb potential energies of all ions including the test ion,

$$U_{tot} = \sum_{i=1}^{N} Q \cdot \Phi_{ps}(\mathbf{r}_i) + Q \cdot \Phi_{ps}(\mathbf{r}_{test}) + \frac{Q^2}{4\pi\epsilon_0} \sum_{i=1}^{N} \sum_{j=i+1}^{N} \frac{1}{r_{ij}} + \frac{Q^2}{4\pi\epsilon_0} \sum_{i=1}^{N} \frac{1}{r_{i,test}}, \tag{8.5}$$

where Q is the common charge of the ensemble ions and the test ion, $\mathbf{r}_i$ are the positions of the N ensemble ions, $\mathbf{r}_{test}$ is the position of the test ion, r_{ij} is the distance of the ensemble ions i and j, and $r_{i,test}$ is the distance of the ensemble ion i and the test ion.

Fig. 8.9 shows the equilibrium total potential energies U_{tot} of a prolate 500 ion ensemble, with the test ion at increasing radial distances r_{test} from the trap axis. In this case, the axial coordinate of the test ion was set close to the ensemble middle to $z_{test} = 26\,\mu\mathrm{m}$, because the test ion's start position $\mathbf{r}_{test} = (0\,\mu\mathrm{m}, 0\,\mu\mathrm{m}, 26\,\mu\mathrm{m})$ corresponds to a position where an ion would arrange in an ion ensemble consisting of 501 ions. The gray columns in Fig. 8.9 show the radial distribution of the 123 ions in a 200 µm long slice of the ion ensemble centered around the fixed test ion's axial coordinate selected for a clearer illustration.

As expected, U_{tot} shows local minima when the test ion is situated in a shell or the inner

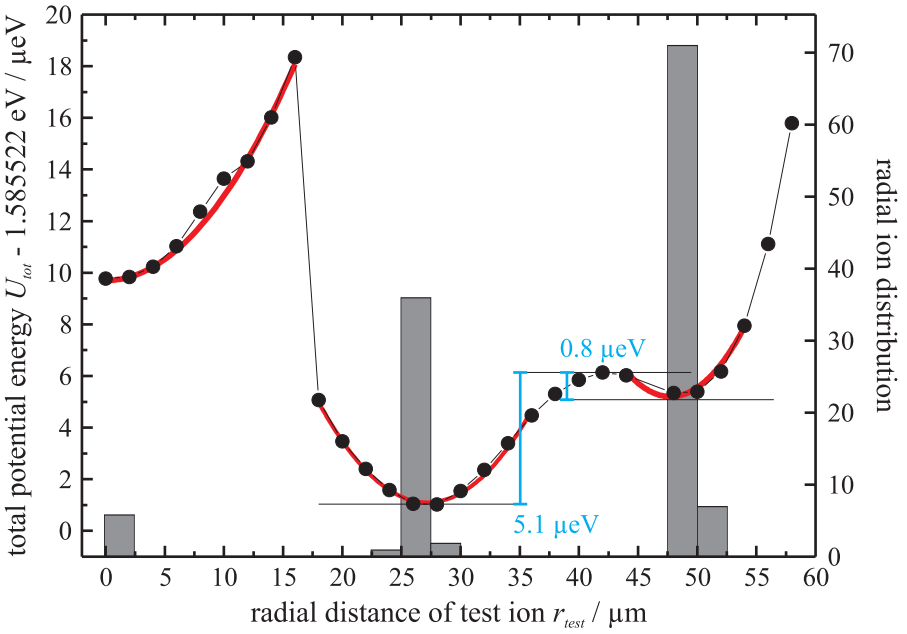

Figure 8.9: Potential barriers for intershell ion motion. In a prolate 500 ion ensemble, a fixed test ion of the same species is placed at increasing radial distances r_{test} from the trap axis. The ions arrange in configurations that yield the lowest possible total potential energy. For the test ion at radial distances with a high ion density (gray columns) the total potential energy shows local minima. The red curves are parabolic fits to these local potential wells.

ion string (see as well Fig. 8.1(b)), because the arrangement of the ions in a shell structure represents a state of lowest potential energy. Most of the intershell ion motion happens between the inner shell at $r = 27\,\mu$m and the outer shell at $r = 48\,\mu$m, as the potential barrier towards the inner ion string at $r = 0\,\mu$m is very large. Thus, the average potential barrier that intershell moving ions need to overcome, is the mean of the depths of the potential wells, which is 3.0 µeV at this axial coordinate. Indeed, this is very close to the potential barrier derived from the Arrhenius fits to the relative intershell diffusion rates (Fig. 8.8), which is $k_B(38.3\,\text{mK}) = 3.3\,\mu$eV in the case of the prolate 500 ion ensemble.

A special feature in the case of the prolate 500 ion ensemble is the presence of an inner ion string along the trap axis which consists of nine ions only. When an ion leaves the string, an ion, most probably from the inner shell, will promptly move to the trap axis in order to reconstruct the arrangement of lowest potential energy. In case of the fixed test ion, which is moved away from the trap axis step by step, the total potential energy grows until an ion from the inner shell jumps to the trap axis leading to a sudden strong decrease of the total potential energy, as shown in Fig. 8.9 at $r_{test} = 16\,\mu$m. In ion ensembles without an inner ion string consisting of a low number of ions, such large and sudden energy changes do not occur, as they average among the larger number of ions present in the shells, similar to the smooth change of the potential energy between the shells in this case of the prolate 500 ion ensemble.

The local potential minima radially centered in the inner ion string, the inner and the outer shell can be regarded as parabolic potential wells in which the ions oscillate with the frequency ν_{pot}. In a simple model, an average of these oscillation frequencies weighted according to the number of ions in the corresponding shell can be interpreted as the parameter k_0 from the Arrhenius fits to the relative intershell diffusion rates (Fig. 8.8). Fits to the potential wells have been performed with the function

$$U_{pot}(r_{test}) = \frac{a}{2}(r_{test} - r_{test,0})^2 + U_{pot,0} \tag{8.6}$$

in order to derive the harmonic oscillator frequencies $\nu_{pot} = \sqrt{\frac{a}{m}}$, where a is a fit parameter and m the ion mass. In the case of the prolate 500 ion ensemble with the test ion at $z = 26\,\mu$m, the oscillation frequencies $\nu_{pot}(r = 0\,\mu\text{m}) = 34.0\,$kHz, $\nu_{pot}(r = 27\,\mu\text{m}) = 40.3\,$kHz , and $\nu_{pot}(r = 48\,\mu\text{m}) = 49.5\,$kHz are obtained. The weighted average of these frequencies according to the ion distribution around this axial coordinate gives the value $k_0 = 45.9\,$kHz which is about three times higher than the value of k_0 obtained from the Arrhenius fit (see Tab. 8.2). A detailed discussion about this deviation is given in the end of this section.

Such simulations of the total potential energy using the method of a fixed test ion have been performed for all investigated ion ensembles. The data have been analyzed as described above and the derived results for k_0 and k_BT_0 are summarized in Tab. 8.2. While the values for the potential barriers k_BT_0 agree quite well with those obtained from the Arrhenius fits to the relative intrashell diffusion rates, the values for the frequency k_0 obtained with the test ion method are significantly higher. Especially in the case of the spherical 500 ion ensemble the values for both k_0 and k_BT_0 differ strongly, which is not understood so far and which requires further investigation.

ion number	symmetry	k_0/ kHz		k_BT_0 / µeV	
		rate fit	test ion	rate fit	test ion
300	prolate	21.0	48.9	4.4	4.7
500	prolate	15.1	45.9	3.3	3.0
1000	prolate	17.0	29.1	3.0	4.4
500	spherical	5.3	100.6	2.1	41.0

Table 8.2: Summary and comparison. Results for the oscillations frequency k_0 and the potential barrier k_BT_0 derived from the Arrhenius fits to the relative intershell diffusion rates (rate fit) and the simulations using the method of the fixed test ion (test ion).

The reason for these deviations is most probably the fact that the values of k_0 and k_BT_0 derived with the test ion method do not represent the situation of the whole ion ensemble. Here, the test ion is moved in one radial direction at a certain axial coordinate z, so that the presented results are, strictly speaking, only valid for this specific case, although they can be used for an approximate description. In contrast, the values derived from the Arrhenius fits represent average values, which hardly can be obtained by the test ion simulations. It is a part of ongoing work within this project, to achieve a better agreement for the values of k_0 and k_BT_0 via a more detailed analysis. Therefore, total potential energy curves for the test ion at numerous axial coordinates covering the whole ensemble length will be calculated and evaluated in order to average the depths of the potential wells and their oscillations frequencies in a suitable way. Additionally, such simulations will be performed at higher ion temperatures (in contrast to the simulations performed so far at $T \approx 0\,$mK) to have more realistic conditions. However, due to the less sharp shell structures at higher temperatures, the results will suffer from more scattering so that strong averaging will be required.

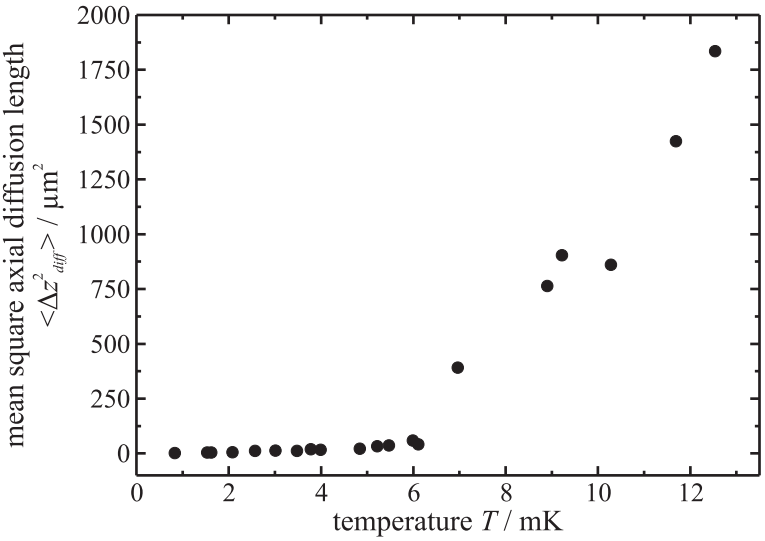

Figure 8.10: Axial intrashell diffusion. For a homogeneous sub-ensemble of a prolate 500 ion ensemble (see text for details), the mean square axial diffusion length $< \Delta z^2_{diff} >$ is shown for different temperatures, representing the sub-ensemble average of the ions' axial displacement within a time interval of $\Delta t = 0.5\,\mathrm{ms}$.

8.4 Intrashell ion motion

As described above, the radial intershell ion motion is subjected to potential barriers arising from the ions' arrangement in shells, which are still present for temperatures of up to 100 mK and therefore far above the Coulomb crystallization phase transition. However, for the axial intrashell ion motion, simulations have shown that this motion is almost free for temperatures above the phase transition, and that it can be described as normal diffusion.

For the investigation of the axial intrashell ion motion, a homogeneous sub-ensemble of the prolate 500 ion ensemble was chosen. It consists of the ions in the outer shell ($44\,\mu\mathrm{m} < r_i < 54\,\mu\mathrm{m}$) within an axial range of 300 µm centered around the ensemble middle ($-150\,\mu\mathrm{m} < z_i < 150\,\mu\mathrm{m}$). Depending on the temperature of the ion ensemble and the width of the considered diffusion time interval Δt, this selection comprises a varying number M of ions ranging from about 60 to 110. This is due to the fact that only ions are considered, whose diffusion paths lie within the spatial range denoted above, in order to ensure similar conditions for all considered ions. As quantity for the axial intrashell diffusion of the ions, the mean square axial diffusion length

$$< \Delta z^2_{diff} >= \frac{1}{M} \sum_{i=1}^{M} (z_i(t = \Delta t) - z_i(t = 0))^2 \tag{8.7}$$

is introduced, which represents the sub-ensemble average of the ions' squared axial displacement within the time interval Δt. Fig. 8.10 shows this mean square axial diffusion length $< \Delta z^2_{diff} >$ of the observed sub-ensemble for a time interval of $\Delta t = 0.5\,\mathrm{ms}$ for different temperatures. Here, at temperatures below $\sim 6\,\mathrm{mK}$, the ions are localized in individual local potential wells and oscillate around these equilibrium positions showing axial diffusion in a range of less than 8 µm and just a low linear increase with rising temperatures. For temperatures above $\sim 6\,\mathrm{mK}$, the ions are no longer bound and can freely diffuse in axial directions, with the axial diffusion lengths showing an abrupt rise with increasing temperatures.

In the case of normal diffusion described by Fick's law, the ensemble average of the squared displacements within the time interval Δt is proportional to Δt and characterized by the relation

$$< \Delta z_{diff}^2 >= 2D \cdot \Delta t, \tag{8.8}$$

where D is the diffusion coefficient [84].

Fig. 8.11(a) shows the mean square axial diffusion length $< \Delta z_{diff}^2 >$ for increasing time intervals Δt and for different ion temperatures T in case of the considered sub-ensemble of the prolate 500 ions ensemble. The values of $< \Delta z_{diff}^2 >$ seem to increase linearly with Δt, as expected for normal diffusion. Scattering arises for higher temperatures and larger values of Δt, because the number of considered ions is lower in these cases as described above. Linear fits to the curves $< \Delta z_{diff}^2 > (\Delta t)$ according to Eq. (8.8) yield the diffusion coefficients $D(T)$ which are plotted in Fig. 8.11(b). For temperatures below $\sim 6\,\mathrm{mK}$ the diffusion coefficient is negligibly low, and at $\sim 6\,\mathrm{mK}$ it abruptly rises, initially linearly with increasing temperatures. In gases the diffusion coefficient shows a square root dependence of the temperature [85], which cannot be proved in this case due to a lack of data points at higher temperatures. However, our results agree very well with diffusion coefficients found for other cases of non-neutral plasmas. Dubin and O'Neil [86] analyzed the diffusion of similar sized clouds of $^9Be^+$ ions in Penning traps. For comparable temperatures they found diffusion coefficients between 1000 to 10,000 $\mu m^2/ms$ which are of the same order of magnitude as our values (compare Fig. 8.8(b)).

Additional investigations with the fixed test ion method presented in Chapter 8.3.2 have been performed, in order to analyze the behavior of the total potential energy along intrashell ion paths. Two cases have been studied using again the example of the prolate 500 ion ensemble: the total potential energy for the fixed ion on a path in the outer shell along *axial* direction (see inset of Fig. 8.12(a)) and along *azimuthal* direction (see inset of Fig. 8.12(b)).

Fig. 8.12(a) shows the total potential energies U_{pot} for different axial positions z of the fixed test ions within the outer shell of the ion ensemble. As the simulations were performed with a very high damping coefficient resulting in ion temperatures of $T \approx 0\,\mathrm{mK}$, the ion ensemble does not only show the well known radial shell structure, but as well an axial structure looking like slices as shown in the inset image of the plot. In this simulated CCD image of 10 ms exposure time, the temperature is slightly higher at $T \approx 1\,\mathrm{mK}$ in order to make the ions move to reveal the shell and slice structure (otherwise the ions would appear as single dots). This weak axial slice structure leads to variations of the total potential energy on the order of a few micro-electron volts, when the fixed test ion is moved axially through the shell. At higher temperatures these potential variations will wash out allowing for a free diffusion in axial direction.

The total potential energies U_{pot} for different azimuthal angles α of the fixed test ion within the outer shell of the ion ensemble given in Fig. 8.12(b) do not show any significant change and fluctuate with a standard deviation of 43 neV. These fluctuations are on the order of the precision of our numerical calculations, so the total potential energy can be regarded as constant. When the fixed test ion is moved to another azimuthal position in the outer shell, the whole ion ensemble is expected to re-arrange to an ion configuration which yields the lowest possible total potential energy with this fixed ion. As the ion ensemble and the trap potential are rotational symmetric relative to the trap axis, the easiest way for the ion ensemble to achieve this goal is to rotate around the trap axis by the angle the test ion has been moved. Thus, the total potential energy does not change at all. In order to study the potential barriers the ions are subjected to when moving azimuthally within a

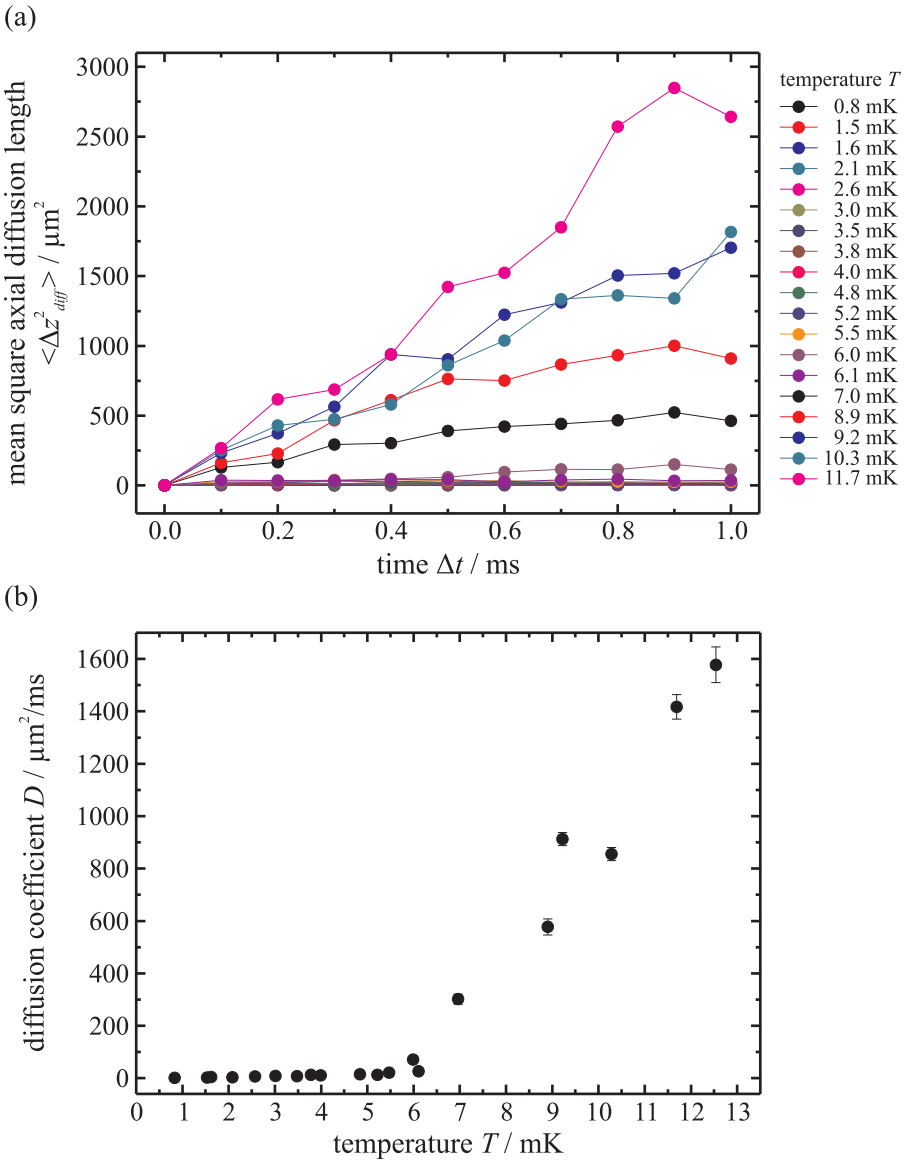

Figure 8.11: Normal diffusion in axial direction within a shell. (a) The mean square axial intrashell diffusion length $< \Delta z^2_{diff} >$is plotted for increasing time intervals Δt and different ion temperatures T, and found to be proportional to Δt as expected for the case of normal diffusion. (b) Here, the diffusion coefficients $D(T)$ obtained from linear fits to the curves $< \Delta z^2_{diff} > (\Delta t)$ shown in (a) are plotted, showing an abrupt rise for temperatures above $\sim 6\,\mathrm{mK}$.

shell, the simulation program would need to be changed so that such a collective rotation of all ions is forbidden.

8.5 Phase transition temperatures

Basically, there are two ways to theoretically investigate the Coulomb crystallization phase transition in non-neutral plasmas – analytical approaches and numerical simulations. Coulomb crystallization is a first-order phase transition, at which the first derivative of the system's free energy versus temperature shows a local maximum, and the free energy of the phases above and below the transition temperature are equal. Thus, the free energy is often analyzed in thermodynamic approaches, analytically as well as numerically, to determine the liquid-solid phase transition temperature in infinite and large non-neutral plasmas. Generally, the phase transition temperature T is given in an inverse form as the plasma coupling parameter Γ which was introduced in Chapter 2.3 in Eq. (2.29) as

$$\Gamma = \frac{Q^2}{4\pi\epsilon_0 a_{WS}} \frac{1}{k_B T}.$$

In an infinite, homogeneous one-component plasma, a transition from a fluid to a bcc crystalline phase is observed for $\Gamma = 174$, where the Gibbs free energies of these two phases are equal as derived from analytical models [51].

Other thermodynamic approaches use numerical methods, such as in [82], where among other aspects the specific heat of differently sized spherical ion ensembles is investigated. While characteristic changes in thermodynamic potentials at the phase transition are very distinct for infinite and large systems, they are much weaker for small systems. The increase of the specific heat investigated in the above mentioned case, for example, is more than a magnitude higher for an ion ensemble consisting of 10,000 ions compared to an ensemble consisting of 100 ions. Thus, for ion ensembles with ion numbers as considered experimentally in this work (< 1000), thermodynamic considerations are less suitable to investigate the Coulomb crystallization.

Numerical simulations of ion ensembles considering the ions' motion have been performed to investigate this phase transition in smaller systems. For example, Donkó et al. [87] studied strongly coupled one-component plasmas consisting of 1024 particles that are characterized by a localization ("caging") of the particles, trapped and oscillating in slowly fluctuating local potential wells. They introduce a caging time τ during which half of a particle's original surrounding neighbors stay unchanged with 90 % probability. The caging time τ is found to be a fast growing function of the plasma coupling parameter Γ according to the equation $\tau = A\exp(\Gamma^B)$. No definite value of Γ can be given for the observed liquid-solid phase transition, but the authors claim for $\Gamma = 172$ that the caging of the particles tends to be complete with $\tau \to \infty$. Compared to our approach of investigating the phase transition via intershell diffusion, the method of Donkó et al. examines the ion dynamics on a more fine scale, but comes to similar results.

In any consideration of the Coulomb crystallization phase transition, certain assumptions and definitions need to be made, in order to deduce a concrete value of Γ at which the transition occurs. In analytical approaches, for example, an analytical description of a solid or a liquid phase needs to be specified, or a suitable model needs to be found that describes the shell structured appearance of a one-component plasma in a trap. In numerical approaches, certain limits need to be set, such as in the case of Donkó et al. the 90 % probability and a limit for the caging time itself.

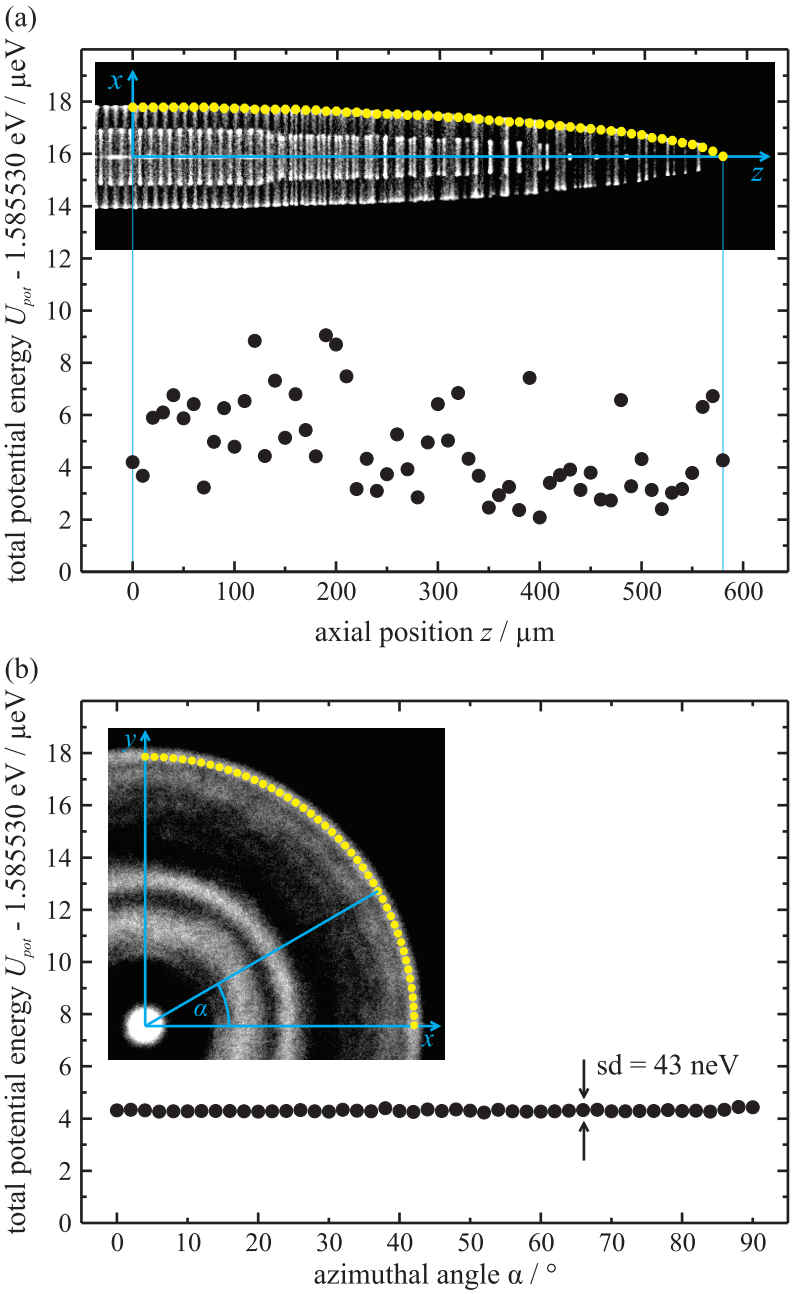

Figure 8.12: Potential barriers for intrashell ion motion. The total potential energy U_{pot} has been calculated for a prolate 500 ion ensemble for different intrashell paths of an additional fixed test ion within the outer shell (a) along axial direction z, and (b) along azimuthal direction with increasing azimuthal angle α as illustrated in the inset images with the yellow dots representing the fixed ion's positions. (a) In the axial case U_{pot} varies on the order of a few micro-electron volts due to an additional axial slice structure at low temperatures as in this case. (b) In the azimuthal case U_{pot} is constant as the ion ensemble just needs to rotate around the z-axis to react on a new position of the fixed test ion. The fluctuations of U_{pot} with a standard deviation of 43 neV are on the order of the numerical precision of our calculations.

In the simulations performed in this work, a threshold for the relative intershell diffusion rate k_{rel} has been set below which an ion ensemble is considered as crystallized to a solid state for a macroscopic duration. A value of $k_{rel} = 0.1\,\mathrm{ms}^{-1}$ has been chosen with respect to the significant changes of the ion motion in radial and axial direction. For this value, phase transition temperatures T_c can be derived from the fit functions using Eq. (8.4) as shown in the plots of Fig. 8.8. The values of T_c are listed in Tab. 8.3 for the investigated ion ensembles. A clear tendency is, that larger ion ensembles crystallize at lower temperatures, the prolate 1000 ion ensemble at 6.7 mK compared to the 300 ion ensemble at 9.5 mK.

Ion number	Symmetry	T_c / mK	a_{WS}/ µm	Γ
300	prolate	9.5	13.9	125
500	prolate	7.6	14.4	152
1000	prolate	6.7	14.8	168
500	spherical	6.2	15.2	177

Table 8.3: Simulation results. Given are the phase transition temperatures T_c of the investigated ion ensembles derived from the relative intershell diffusion rate fit functions for the condition $k_{rel} = 0.1\,\mathrm{ms}^{-1}$. With these values and the Wigner-Seitz radii a_{WS}, the plasma coupling parameters Γ can be calculated at which the phase transitions occur.

Further, Tab. 8.3 lists the Wigner-Seitz radii a_{WS} for the investigated ion ensembles as defined in Eq. (2.30). The Wigner-Seitz radius of an ion ensemble corresponds to the radius of the sphere with a volume equal to the volume per ion. In order to determine these radii, the volumes of the investigated ion ensembles have been calculated from the ion coordinates. With the radii a_{WS} and the transition temperatures T_c, the plasma coupling parameters Γ can be determined, at which the ion ensembles undergo the fluid-solid phase transition. Values of Γ range from 125 for the prolate 300 ion ensemble to 168 for the prolate 1000 ion ensemble, and to 177 for the spherical 500 ion ensemble. These values depend on the chosen threshold for the relative intershell diffusion rates, but their tendency and also their dimension agree well with those found in the literature. Most Γ values for the liquid-solid phase transition have been derived for large or infinite systems and values of 175 [88], 172 [87], 173 [89], or 178 [90] have been published. In systems with lower particle numbers, the phase transition occurs at significantly lower values [90, 89], for example at $\Gamma = 155$ in the case of one-component plasmas consisting of 250 particles or less [52].

Comparing the 500 ion ensembles of prolate and spherical symmetry, the phase transition value of Γ in the spherical case ($\Gamma_{sph} = 177$) is higher than in the prolate case ($\Gamma_{pro} = 152$). As these different symmetries have been achieved with significantly different trap parameters, the ion densities in the ensembles and therefore the Wigner-Seitz radii are different. Thus, it is not clear if ion ensembles with the same Wigner-Seitz radii but different symmetry, would show different phase transition temperatures T_c and coupling parameters Γ. Here, the prolate 500 ion ensemble shows a higher phase transition temperature and is thereby more stable than the spherical one of the same ion number.

9 Summary and outlook

This work presents various novel results in the field of trapped ion studies. All investigations involve laser-cooled $^{138}Ba^{+}$ ions confined in a linear quadrupole ion trap, which serve as coolant for complex molecular ions, as target for collisions with neutral atoms, or as model system in theoretical analyses. This chapter briefly summarizes the experimental apparatus, the applied techniques, and the achieved results, and gives an outlook of the current work and future plans. A German version of the summary can be found in Chapter 9.3.

9.1 Summary

The apparatus used in this work is a unique setup for sympathetic cooling of complex molecular ions to millikelvin temperatures. Its special feature is the use of a molecular ion source based on electrospray ionization that allows for the production of gas-phase molecular ions of almost arbitrary species with a maximum mass-to-charge ratio of 2,000 Da. Using an octopole ion guide, the produced molecular ions can be transferred to a linear quadrupole trap which is placed in an ultra-high vacuum chamber. In the presence of simultaneously trapped laser-cooled $^{138}Ba^{+}$ ions, the molecular ions can be stored, cooled down, kept cold and investigated for many minutes and in principle for up to hours.

Three different techniques are used to analyze experimentally observed trapped ion ensembles: The secular excitation method is non-destructive and based on a mass-selective resonant excitation of ion motion in the harmonic trap potential. It can be applied to identify the trapped ion species and to follow changes in the number of trapped ions. The ion extraction method is destructive and relies on a mass-selective extraction followed by detection of the trapped ions. It is also used for the identification of ion species and can give a qualitative evidence on the low temperature of the ions. The last method is the very versatile application of molecular dynamics simulations of the observed ion crystals, which enable to obtain quantitative values for ion numbers and temperatures. Furthermore simulations can be used for theoretical studies of the ions' interaction and dynamics.

Sympathetic cooling of proteins

In this work, the sympathetic cooling of complex molecular ions to translational temperatures below 1 K has been demonstrated for different types of molecules, such as dyes, pharmaceutical agents, amino acids, peptides, and even proteins, covering a mass range from 182 to 12,400 Da. Procedures have been developed and described to reliably prepare ensembles of translationally cold molecular ions for various applications, such as studies of molecular photodestruction rates or of collisions with neutral atoms.

Using the example of the protein cytochrome c, the most massive molecular species sympathetically cooled in an ion trap so far, the methods for detection of successful trapping and cooling, and temperature determination have been presented in detail. For such complex molecules with masses above a few hundred Daltons, multiple protonation during

the electrospray ionization process becomes more and more prevalent. This reduction of their mass-to-charge ratios is essential for these experiments because it makes this kind of molecules accessible for conventional mass spectrometers and quadrupoles in the first place, and it allows for a more efficient sympathetic cooling. In one case, multiply protonated molecules of the protein cytochrome c (mass = 12,390 Da, charge = +17 e) have been cooled to less than 0.75 K.

Measurement of photodestruction rates

One of the main goals of this work was to develop the experimental techniques required for high-resolution vibrational spectroscopy of cold, trapped complex molecular ions. In order to resolve spectral features, cooling is absolutely essential. Here, our setup provides advantageous conditions. However, a problem of spectroscopy on such small molecular samples in the gas-phase is that there is no or very low fluorescence emitted upon excitation so that there is no easily accessible signal for spectroscopy. A solution is destructive spectroscopy where destruction rates of the parent molecular ions are measured.

Two methods for measuring photodestruction rates of cold, trapped complex molecular ions have been developed within this project and are described in this work using the example of singly protonated glycyrrhetinic acid molecules (GAH^+) dissociated by a UV laser at 266 nm. In the secular excitation method, the decay of the parent molecular ions is detected during one photodestruction process via repeated secular excitation of the parent ions' motional resonance, which produces signals proportional to the number of parent ions. In the ion extraction method the composition of a set of initially similar Ba^+/GAH^+ ion crystals is analyzed via extractions of the ions from the trap after different exposure times to the UV laser. Measurements of the photodestruction rate were performed at different intensities of the UV laser and rates of less than $0.05\,s^{-1}$ have been determined, which is only possible due to the long ion storage times that can be achieved with this apparatus. For the UV laser wavelength of 266 nm a destruction cross section of $(1.1 \pm 0.1) \cdot 10^{-17}\,cm^2$ for GAH^+ has been determined.

Collisions of neutral atoms and trapped ions

As large molecules have complex and over-crowded spectra, cooling is absolutely essential in order to resolve spectral features. A combination of sympathetic translational cooling via laser-cooled atomic ions and internal cooling might be feasible via collisional cooling of the trapped molecular ions with laser-cooled neutral atoms. A suitable neutral atomic species needs to be conveniently laser-coolable with lasers of preferable high wavelengths in order not do dissociate the molecular ions, and its ionization energy needs to be high enough to prevent charge exchange with both the laser-cooled barium ions and the molecular ions.

To test their suitability for internal cooling, neutral atoms of the alkali metals Li, Na, K, Rb, and Cs from dispensers and the rare earth metal Yb from an oven have been collided with trapped laser-cooled and not cooled Ba^+ ions as well as complex molecular ions. For all species charge exchange reactions with Ba^+ ions have been observed, so that these species would not be suitable for collisional cooling. While K, Rb, and Cs showed charge exchange reactions with ground state and laser-excited Ba^+ ions, the charge exchange rates of Yb and Ba^+ were found to be state dependent. Concerning the collisions of the neutral atoms with trapped molecular ions, the collisions of Yb atoms with trapped GAH^+ and $AlaTyrH^+$ molecules were reactive and lead to the formation of adducts and fragments, in contrast to the alkali metals for which no such reactions have been observed.

Theoretical studies on Coulomb crystallization

When the translational energy of a trapped ion ensemble is sufficiently reduced by laser cooling, a first-order phase transition from a liquid to a solid state occurs with the ion ensemble changing from a disordered ion cloud to an ordered ion crystal. Molecular dynamics studies on the ion motion in ensembles with ion numbers typical for the experiments carried out in this work (≤ 1000) at temperatures around this phase transition have been performed. The simulations made use of our in-house simulation program *SOSC*, that has also been applied for the analysis of experimentally observed ion ensembles.

In a linear quadrupole trap, the ions arrange in shell structures which disables a free motion in radial direction towards other shells (intershell motion), but allows for an almost free diffusion within the shells (intrashell motion) . Intershell motion can only occur provided the kinetic energy of an ion is high enough to overcome a potential barrier, which has been analyzed in detail. The simulations have shown, that intershell diffusion rates in the considered ion crystals increase exponentially when the ion temperatures exceed certain values that well agree with the predictions of other established models. Ion ensembles of different ion numbers (300, 500, and 1000 $^{138}Ba^{+}$ ions) and symmetries (prolate and spherical) have been investigated showing a clear tendency for the phase transition temperatures: The higher the ion number, the lower is the transition temperature.

9.2 Outlook

One of the long-term goals of the entire project is to perform high-resolution spectroscopy on cold complex molecular ions. Within this work, the required basic principles for such investigations have been developed. Now, ensembles of almost arbitrary translationally cold molecular ions with masses in a range of 182 to 12,400 Da can reliably be prepared. Furthermore, photodestruction rates of the parent molecular ions can be measured to be applied for spectroscopic schemes based on photodestruction. Here, several approaches are possible, such as the direct destruction using low intensity, tunable cw UV lasers or IR depletion spectroscopy (Chapter 6.5). In the latter case, the cooled, trapped molecular ions are excited with a fixed frequency UV dissociation laser above the dissociation threshold and a certain destruction rate is measured. An additional tunable IR laser is used to excite vibrational transitions of the molecular ions. In case of a vibrational resonance, the population in the vibrational ground state is depleted and the destruction rate is reduced. This yields a destruction rate spectrum in which dips correspond to certain vibrational modes. Such studies are planned with singly protonated molecules of the dipeptide analine-tyrosine ($AlaTyrH^{+}$), that has already been successfully cooled in our apparatus. Here, a fixed frequency UV laser at a wavelength of 266 nm will be applied for destruction and a tunable diode laser at a wavelength around 1.4 µm for depletion exciting the first overtone of the phenol OH-stretching transition (see Chapter 6.6 for details). Similar investigations have already been performed in the group of Prof. Thomas Rizzo (EPFL Lausanne), where the $AlaTyrH^{+}$ ions have been cooled to less than 10 K using cryogenic buffer gas, i. e. internally and translationally [9]. It will be an exciting goal to see, if vibrational transitions in the $AlaTyrH^{+}$ spectrum can also be resolved in our experiments in which the internal energy of the molecules is not reduced and corresponds to room temperature.

Internal cooling is envisioned to be implemented in our setup, but requires a completely new ion trap design. As mentioned above, translationally cooled, trapped molecular ions could be internally cooled by collisions with cold neutral particles. This could be achieved by a dual ion-neutral trap in which the trap volume of an ion trap is overlapped with that of a magneto-optical trap. Alternatively, the translationally cooled molecular ions in an

ion trap could be exposed to a beam of laser-cooled neutral atoms from an external neutral atom trap. Within this work, prestudies have been performed to find a suitable neutral atom species that does neither react with the laser-cooled Ba^+ nor with the molecular ions. So far, no suitable species has been found that fulfills these conditions and is conveniently laser-coolable. An alternative could be neutral Hg atoms which have already been laser-cooled and confined in magneto-optical traps [91]. With their comparatively high ionization energy of 10.4 eV, charge exchange reactions with the trapped Ba^+ and molecular ions would be energetically impossible. Anyway, it is still an open question, if collisions with laser-cooled neutral atoms alone can sufficiently cool the molecular ions, as they contain comparatively large amounts of internal energy due to their huge number of degrees of freedom. Thus, it might be necessary to assist the internal cooling using cryogenical buffer gases for direct collisions and cooling of the trap and its environment.

Concerning the simulations on the liquid-solid phase transition, there are various aspects that could be investigated in more detail. It was found that the ions in shell structured ion ensembles move to neighboring shells with rates whose temperature dependence can be described by Arrhenius equations. These equations yield certain temperatures T_0 which were found to correspond to the height $k_B T_0$ of potential energy barriers that have to be overcome, when an ion moves from one shell to the other. These potential barriers have been investigated with simulations that include a fixed test ion moved along a radial path through the shell structure. It is a part of ongoing work within this project to achieve a better agreement of the values for $k_B T_0$ achieved from the Arrhenius fits to the intershell diffusion rates with those derived from the equilibrium positions of the ions in ensembles with fixed test ions. Therefore, more simulations with the test ion at different axial coordinates covering the whole length of the ion ensemble are performed, in order to determine an ensemble average for the height of the potential barriers. Further simulations could be performed on the aspect of the phase transition temperature depending on different ion numbers and symmetries. Here, one could chose trap parameters under which all investigated ion ensembles show the same Wigner-Seitz radius, i. e. the same ion density. This is a very critical value in ion ensembles, because they are strongly governed by the distance dependent Coulomb repulsion. Investigations at the same ion densities would reveal the true dependence of ion numbers and symmetries regardless of other aspects.

9.3 Zusammenfassung (Summary in German)

Für diese Arbeit wurde ein einzigartiger experimenteller Aufbau verwendet, mit dem komplexe Molekülionen translatorisch auf Temperaturen im Millikelvin-Bereich abgekühlt werden können. Die Besonderheit dieses Aufbaus besteht in der verwendeten, auf der Methode der Elektrospray-Ionisation (ESI) beruhenden Molekülionen-Quelle. Sie ermöglicht es, Moleküle unterschiedlichster Art zu ionisieren und in die Gasphase zu transferieren, wobei Masse-zu-Ladungs-Verhältnisse von bis zu 2000 Da realisiert werden können. Um die auf diese Weise erzeugten Molekülionen zu kühlen, werden sie mit einem Oktopol-Ionenleiter in eine lineare Quadrupol-Ionenfalle transferiert, die sich in einer Ultrahochvakuum-Kammer befindet. Hier werden sie gleichzeitig mit lasergekühlten $^{138}Ba^+$-Ionen gespeichert, in deren Gegenwart sich die Molekülionen durch die gegenseitige elastische Coulomb-Wechselwirkung translatorisch abkühlen − dies wird als sympathische Kühlung bezeichnet. Derart präparierte Ensembles kalter Molekülionen können in diesem Zustand für viele Minuten und im Prinzip sogar für Stunden aufrecht erhalten und untersucht werden.

Zur Untersuchung experimentell beobachteter Ionenensembles kamen drei verschiedene Methoden im Rahmen dieser Arbeit zum Einsatz: Die Methode der Säkular-Anregung

ist zerstörungsfrei und beruht auf einer massen-selektiven, resonanten Anregung der Ionenbewegung im harmonischen Fallenpotential. Sie kann angewendet werden, um gefangene Ionensorten zu identifizieren und Veränderungen der Anzahl der Ionen einer Sorte zu verfolgen. Die Methode der Ionen-Extraktion ist destruktiv, da sie auf einer massenselektiven Extraktion mit anschließender Detektion der gefangenen Ionen beruht. Sie wird ebenfalls zur Identifikation der gefangenen Ionensorten benutzt und kann auch für qualitativen Nachweis der Kühlung der Ionen herangezogen werden. Die dritte Methode beruht auf Molekulardynamik-Simulationen experimentell beobachteter Ionenkristalle. Durch den Vergleich von im Experiment aufgenommenen CCD-Aufnahmen mit solchen aus Simulationen lassen sich quantitative Werte für Ionenzahlen und -temperaturen ableiten. Zusätzlich können die Simulationen für theoretische Untersuchungen der Wechselwirkungen und der Dynamik gefangener Ionen verwendet werden.

Sympathische Kühlung von Proteinen

Im Rahmen dieser Arbeit wurde die sympathische Kühlung von komplexen Molekülionen auf Temperaturen unter 1 K an verschiedenen Molekülsorten demonstriert, wie beispielsweise an Farbstoffen, pharmazeutischen Wirkstoffen, Aminosäuren, Peptiden und sogar Proteinen. Dabei wurden Verfahren entwickelt und erprobt, Ensembles von translatorisch kalten Molekülionen mit Massen im Bereich von 183 bis 12400 Da verlässlich herzustellen. Derartige Ionenensembles dienten in anderen Teilen dieses Projekts als Modellsysteme zur Untersuchung der Photodestruktion und von Kollisionen mit Neutralatomen.

Am Beispiel des Proteins Cytochrom c, der massereichsten Molekülsorte, die jemals in einer Ionenfalle sympathisch gekühlt wurde, werden Methoden zum Nachweis der erfolgreichen Speicherung und Kühlung sowie der Temperaturbestimmung im Detail beschrieben. Bei solchen Molekülen und auch schon bei Molekülen mit Massen von mehreren Hundert Dalton kommt es durch das Vorhandensein vieler basischer Stellen im Molekül zu einer mehrfachen Protonierung der Moleküle während des Elektrospray-Prozesses. Diese mehrfache positive Ladung der Molekülionen führt zu einer Reduktion der Masse-zu-Ladungs-Verhältnisse. Erst dadurch lassen sich solche komplexe Moleküle wie Proteine mit üblichen Quadrupol-Fallen und -Massenspektrometern handhaben, da deren maximal zulässige Masse-zu-Ladungs-Verhältnisse häufig auf wenige Tausend Dalton begrenzt sind. Außerdem führt die mehrfache Ladung zu einer Annäherung der Masse-zu-Ladungs-Verhältnisse von Molekülionen und lasergekühlten atomaren Ionen und somit zu einer effizienteren sympathischen Kühlung in der Ionenfalle. In einem Fall konnte die Kühlung mehrfach geladener Cytochrom-Moleküle (Masse = 12390 Da, Ladung = +17 e) auf Temperaturen kleiner als 0,75 K demonstriert werden.

Messung von Photodestruktions-Raten

Eines der zukünftigen Ziele dieses Projekts war die Entwicklung von experimentellen Techniken, die zur hochauflösenden Vibrations-Spektroskopie an kalten, gefangenen komplexen Molekülionen benötigt werden. Eine Kühlung der Moleküle ist unbedingt notwendig, um deren komplizierte Vibrationsspektren auflösen zu können. Was dies betrifft, bietet unsere Apparatur notwendige, wenn auch aufgrund der fehlenden internen Kühlung noch nicht hinreichende Bedingungen. Ein Problem der Spektroskopie an solch kleinen Anzahlen von Molekülen in der Gasphase ist die geringe oder nicht vorhandene Fluoreszenz infolge der spektroskopischen Anregung, so dass ein gewohntes Messsignal zunächst einmal fehlt. Eine Lösung stellt die destruktive Spektroskopie dar, bei der Photodestruktions-Raten der Ausgangsmoleküle gemessen werden.

Zwei Methoden zur Messung von Photodestruktions-Raten wurden im Rahmen dieses Projekts entwickelt und werden in dieser Arbeit beschrieben. Hierbei wurden als Modellsystem einfach protonierte Moleküle der Glyzyrrhetinsäure (GAH^+) gefangen, sympathisch gekühlt und durch UV-Laserlicht bei einer Wellenlänge von 266 nm dissoziiert. Bei der Säkularanregungs-Methode wird der Zerfall der Ausgangsmoleküle während des Photodestruktionsprozesses durch wiederholte Säkular-Anregung gemessen, wobei Signale produziert werden, deren Amplitude proportional zur Anzahl der Ausgangsmoleküle ist. Bei der Ionenextraktions-Methode wird die Zusammensetzung eines Sets von anfänglich ähnlichen Ba^+/GAH^+-Ionenkristallen durch eine Extraktion der Ionen aus der Falle nach unterschiedlichen UV-Bestrahlungsdauern analysiert. Auf diesen beiden Wegen wurden Photodestruktions-Raten bei verschiedenen Intensitäten des UV-Laserlichts gemessen. Dabei konnten so geringe Raten von kleiner als $0,05\,s^{-1}$ gemessen werden, was nur durch die langen Speicherzeiten für Ionen in dieser Apparatur möglich ist. Für die UV-Wellenlänge von 266 nm wurde für GAH^+ ein Photodestruktions-Querschnitt von $(1.1 \pm 0.1) \cdot 10^{-17}\,cm^2$ bestimmt.

Kollisionen neutraler Atome und gefangener Ionen

Eine zusätzliche interne Kühlung der translatorisch gekühlten Molekülionen könnte durch Kollisionen mit lasergekühlten Neutralatomen realisiert werden. Eine dafür geeignete Neutralatomsorte sollte vorzugsweise mit großer Laserwellenlängen kühlbar sein, um die Molekülionen möglichst nicht zu dissoziieren. Außerdem sollte ihre Ionisierungsenergie ausreichend hoch sein, damit es weder zum Ladungsaustausch mit den lasergekühlten Barium-, noch den Molekülionen kommen kann.

Um ihre Tauglichkeit für eine solche interne Kühlung zu testen, wurden Neutralatome der Alkalimetalle Li, Na, K, Rb und Cs aus Dispensern und des Seltenerdmetalls Yb aus einem Verdampferofen zur Kollision mit gefangenen lasergekühlten und nicht gekühlten Bariumionen sowie komplexen Molekülionen gebracht. Bei allen Metallen wurden Ladungsaustauschreaktionen mit den Bariumionen beobachtet, so dass diese Metalle nicht für eine solche interne Kühlung geeignet wären. Während es bei K, Rb und Cs zum Ladungsaustausch mit Bariumionen im Grundzustand und im angeregten Zustand kam, waren die Ladungsaustauschraten zwischen Yb und Ba^+ abhängig vom Anregungszustand der Bariumionen. Was die Kollisionen der Neutralatome mit gefangenen Molekülionen betrifft, so waren die Kollisionen Ytterbiumatomen reaktiv und führten zur Bildung von Fragmenten und Addukten. Bei Kollisionen der Alkalimetallatome mit Molekülionen wurde keine Reaktionen beobachtet.

Theoretische Untersuchungen der Coulomb-Kristallisation

Wenn die translatorische Energie gefangener Ionen ausreichend abgesenkt wird, kommt es zu einem Phasenübergang erster Ordnung von einem flüssigen zu einem festen Zustand. Dabei verändert sich das Ionenensemble von einer ungeordneten Ionenwolke hin zu einem geordneten Ionenkristall. Die Ionenbewegung in Ensembles mit Ionenzahlen, die typisch für die Experimente im Rahmen dieser Arbeit sind (≤ 1000), wurde theoretisch bei Temperaturen um diesen Phasenübergang herum untersucht. Dazu wurde das hauseigene Simulationsprogramm *SOSC* verwendet, das auch für die Analyse experimentell beobachteter Ionenkristalle benutzt wird.

In einer linearen Quadrupol-Ionenfalle ordnen sich die Ionen in Schalenstrukturen an, wodurch eine freie Bewegung der Ionen in radialer Richtung hin zu anderen Schalen verhindert wird, eine beinahe freie Diffusion innerhalb der Schalen aber möglich ist. Die Ionen

können nur in benachbarte Schalen wechseln, wenn sie eine ausreichend hohe kinetische Energie aufweisen, um bestehende Potenzialbarrieren zu überwinden. Die durchgeführten Simulationen haben gezeigt, dass die Raten der Diffusion in benachbarte Schalen in den betrachteten Ionenkristallen exponentiell anwachsen, wenn die Ionentemperaturen gewisse Werte überschreiten, die gut mit den Vorhersagen anderer etablierter Modelle übereinstimmen. Es wurden Ionenensembles verschiedener Ionenzahl (300, 500 und 1000 $^{138}Ba^{+}$-Ionen) und unterschiedlicher Symmetrie (prolat und sphärisch) untersucht. Daraus ergab sich die klare Tendenz, dass die Phasenübergangstemperatur um so niedriger liegt, je höher die Ionenzahl ist.

Bibliography

[1] J. Doyle, B. Friedrich, R. V. Krems, and F. Masnou-Seeuws. Editorial: Quo vadis, cold molecules? *Eur. Phys. J. D*, 31(2):149–164, 2004.

[2] T. Glenewinkel-Meyer and D. Gerlich. Single and merged beamstudies of the reaction H_2^+ (v = 0, 1; j = 0, 4) + $H_2 \rightarrow H_3^+ + H$. *Israel J. Chem.*, 37:343–352, 1997.

[3] P. Staanum, S. D. Kraft, J. Lange, R. Wester, and M. Weidemüller. Experimental investigation of ultracold atom-molecule collisions. *Phys. Rev. Lett.*, 96(2):023201–4, 2006.

[4] S. Willitsch, M. T. Bell, A. D. Gingell, S. R. Procter, and T. P. Softley. Cold reactive collisions between laser-cooled ions and velocity-selected neutral molecules. *Phys. Rev. Lett.*, 100(4):043203–4, 2008.

[5] S. Inouye, M. R. Andrews, J. Stenger, H.-J. Miesner, D. M. Stamper-Kurn, and W. Ketterle. Observation of Feshbach resonances in a Bose-Einstein condensate. *Nature*, 392(6672):151–154, 1998.

[6] P. F. Weck and N. Balakrishnan. Importance of long-range interactions in chemical reactions at cold and ultracold temperatures. *Int. Rev. Phys. Chem.*, 25(3):283–311, 2006.

[7] J. C. J. Koelemeij, B. Roth, A. Wicht, I. Ernsting, and S. Schiller. Vibrational spectroscopy of HD^+ with 2-ppb accuracy. *Phys. Rev. Lett.*, 98(17):173002–4, 2007.

[8] E. R. Hudson, H. J. Lewandowski, B. C. Sawyer, and J. Ye. Cold molecule spectroscopy for constraining the evolution of the fine structure constant. *Phys. Rev. Lett.*, 96(14):143004–4, 2006.

[9] J. A. Stearns, M. Guidi, O. V. Boyarkin, and T. R. Rizzo. Conformation-specific infrared and ultraviolet spectroscopy of tyrosine-based protonated dipeptides. *J. Chem. Phys.*, 127(15):154322–7, 2007.

[10] A. Fioretti, D. Comparat, A. Crubellier, O. Dulieu, F. Masnou-Seeuws, and P. Pillet. Formation of cold Cs_2 molecules through photoassociation. *Phys. Rev. Lett.*, 80(20):4402–5, 1998.

[11] S. Jochim, M. Bartenstein, A. Altmeyer, G. Hendl, S. Riedl, C. Chin, J. Hecker Denschlag, and R. Grimm. Bose-Einstein condensation of molecules. *Science*, 302(5653):2101–2103, 2003.

[12] C. A. Regal, C. Ticknor, J. L. Bohn, and D. S. Jin. Creation of ultracold molecules from a fermi gas of atoms. *Nature*, 424(6944):47–50, 2003.

[13] J. D. Weinstein, R. deCarvalho, T. Guillet, B. Friedrich, and J. M. Doyle. Magnetic trapping of calcium monohydride molecules at millikelvin temperatures. *Nature*, 395(6698):148–150, 1998.

[14] F. M. H. Crompvoets, H. L. Bethlem, R. T. Jongma, and G. Meijer. A prototype storage ring for neutral molecules. *Nature*, 411(6834):174–176, 2001.

[15] M. Wewer and F. Stienkemeier. Molecular versus excitonic transitions in PTCDA dimers and oligomers studied by helium nanodroplet isolation spectroscopy. *Phys. Rev. B*, 67(12):125201, 2003.

[16] D. J. Larson, J. C. Bergquist, J. J. Bollinger, W. M. Itano, and D. J. Wineland. Sympathetic cooling of trapped ions: A laser-cooled two-species nonneutral ion plasma. *Phys. Rev. Lett.*, 57(1):70–73, 1986.

[17] K. Mølhave and M. Drewsen. Formation of translationally cold MgH^+ and MgD^+ molecules in an ion trap. *Phys. Rev. A*, 62(1):011401, 2000.

[18] P. Blythe, B. Roth, U. Fröhlich, H. Wenz, and S. Schiller. Production of ultracold trapped molecular hydrogen ions. *Phys. Rev. Lett.*, 95(18):183002, 2005.

[19] B. Roth, D. Offenberg, C. B. Zhang, and S. Schiller. Chemical reactions between cold trapped Ba^+ ions and neutral molecules in the gas phase. *Phys. Rev. A*, 78(4):042709, 2008.

[20] A. Ostendorf, C. B. Zhang, M. A. Wilson, D. Offenberg, B. Roth, and S. Schiller. Sympathetic cooling of complex molecular ions to millikelvin temperatures. *Phys. Rev. Lett.*, 97(24):243005, 2006. Erratum: 100(1):019904(E), 2008.

[21] D. Offenberg, C. B. Zhang, Ch. Wellers, B. Roth, and S. Schiller. Translational cooling and storage of protonated proteins in an ion trap at subkelvin temperatures. *Phys. Rev. A*, 78(6):061401, 2008.

[22] A. Ostendorf. *Sympathetische Kühlung von Molekülionen durch lasergekühlte Bariumionen in einer linearen Paulfalle*. PhD thesis, Heinrich-Heine-Universität Düsseldorf, 2004.

[23] C. B. Zhang. *Production and sympathetic cooling of complex molecular ions*. PhD thesis, Heinrich-Heine-Universität Düsseldorf, 2008.

[24] S. Earnshaw. On the nature of the molecular forces which regulate the constitution of the luminiferous ether. *Trans. Camb. Phil. Soc.*, 7:97–112, 1842.

[25] H. G. Dehmelt. Radiofrequency spectroscopy of stored ions I: Storage. *Adv. At. Mol. Phys.*, 3:53–72, 1967.

[26] W. Paul, H. P. Reinhard, and U. von Zahn. Das elektrische Massenfilter als Massenspektrometer und Isotopentrenner. *Z. Phys.*, 152(2):143–182, 1958.

[27] P. K. Gosh. *Ion traps*. Oxford University Press, 1996.

[28] L. Hornekær. *Single- and multi-species Coulomb ion crystals: Structures, dynamics and sympathetic cooling*. PhD thesis, University of Århus, 2000.

[29] M. Drewsen and A. Brøner. Harmonic linear Paul trap: Stability diagram and effective potentials. *Phys. Rev. A*, 62(4):045401, 2000.

[30] W. Schnitzler. *Development of an experiment for trapping, cooling and spectroscopy of molecular hydrogen ions*. PhD thesis, Universität Konstanz, 2001.

[31] B. Roth, P. Blythe, and S. Schiller. Motional resonance coupling in cold multispecies Coulomb crystals. *Phys. Rev. A*, 75(2):023402–8, 2007.

[32] C. B. Zhang, D. Offenberg, B. Roth, M. A. Wilson, and S. Schiller. Molecular-dynamics simulations of cold single-species and multispecies ion ensembles in a linear Paul trap. *Phys. Rev. A*, 76(1):012719, 2007.

[33] J. D. Prestage, A. Williams, L. Maleki, M. J. Djomehri, and E. Harabetian. Dynamics of charged particles in a Paul radio-frequency quadrupole trap. *Phys. Rev. Lett.*, 66(23):2964, 1991.

[34] V. L. Ryjkov, X. Z. Zhao, and H. A. Schuessler. Simulations of the rf heating rates in a linear quadrupole ion trap. *Phys. Rev. A*, 71(3):033414, 2005.

[35] M. Drewsen, C. Brodersen, L. Hornekær, J. S. Hangst, and J. P. Schifffer. Large ion crystals in a linear paul trap. *Phys. Rev. Lett.*, 81(14):2878, 1998.

[36] H. G. Dehmelt. Radiofrequency spectroscopy of stored ions II: Spectroscopy. *Adv. At. Mol. Phys.*, 5:109–154, 1969.

[37] W. M. Itano, J. C. Bergquist, J. J. Bollinger, and D. J. Wineland. Cooling methods in ion traps. *Phys. Scr.*, T59:106–120, 1995.

[38] T. W. Hänsch and A. L. Schawlow. Cooling of gases by laser radiation. *Opt. Comm.*, 13(1):68–69, 1975.

[39] D. J. Wineland and H. Dehmelt. Proposed $10^{14}\ \delta\nu < \nu$ laser fluorescence spectroscopy on Tl^+ mono-ion oscillator III (sideband cooling). *Bull. Am. Phys. Soc.*, 20:637, 1975.

[40] R. Drullinger, D. Wineland, and J. Bergquist. High-resolution optical spectra of laser cooled ions. *Appl. Phys.*, 22(4):365–368, 1980.

[41] P. Bowe, L. Hornekær, C. Brodersen, M. Drewsen, J. S. Hangst, and J. P. Schiffer. Sympathetic crystallization of trapped ions. *Phys. Rev. Lett.*, 82(10):2071, 1999.

[42] P. Banks. Collision frequencies and energy transfer - Ions. *Planet. Space Sci.*, 14:1105–1122, 1966.

[43] B. Roth. *Production, Manipulation and Spectroscopy of Cold Trapped Molecular Ions.* Habilitationsschrift, Heinrich-Heine-Universität Düsseldorf, 2007.

[44] S. Stenholm. The semiclassical theory of laser cooling. *Rev. Mod. Phys.*, 58(3):699, 1986.

[45] H. J. Metcalf and P. van der Straaten. *Laser Cooling and Trapping.* Springer-Verlag, 1999.

[46] O. H. Arroe. Hyperfine structure and isotope shift in barium. *Phys. Rev.*, 79(5):836, 1950.

[47] N. Yu, W. Nagourney, and H. Dehmelt. Radiative lifetime measurement of the Ba^+ metastable $D_{3/2}$ state. *Phys. Rev. Lett.*, 78(26):4898, 1997.

[48] A. Gallagher. Oscillator strengths of Ca II, Sr II, and Ba II. *Phys. Rev.*, 157(1):24, 1967.

[49] D. Reiß, A. Lindner, and R. Blatt. Cooling of trapped multilevel ions: A numerical analysis. *Phys. Rev. A*, 54(6):5133, 1996.

[50] J. P. Hansen. Statistical mechanics of dense ionized matter. I. Equilibrium properties of the classical one-component plasma. *Phys. Rev. A*, 8(6):3096, 1973.

[51] D. H. E. Dubin and T. M. O'Neil. Trapped nonneutral plasmas, liquids, and crystals (the thermal equilibrium states). *Rev. Mod. Phys.*, 71(1):87, 1999.

[52] E. L. Pollock and J. P. Hansen. Statistical mechanics of dense ionized matter. ii. Equilibrium properties and melting transition of the crystallized one-component plasma. *Phys. Rev. A*, 8(6):3110, 1973.

[53] D. J. Wineland. Ion traps for large storage capacity. *Proceedings of the Cooling, Condensation and Storage of Hydrogen Cluster Ions Workshop, Menlo Park, Ca, 1987, edited by J. T. Bahns*, page 181.

[54] H. Borawski. *Transfer von Molekülionen und Einschluss kalter Bariumionen in einer Paulfalle.* Diploma thesis, Heinrich-Heine-Universität Düsseldorf, 2004.

[55] M. Karas and F. Hillenkamp. Laser desorption ionization of proteins with molecular masses exceeding 10 000 Daltons. *Anal. Chem.*, 60:2299–2301, 1988.

[56] M. Yamashita and J. B. Fenn. Electrospray ion source. Another variation on the free-jet theme. *J. Phys. Chem.*, 88(20):4451–4459, 1984.

[57] J. B. Fenn, M. Mann, C. K. Meng, S. F. Wong, and C. M. Whitehouse. Electrospray ionization for mass spectrometry of large biomolecules. *Science*, 246(4926):64–71, 1989.

[58] J. B. Fenn. Electrospray wings for molecular elephants. *Nobel Lecture*, pages 154–184, 2002.

[59] D. Offenberg. *Sympathische Kühlung und massenselektiver Nachweis komplexer Molekülionen in einer Falle*. Diploma thesis, Heinrich-Heine-Universität Düsseldorf, 2006.

[60] E. D. Black. An introduction to Pound-Drever-Hall laser frequency stabilization. *Am. J. Phys.*, 69(1):79–87, 2001.

[61] Ch. Raab, J. Eschner, J. Bolle, H. Oberst, F. Schmidt-Kaler, and R. Blatt. Motional sidebands and direct measurement of the cooling rate in the resonance fluorescence of a single trapped ion. *Phys. Rev. Lett.*, 85(3):538, 2000.

[62] D. Offenberg, Ch. Wellers, C. B. Zhang, B. Roth, and S. Schiller. Measurement of small photodestruction rates of cold, charged biomolecules in an ion trap. *J. Phys. B*, 42(3):035101, 2009.

[63] L. L. Griffin and D. J. McAdoo. The effect of ion size on rate of dissociation: RRKM calculations on model large polypeptide ions. *J. Am. Soc. Mass Spectrom.*, 4(1):11–15, 1993.

[64] E. S. Worm, I. H. Andersen, J. U. Andersen, A. I. S. Holm, P. Hvelplund, U. Kadhane, S. B. Nielsen, J.-C. Poully, and K. Støchkel. Photodissociation of dinucleotide ions in a storage ring. *Phys. Rev. A*, 75(4):042709–7, 2007.

[65] B. Liu, P. Hvelplund, S. B. Nielsen, and S. Tomita. Photodissociation of singly charged oligonucleotide cations: Arrhenius parameters and identification of nonstatistical processes. *Phys. Rev. A*, 74(5):052704–6, 2006.

[66] S. B. Nielsen. Gas-phase studies of chromophore molecules in an electrostatic storage ring. *Phys. Scr.*, T110:332–335, 2004.

[67] J. T. Khoury, S. E. Rodriguez-Cruz, and J. H. Parks. Pulsed fluorescence measurements of trapped molecular ions with zero background detection. *J. Am. Soc. Mass Spec.*, 13(6):696–708, 2002.

[68] B. Roth, J. C. J. Koelemeij, H. Daerr, and S. Schiller. Rovibrational spectroscopy of trapped molecular hydrogen ions at millikelvin temperatures. *Phys. Rev. A*, 74(4):040501–4, 2006.

[69] E. S. Ensberg and K. B. Jefferts. The visible photodissociation spectrum of ionized methane. *Astrophys. J.*, 195:L89–91, 1975.

[70] A. Chakir, G. Solignac, A. Mellouki, and D. Daumont. Gas phase UV absorption cross-sections for a series of amides. *Chem. Phys. Lett.*, 404(1-3):74–78, 2005.

[71] P. Dagaut and M. J. Kurylo. A flash photolysis investigation of the gas phase uv absorption spectrum and self-reaction kinetics of the neopentylperoxy radical. *Int. J. Chem. Kin.*, 22(11):1177–1187, 1990.

[72] A. L. Smith. Comparison of the ultraviolet absorption cross section of C_{60} buckminsterfullerene in the gas phase and in hexane solution. *J. Phys. B*, 29(21):4975–4980, 1996.

[73] S. Ishiuchi, M. Fujii, T. W. Robinson, B. J. Miller, and H. G. Kjaergaard. Vibrational overtone spectroscopy of phenol and its deuterated isotopomers. *J. Phys. Chem. A*, 110(23):7345–7354, 2006.

[74] G. W. F. Drake, editor. *Handbook of Atomic, Molecular, and Optical Physics*. Springer Science+Business Media, Inc., 2006.

[75] D. J. Berkeland, J. D. Miller, J. C. Bergquist, W. M. Itano, and D. J. Wineland. Laser-cooled mercury ion frequency standard. *Phys. Rev. Lett.*, 80(10):2089, 1998.

[76] SAES Getters S.p.A., Via Gallarate 215, 20151 Milano, Italy. *Product brochure: Alkali Metal Dispensers*, 1992.

[77] M. Succi, R. Canino, and B. Ferrario. Atomic absorption evaporation flow rate measurements of alkali metal dispensers. *Vacuum*, 35(12):579–582, 1985.

[78] National Institute of Standards and Technology. *Physical reference data*. <http://physics.nist.gov/PhysRefData/Handbook/index.html>, 6 Oct. 2009.

[79] B. Cagnac, L. Tchang-Brillet, and J.-C. Pebay-Péroula. *Physique atomique - Atomes et rayonnement: interactions électromagnétiques*. Dunod, 2005.

[80] W. Kläui (Institut für Anorganische Chemie und Strukturchemie, Heinrich-Heine-Universität Düsseldorf), Private communication. 2009.

[81] J. Crassous (Equipe Organométalliques et Matériaux Moléculaires, Université de Rennes), Private communication. 2009.

[82] J. P. Schiffer. Melting of crystalline confined plasmas. *Phys. Rev. Lett.*, 88(20):205003, 2002.

[83] C. E. Mortimer. *Chemie*. Georg Thieme Verlag, 1996.

[84] L. Bergmann and C. Schaefer. *Lehrbuch der Experimentalphysik - Band 1: Mechanik, Relativität, Wärme*. de Gruyter, 1998.

[85] W. Demtröder. *Experimentalphysik, Band 1: Mechanik und Wärme*. Springer-Verlag, 1998.

[86] D. H. E. Dubin and T. M. O'Neil. Computer simulation of ion clouds in a Penning trap. *Phys. Rev. Lett.*, 60(6):511, 1988.

[87] Z. Donkó, G. J. Kalman, and K. I. Golden. Caging of particles in one-component plasmas. *Phys. Rev. Lett.*, 88(22):225001, 2002.

[88] M. Bonitz, P. Ludwig, H. Baumgartner, C. Henning, A. Filinov, D. Block, O. Arp, A. Piel, S. Kading, Y. Ivanov, A. Melzer, H. Fehske, and V. Filinov. Classical and quantum Coulomb crystals. *Phys. Plasmas*, 15(5):055704, 2008.

[89] R. T. Farouki and S. Hamaguchi. Thermal energy of the crystalline one-component plasma from dynamical simulations. *Phys. Rev. E*, 47(6):4330, 1993.

[90] W. L. Slattery, G. D. Doolen, and H. E. DeWitt. N dependence in the classical one-component plasma Monte Carlo calculations. *Phys. Rev. A*, 26(4):2255, 1982.

[91] H. Hachisu, K. Miyagishi, S. G. Porsev, A. Derevianko, V. D. Ovsiannikov, V. G. Pal'chikov, M. Takamoto, and H. Katori. Trapping of neutral mercury atoms and prospects for optical lattice clocks. *Phys. Rev. Lett.*, 100(5):053001, 2008.

Publications

1. A. Ostendorf, C. B. Zhang, M. A. Wilson, D. Offenberg, B. Roth, and S. Schiller, Sympathetic Cooling of Complex Molecular Ions to Millikelvin Temperatures. *Phys. Rev. Lett.* 97(24):243005, 2006. Erratum: 100(1):019904(E), 2008.
   Abstract: Gas-phase singly protonated organic molecules of mass 410 Da (Alexa Fluor 350) have been cooled from ambient temperature to the hundred millikelvin range by Coulomb interaction with laser-cooled barium ions. The molecules were generated by an electrospray ionization source, transferred to and stored in a radio-frequency trap together with the atomic ions. Observations are well described by molecular dynamics simulations, which are used to determine the spatial distribution and thermal energy of the molecules. In one example, an ensemble of 830 laser-cooled $^{138}Ba^+$ ions cooled 200 molecular ions to less than 115 mK. The demonstrated technique should allow a large variety of protonated molecules to be sympathetically cooled, including molecules of much higher mass, such as proteins.

2. C. B. Zhang, D. Offenberg, B. Roth, M. A. Wilson, and S. Schiller. Molecular-dynamics simulations of cold single-species and multispecies ion ensembles in a linear Paul trap. *Phys. Rev. A*, 76(1):012719, 2007.
   Abstract: The properties of cold ion plasmas with large numbers 200 of laser- and sympathetically cooled species are modeled in detail using molecular dynamics simulations. We describe how to extract temperatures and ion numbers from CCD images. The identification of the ion species by excitation of their oscillation modes is discussed. The sympathetic cooling efficiency, effects of the rf micromotion and of collision heating by a neutral background gas are analyzed, in part experimentally.

3. K. Højbjerre, D. Offenberg, C. Z. Bisgaard, H. Stapelfeldt, P. F. Staanum, A. Mortensen, and M. Drewsen, Consecutive photodissociation of a single complex molecular ion. *Phys. Rev. A*, 77(3):030702(R), 2008.
   Abstract: Using the positively charged aniline ion $C_6H_5NH_2^+$ as a test molecule, we demonstrate that it is possible to study consecutive photodissociation of complex molecular ions at the single molecule level in an ion trap. When a single $C_6H_5NH_2^+$ ion is exposed to laser light at 397 nm and 294 nm, direct or consecutive photodissociation leads to the production of a range of smaller polyatomic molecular ions such as $C_5H_6^+$ and $C_3H_3^+$. The applied method is very versatile and can, e.g., be used in combination with free electron lasers or synchrotron radiation sources.

4. B. Roth, D. Offenberg, C. B. Zhang, and S. Schiller. Chemical reactions between cold trapped Ba^+ ions and neutral molecules in the gas phase. *Phys. Rev. A*, 78(4):042709, 2008.
   Abstract: Using a laser-cooled ion trapping apparatus, we have investigated laser-induced chemical reactions between cold trapped Ba^+ ions and several neutral molecular gases at room temperature, O_2, CO_2, and N_2O, leading to the production of cold trapped 20 mK BaO^+ ions. The BaO^+ ions were converted back to Ba^+ ions via reaction with room-temperature CO. Reaction rates were determined by employing molecular dynamics simulations. The cold mixed-species ion ensembles produced were used for studying the efficiency of sympathetic cooling, by variation of the ratio

of laser-cooled to sympathetically cooled ion numbers. In one extreme case, 20 laser-cooled $^{138}Ba^{+}$ ions were capable of maintaining the translational temperature of 120 sympathetically cooled barium isotopes $^{135\text{-}137}Ba^{+}$ and 430 $^{138}Ba^{16}O^{+}$ molecules at approximately 25 mK.

5. D. Offenberg, C. B. Zhang, Ch.Wellers, B. Roth, and S. Schiller. Translational cooling and storage of protonated proteins in an ion trap at subkelvin temperatures. *Phys. Rev. A*, 78(6):061401, 2008.
   Abstract: Gas-phase multiply charged proteins have been sympathetically cooled to translational temperatures below 1 K by Coulomb interaction with laser-cooled barium ions in a linear ion trap. In one case, an ensemble of 53 cytochrome c molecules (mass $\simeq$ 12,390 amu, charge $+17e$) was cooled by $\simeq$ 160 laser-cooled barium ions to less than 0.75 K. Storage times of more than 20 min have been observed and could easily be extended to more than an hour. The technique is applicable to a wide variety of complex molecules.

6. D. Offenberg, Ch. Wellers, C. B. Zhang, B. Roth, and S. Schiller. Measurement of small photodestruction rates of cold, charged biomolecules in an ion trap. *J. Phys. B*, 42(3):035101, 2009.
   Abstract: In this work, we demonstrate quantitative measurements of photodestruction rates of translationally cold, charged biomolecules. The long-term stable storage of the molecular ions in an ion trap at ultra-high vacuum conditions allows measurement of small rates and verification that rates are linear in photodestruction laser intensity. Measurements were performed on singly protonated molecules of the organic compound glycyrrhetinic acid ($C_{30}H_{46}O_4$), dissociated by a continuous-wave UV laser (266 nm) using different intensities. The molecules were sympathetically cooled by simultaneously trapped laser-cooled barium ions to translational temperatures of below 150 mK. Destruction rates of less than 0.05 s^{-1} and a cross section of $(1.1 \pm 0.1) \cdot 10^{-17}$ cm^2 have been determined. An extension to tunable UV laser sources would permit high-resolution dissociation spectroscopic studies on a wide variety of cold complex molecules.

Acknowledgments

This project and this work would not have been successful without the support of so many people who I would like to thank at this point.

First of all, I would like to thank Prof. Stephan Schiller for giving me the chance to work on this exciting and challenging project. I very much appreciate his constructive support and his ambition to bring the project forward, and especially acknowledge his confidence to let me work independently allowing to develop own ideas and strategies.

Special thanks go to Dr. Bernhard Roth who was available at any time to help me with any problems in the lab, to answer and to discuss theoretical questions, to manage organizational problems, and to give the crucial advice in so many cases of doubt. His wide experience of an experimental physicist and his realistic assessment of feasibility helped so often to proceed in the right direction.

I would like to thank all the guys who worked with me on the barium project: My thanks go to Dr. Chaobo Zhang for the excellent and easy-going collaboration on "our" experiment, for introducing me into the ESI's secrets, and especially for his efforts on the so valuable simulations – even after he has left the group. I am very grateful to Dr. Mark Alexander Wilson who gave me important guidance during my first steps in research and inspired me to something really essential – keeping detailed records in lab books, which helped me so much when writing this work. Further, I would like to thank my predecessor Dr. Alexander Ostendorf who introduced me into the group and who was always available for giving me valuable advice whenever there were problems with "his" setup. My thanks go to Christian Wellers for his reliable support in lenghty temperature determinations and time-consuming simulations, and for numerous creative ideas. And Dr. Tobias Schneider I want to thank for his wide experience he brought into our group and especially his realistic and relaxed view of things.

A significant contribution to this work was given by our technicians Peter Dutkiewicz, Rita Gusek, Heinrich Hoffmann, and Jens Bremer. Special thanks go to Peter for his help in so many electronics emergencies, for urgent repairs and the development of customized, reliable electronics.

I would like to thank all present and former members of the Institute for Experimental Physics (Institut für Experimentalphysik) for a really cooperative working climate, for the pleasant working atmosphere, and many interesting discussions. There are so many more people who were directly or indirectly involved in this project, and I am sorry and would like to apologize that I cannot thank all of them personally here.

I gratefully acknowledge the financial support by the German National Merit Foundation (Studienstiftung des deutschen Volkes) through a doctoral fellowship.

Erklärung

Die hier vorgelegte Dissertation habe ich eigenständig und ohne unerlaubte Hilfe angefertigt. Die Dissertation wurde in der vorgelegten oder in ähnlicher Form noch bei keiner anderen Institution eingereicht. Ich habe bisher keine erfolglosen Promotionsversuche unternommen.

Düsseldorf, 30.10.2009

(David Offenberg)